Detection of Magnetically Trapped Neutrons: Liquid Helium as a Scintillator

A thesis presented

by

Daniel Nicholas McKinsey

to

The Department of Physics

in partial fulfillment of the requirements

for the degree of

Doctor of Philosophy

in the subject of

Physics

Harvard University

Cambridge, Massachusetts

February 2002

To my parents

Thesis advisor

John Morrissey Doyle

Author

Daniel Nicholas McKinsey

Detection of Magnetically Trapped Neutrons: Liquid Helium as a Scintillator

Abstract

Herein, we describe the magnetic trapping of ultracold neutrons and the design and testing of an experiment to measure the neutron beta-decay lifetime. In this approach, ultracold neutrons are loaded into a magnetic trap through the superthermal effect in liquid helium, and then the same helium bath is used as a scintillator to detect decay of the trapped neutrons. The design of the experiment is described in detail, with particular emphasis given to the technical development of charged particle detectors based on liquid helium and to the construction of a large, deep superconducting magnetic trap. Trapping of ultracold neutrons has been demonstrated with a statistical significance of 5.4 σ.

Contents

List of Figures

List of Tables

Acknowledgements

My greatest thanks goes to John Doyle, for teaching me most of what I know about experimental physics and being a physicist, and for supporting me in every way throughout graduate school.

I am also tremendously grateful to Paul Huffman, whose enormously capable and willing support extended into every facet of laboratory work. I would also like to thank Paul for teaching me so much about low temperature work, and for his careful and constructive reading of this manuscript.

Special thanks to Bob Golub, whose genius and vision made this work possible, and for telling us when we were doing it all wrong.

Appreciation is also extended to James Butterworth, for patience and intelligence, and teaching me about cryogenics in my early years of graduate school.

I would also like to thank my fellow graduate students on this experiment; we suffered together through endless late nights and leaky dewars. Carlo Mattoni (my "twin" in so many ways), radiated competence and willingness to help throughout graduate school, and was a constant source of industry and comradeship. Sergei Dzhosyuk deserves special mention for his natural competence, thorough industriousness, and unflagging good humor. Liang Yang was a neverending source of quiet competence; much of the success of this latest incarnation of the experiment is due to his work. Clint Brome, Bob Michniak, and Kyle Alvine also contributed significantly to the experiment.

Thanks to Jonathan Weinstein, for his exceptional sense of humor, and for our friendship throughout graduate school.

My appreciation also goes out to my fellow students in the Doyle Lab, for mak-

ing the basement of Lyman a pleasant but vigorous environment for work and play. Harvard has been a fertile environment for my intellectual growth, and the numerous lunchtime discussions aided my education and made my time at Harvard more pleasant.

Thanks to the folks at NIST for creating a supportive environment at the NCNR.

I am indebted also to Klaus Habicht for his early, careful work on the detection of helium scintillations.

I also wish to thank Eva Allan; her love sustained me through the late months of the experiment and the frenzied writing of this thesis.

This thesis is dedicated to my parents. I thank them for their total, unqualified support and enthusiasm.

Chapter 1

Introduction

1.1 Ultracold Neutrons

The term "ultracold neutrons" (also known as UCN) refers to neutrons whose energies are so low ($\sim$ 100 neV, T $\sim$ 1 mK) that they can be confined within an experimental apparatus using material walls. This is possible when the neutron cannot overcome the aggregate Fermi potential of the wall and the wavelength of the neutron ($\sim$ 80 nm at 1 mK) is large compared to the interatomic spacing. In this case the material walls present a step potential with a height

$$V_{mat} = 2\pi\hbar^2 Na/m_n,$$

where N is the number density of atoms, a is the coherent neutron scattering length, and m_n is the mass of the neutron[1]. For many wall materials the UCN can bounce off the walls many thousands of times before being absorbed; bottles made form these materals can store UCN for many minutes before they decay, are absorbed, or scatter inelastically. Some properties of a 1 mK neutron are listed in Table 1.1.

UCN are also of low enough energy to be affected strongly by gravity and exper-

Table 1.1: A summary of the properties of a 1 mK neutron.

Property	Expression	Value for a 1 mK UCN
Mass	m_n	1.675×10^{-27} kg
Energy	$\frac{3}{2}k_BT$	2.07×10^{-26} J (129 neV)
Speed	$(2E/m)^{1/2}$	4.97 m/s
Wavelength	h/m_nv	79.6 nm
Magnetic moment	-1.91 μ_N	9.65×10^{-27} J/T

imentally accessible magnetic fields. The strengths of these interactions are summarized in Table 1.2. The rich array of experimental tools available for the investigation of UCN makes possible many imaginative and interesting experiments.

UCN are particularly well suited for many experiments in fundamental physics where it is beneficial to keep neutrons in an apparatus for a long time. While thermal neutrons ($T \sim 300$ K, $v \sim 2700$ m/s) or cold neutrons ($T \sim 30$ K, $v \sim 860$ m/s) spend very little time ($\sim$ ms) in an experimental apparatus, ultracold neutrons, through material, magnetic, or gravitational confinement, can be stored for times limited primarily by the neutron lifetime ($\tau_n \sim 900$ s). Of particular interest are the search for the neutron electric dipole moment, in which long neutron coherence times are required, and the accurate measurement of the neutron lifetime, where neutron losses by processes other than beta decay must be suppressed.

1.2 The Neutron Lifetime

The neutron is the simplest unstable nucleus. The relationship between the neutron lifetime τ_n and the fundamental constants of nuclear decay, g_a and g_v, is particularly

Table 1.2: A summary of UCN interactions.

Interaction	Expression	Limit for a 1 mK UCN
Gravitational	$E_{grav} = mgh$	$h = 1.26$ m
Magnetic	$V_{mag} = \mu B$	$B = 2.15$ T
Strong	$V_{mat} = 2\pi\hbar^2 Na/m_n$	$Na = 5.01 \times 10^{23}\mathrm{cm}^{-3}\,\mathrm{fm}$

simple, with few theoretical uncertainties. This makes the neutron a unique laboratory for studies of the weak force. The neutron lifetime is an important parameter in evaluating the unitarity of the CKM quark mixing matrix.

The neutron lifetime is also interesting in the context of Big Bang Nucleosynthesis (BBN), determining the production of light elements in the early universe. Uncertainty in the neutron lifetime is the most significant theoretical uncertainty in estimations of ^{4}He production in the Big Bang[2].

Neutron Beta Decay

Neutrons and protons make up the nuclei of ordinary matter, and are each made of three quarks (one up and two down in the neutron, two up and one down in the proton). While protons are stable ($\tau_p > 6.7 \times 10^{32}$ years[3]), free neutrons are not. A free neutron decays in about 15 minutes to a proton, an electron, and an electron anti-neutrino:

$$\mathrm{n} \rightarrow \mathrm{p} + \mathrm{e}^- + \bar{\nu_\mathrm{e}} + 782.6\,\mathrm{keV}.$$

This decay is possible because the mass of the neutron ($\mathrm{m_n} = 939.5656\,\mathrm{MeV/c^2}$) is greater than the masses of all three products combined. The mass of the proton ($\mathrm{m_p} = 938.2720\,\mathrm{MeV/c^2}$) is slightly less than the neutron mass, the difference

arising from difference in electrostatic potential energy and from the mass difference between the up quark and the down quark. The mass of the electron is small ($m_e = 0.511\,MeV/c^2$), and the mass of the electron antineutrino is small indeed ($m_\nu \ll 1$ eV). The net energy difference in the decay is 782.6 keV, and is released as kinetic energy of the three decay products. According to the Standard Model, the decay is mediated by the charged W^- boson as shown in Figure 1.1.

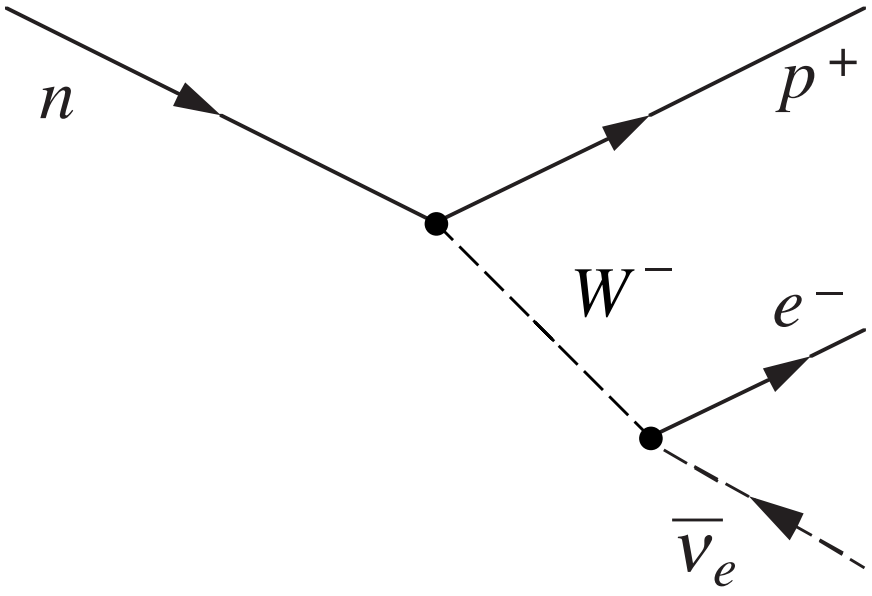

Figure 1.1: The neutron decays into a proton, an electron, and an electron antineutrino through the mediation of a W^- boson.

To understand the mechanism of neutron beta decay and learn of the implications of measuring the neutron lifetime, one must comprehend the theory of electroweak interactions. This theory merges the theories of electromagnetism and the weak interaction. Like quantum electrodynamics (the relativistic, renormalizable theory of electromagnetism), electroweak theory assumes a current that couples to itself at a single space-time point in the limit of low momentum transfer. But unlike quantum electrodynamics, which assumes a vector coupling γ_λ, electroweak theory assumes a

combination of vector and axial vector coupling, $\gamma_\lambda(1-\gamma_5)$. The Lagrangian density is given by

$$L = -\frac{G_F}{2\sqrt{2}}(J_\lambda J^{\lambda\dagger} + J^{\lambda\dagger} J_\lambda).$$

The weak current J_λ has both a leptonic and a hadronic part:

$$J_\lambda = j_\lambda^l + j_\lambda^h$$

where

$$j_\lambda^l = \bar{e}\gamma_\lambda(1-\gamma_5)\nu_e + \bar{\mu}\gamma_\lambda(1-\gamma_5)\nu_\mu + \bar{\tau}\gamma_\lambda(1-\gamma_5)\nu_\tau$$

couples leptons (electrons, muons, and tauons) to their respective neutrinos and

$$j_\lambda^h = \bar{d'}\gamma_\lambda(1-\gamma_5)u + \bar{s'}\gamma_\lambda(1-\gamma_5)c + \bar{b'}\gamma_\lambda(1-\gamma_5)t$$

couples quarks to each other. That is, the weak interaction can change quarks from one kind to another, and simultaneously turn leptons into neutrinos.

Because the quark mass eigenstates are not the same as the eigenstates of the weak force, the d, s, and b quarks are replaced by the weak interaction quark eigenstates of d', s', and b', which are obtained by transforming with the Cabibbo-Kobayashi-Maskawa quark mixing matrix:

$$\begin{pmatrix} d' \\ s' \\ b' \end{pmatrix} = \begin{pmatrix} V_{ud} & V_{us} & V_{ub} \\ V_{cd} & V_{cs} & V_{cb} \\ V_{td} & V_{ts} & V_{tb} \end{pmatrix} \begin{pmatrix} d \\ s \\ b \end{pmatrix}.$$

In the case of neutron decay, a neutron turns into a proton, electron, and antineutrino. The parts of the Lagrangian that pertain to other particles can be neglected to obtain:

$$L = \frac{G_F}{2\sqrt{2}} < p|j_\lambda^h|n > \bar{e}\gamma_\lambda(1-\gamma_5)\nu_e$$

where

$$< p|j^h_\lambda|n >= V_{ud}\bar{p}(\gamma_\lambda(1+\lambda\gamma_5))n.$$

Here it is assumed that the weak vector current is conserved (the CVC hypothesis). This is analogous to the conservation of charge in electromagnetism, and accounts for the fact that the weak vector current cannot depend on nucleon structure. By contrast, the weak axial vector current is not conserved and does depend on nucleon structure. This dependence is embodied in the free parameter λ, which must be determined by experiment.

The axial vector current can cause the proton to flip its spin relative to the neutron, but the vector current cannot. If the proton does flip spin, then the difference in angular momentum is made up in the angular momentum state of the neutrino-electron pair. The relationships between the spins and momenta of the particles in neutron beta decay are shown in Figure 1.2.

In neutron beta decay, correlation coefficients can be defined that characterize the relationships between the spin of the neutron and spins and momenta of its decay products. For example, the correlation coefficient A characterizes the probability that the electron is emitted in the direction of the neutron spin. If $N+$ is the chance that the electron will be emitted parallel to the neutron spin and $N-$ is the chance that it will be emitted antiparallel, then

$$A = \frac{N^+ - N^-}{N^+ + N^-} = \frac{|\Psi(\sigma_n \uparrow\uparrow p_e)|^2 - |\Psi(\sigma_n \uparrow\downarrow p_e)|^2}{|\Psi(\sigma_n \uparrow\uparrow p_e)|^2 + |\Psi(\sigma_n \uparrow\downarrow p_e)|^2}.$$

To calculate $|\Psi(\sigma_n \uparrow\uparrow p_e)|^2$ and $|\Psi(\sigma_n \uparrow\downarrow p_e)|^2$, it is convenient to approximate the electron mass and anti-neutrino masses to be zero. Then the electron momentum is always opposite to its spin (helicity -1/2) and the anti-neutrino momentum is always in the same direction at its spin (helicity 1/2). This is reflected in Figure 1.2; for

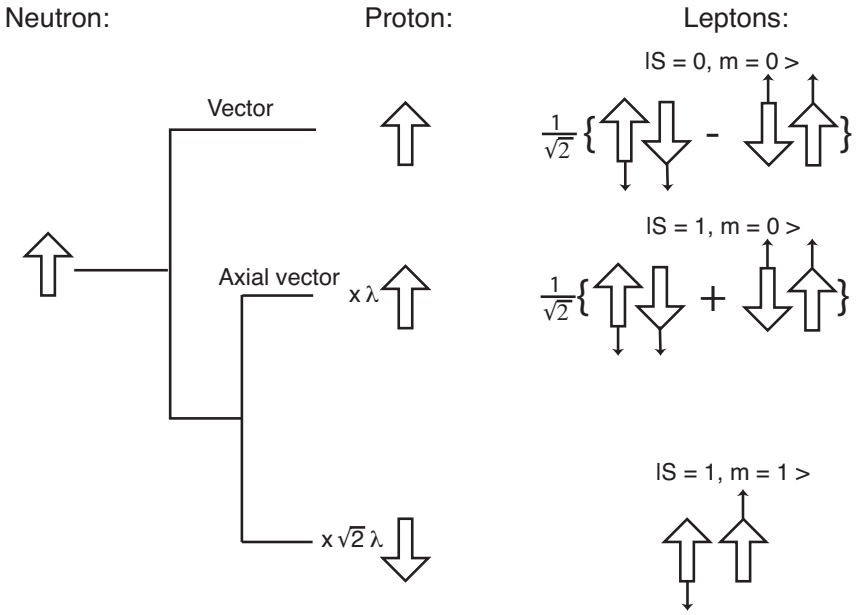

Figure 1.2: Simple scheme for calculating angular correlation coefficients a, A, and B. Wide arrows indicate spin direction, thin arrows indicate direction of momenta. Numerical factors are two- and three- spin one half coupling coefficients. This figure is taken from reference [4].

the electron, the wide arrow indicating spin is always in the opposite direction to the thin arrow indicating momentum, and for the anti-neutrino the opposite is the case.

Adding together the amplitudes for the electron to be emitted parallel to the neutron spin, then multiplying by the complex conjugate, we find:

$$|\Psi(\sigma_n \uparrow\uparrow p_e)|^2 = |\frac{1}{\sqrt{2}}(1-\lambda)|^2 = \frac{1}{2}(1 - 2\mathrm{Re}(\lambda) + |\lambda|^2).$$

Similarly, we can calculate the chance that the electron will be emitted anti-parallel to the neutron spin. In the this case the proton may flip spin; this is treated as a separate outcome and squared separately:

$$|\Psi(\sigma_n \uparrow\downarrow p_e)|^2 = |\frac{1}{\sqrt{2}}(-1-\lambda)|^2 + |2\lambda|^2 = \frac{1}{2}(1 + 2\mathrm{Re}(\lambda) + |\lambda|^2) + 2|\lambda|^2$$

Table 1.3: A summary of previous measurements of the neutron beta-decay asymmetry. These are the four measurements used by the PDG to evaluate CKM unitarity.[5]

Measured λ	Authors	Reference
-1.2735 ± 0.0021	Reich *et al.*	[6]
-1.266 ± 0.004	Liaud *et al.*	[7]
-1.2594 ± 0.0038	Yerozolimsky *et al.*	[8]
-1.262 ± 0.005	Bopp *et al.*	[9]

One then has

$$A_{exp} = \frac{N^+ - N^-}{N^+ + N^-} = \frac{|\Psi(\sigma_n \uparrow\uparrow p_e)|^2 - |\Psi(\sigma_n \uparrow\downarrow p_e)|^2}{|\Psi(\sigma_n \uparrow\uparrow p_e)|^2 + |\Psi(\sigma_n \uparrow\downarrow p_e)|^2} = -2\frac{|\lambda|^2 + \mathrm{Re}(\lambda)}{1 + 3|\lambda|^2}.$$

Other correlation coefficients relate the electron and neutrino momenta (a), the neutron spin and neutrino momentum (B), and the triple product of the neutron spin, electron momentum, and neutrino momentum (D). Like A, these coefficients can be expressed in terms of λ:

$$a = \frac{1 - |\lambda|^2}{1 + 3|\lambda|^2} \tag{1.1}$$

$$A = -2\frac{|\lambda|^2 + \mathrm{Re}(\lambda)}{1 + 3|\lambda|^2} \tag{1.2}$$

$$B = 2\frac{|\lambda|^2 + \mathrm{Re}(\lambda)}{1 + 3|\lambda|^2} \tag{1.3}$$

$$D = 2\frac{\mathrm{Im}(\lambda)}{1 + 3|\lambda|^2} \tag{1.4}$$

Obviously, any experimental measurements of these correlation coefficients should all yield consistent values of λ; discepancies could indicate physics beyond the Standard Model. At this time, experiments measuring A give the most accurate estimates of λ; these measurements are summarized in Table 1.3.

The matrix element for neutron decay can be written in terms of the correlation coefficients described above. Expressed as a decay rate dW, one finds that

$$dW = F(E_e)\left\{1 + a\frac{\vec{p_e}\vec{p_\nu}}{E_e E_\nu} + b\frac{m}{E_e} + \langle\vec{\sigma_n}\rangle \cdot (A\frac{\vec{p_\nu}}{E_e} + B\frac{\vec{p_\nu}}{E_e} + D\frac{\vec{p_e}\times\vec{p_\nu}}{E_e E_\nu})\right\}.$$

By averaging dW over spins and integrating over the energies of the decay products, one finds that

$$\tau^{-1} = \frac{m_e^5 c^4}{2\pi^3\hbar^7} f^R (g_v^2 + 3g_a^3)$$

where τ is the neutron lifetime, $g_v = V_{ud}G_F$, and $g_a = V_{ud}\lambda G_F$. The phase-space factor

$$f^R = 1.71465 \pm 0.00015$$

can be calculated including radiative corrections[10]. The factor of $3g_a^2$ derives from the 3 possible spin states of the lepton products in the case of axial vector coupling.

CKM Unitarity

Measurements of the neutron lifetime and any beta decay asymmetry allow one to determine the fundamental constants of the weak interaction. By comparing the constants determined through neutron beta decay with those measured in other processes, one can test the consistency of the theoretical framework of the Standard Model. In addition, one can test the unitarity of the CKM quark mixing matrix, that is, whether $V^\dagger V = I$. Unitarity implies that

$$|V_{ud}|^2 + |V_{us}|^2 + |V_{ub}|^2 = 1,$$

and this can be tested experimentally. By measuring the rates of the decays $B \to \pi\ell\nu_\ell$ and $B \to \rho\ell\nu_\ell$, $|V_{ub}|$ was measured to be $3.3 \pm 0.4 \pm 0.7 \times 10^{-3}$[11]. In a similar fashion, from the rate of the beta decay of the kaon, $K^+ \to \pi^0 e^+ \nu_e$, $|V_{us}|$

was determined to be 0.2196 ± 0.0023[12]. The limiting uncertainty in determining the unitarity of the CKM matrix is the measurement of V_{ud}, determined through $0^+ \rightarrow 0^+$ nuclear decay, neutron decay, or π^- decay. As seen in Figure 1.3, the value of V_{ud} measured through $0^+ \rightarrow 0^+$ nuclear decay is slightly less than unitarity would imply. The uncertainty from $0^+ \rightarrow 0^+$ nuclear decay is primarily theoretical, while testing unitarity through neutron decay is primarily experimental. Extracting V_{ud} through neutron decay requires two measurements: the neutron lifetime τ_n and a measurement of λ, usually done by determining A. Recent measurements of A vary substantially; depending on which measurement of A one chooses to believe, a value of $V^\dagger V$ either greater or less than unity may be obtained when these measurements are combined with the accepted value of the neutron lifetime. Measurement of the neutron beta-decay asymmetry continues to be a significant avenue of fundamental research, and improvements in the accuracy of the neutron lifetime will also aid in evaluating the unitarity of the CKM matrix.

Big Bang Nucleosynthesis

According to the Big Bang model, the universe originally existed entirely within a small region of space at an extremely high temperature. As neutrons and protons formed, their relative abundance was governed by

$$\frac{\mathrm{n}}{\mathrm{p}} = e^{\left(\frac{m_n - m_p}{kT}\right)}.$$

This state of thermal equilibrium was maintained through the reactions

$$\mathrm{n} + \mathrm{e}^+ \leftrightarrow \mathrm{p} + \bar{\nu_\mathrm{e}}$$

and

$$\mathrm{n} + \nu_\mathrm{e} \leftrightarrow \mathrm{p} + \mathrm{e}^-.$$

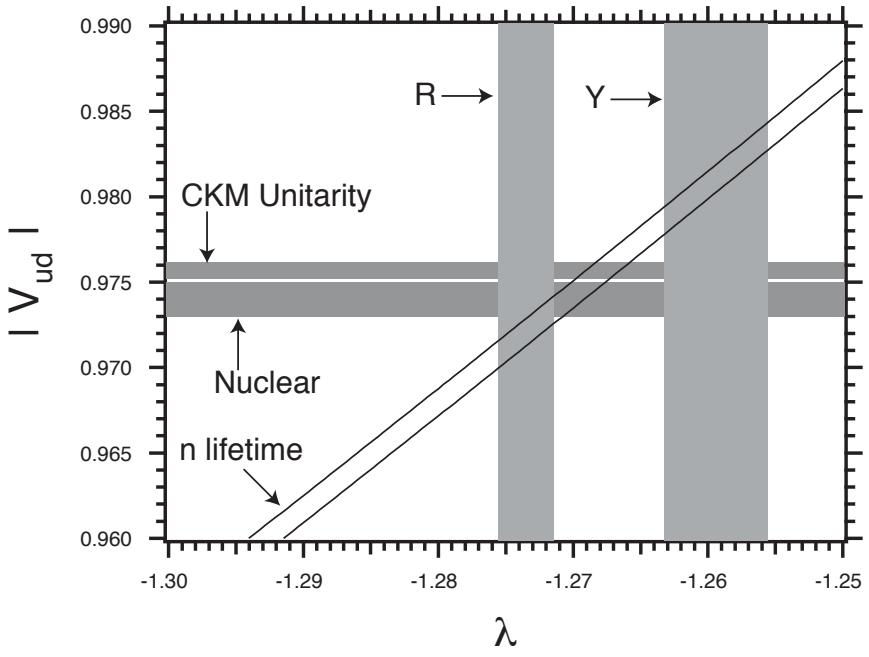

Figure 1.3: Plot of the 1 σ constraints on $|V_{ud}|$ and $\lambda = g_a/g_v$. Shown are the constraints on $|V_{ud}|$ from CKM Unitarity and $0^+ \rightarrow 0^+$ nuclear beta decay. Also shown are the constraints on λ from the two most precise measurements of the β-decay asymmetry in neutron decay, A, denoted in the figure as Y and R[8, 6]. The statistically combined measurements of the neutron lifetime, τ_n, further restrict the values of $|V_{ud}|$ and λ.

As the universe spread and cooled, the number of protons began to slightly exceed the number of neutrons, until at about 1 second after the Big Bang ($T \sim 1$ MeV). Then the neutron population decoupled from the protons. The precise time at which the decoupling occured depends on the cross-sections of the processes above, which can be calculated from the neutron lifetime. After the neutron population "froze out", the number of neutrons decreased due to neutron decay, while simultaneously many neutrons became bound up in ^{4}He nuclei via the processes

$$\mathrm{p} + \mathrm{n} \rightarrow \mathrm{d} + \gamma \tag{1.5}$$

$$\mathrm{d} + \mathrm{p} \rightarrow {}^3\mathrm{He} \tag{1.6}$$

$$^3\mathrm{He} + \mathrm{n} \rightarrow {}^4\mathrm{He} \tag{1.7}$$

These reactions continued for about three minutes and then essentially stopped because of the rapidly dropping temperature, density, and neutron population. Because the neutron lifetime enters twice in the calculation of the ^{4}He abundance (once in determining the initial neutron population, then again as a process competing with ^{4}He production), the measurement of the neutron lifetime is of great importance in testing the Big Bang model of nucleosynthesis. About a quarter of the baryonic matter in the early universe is ^{4}He, and the dominant uncertainty in the calculation of the ^{4}He/^{1}H ratio is in the decay lifetime of the neutron[2].

The isotopic ratios predicted by BBN can be tested by observations of interstellar gas clouds, where the abundances of light elements remain unchanged since the first few minutes of the universe. Along with the cosmic microwave background, the abundances of light elements are key predictions of the Big Bang theory. Accurate knowledge of the neutron lifetime is critical in the interpretation of these data.

1.3 Previous experiments

The currently accepted value of the neutron lifetime is 885.7±0.8 s[5]. The uncertainty in τ_n has dropped considerably in recent years, largely due to the establishment of techniques involving UCN. Table 1.4 and Figure 1.4 summarize this recent progress.

Neutron lifetime experiments to date can be divided into two categories: those that count neutron decays within a carefully defined beam volume, and those that count the neutrons remaining within a confinement apparatus after a variable time. These two methods suffer from quite different systematic uncertainties and thus complement each other nicely. A third method, counting neutrons as they decay within a superfluid

Table 1.4: A summary of previous measurements of the neutron lifetime. Measurements with uncertainties greater than 10 s are not included.

Measured lifetime (s)	Authors	Method	Reference
$885.7 \pm 0.9 \pm 0.4$	Arzumonov 00	UCN double bottle	[13]
$889.2 \pm 3.0 \pm 3.8$	Byrne 96	Beam, Penning trap	[14]
882.6 ± 2.7	Mampe 93	Material confinement, fomblin oil	[15]
$888.4 \pm 3.1 \pm 1.1$	Nesvizhevsky 92	Material confinement	[16]
887.6 ± 3.0	Mampe 89	Material confinement, fomblin oil	[17]
891 ± 9	Spivak 88	Beam	[18]
877 ± 10	Paul 89	Magnetic storage ring	[19]

helium-filled magnetic trap, is the subject of this thesis, and has its own (albeit much reduced) set of systematic uncertainties.

Beam method

In the beam method, neutron decays are counted within a carefully defined neutron beam volume. The rate C_d of decay products emitted from a beam of known flux is

$$C_d = -\frac{dN}{dt} = \frac{N}{\tau}$$

where N is the average number of neutrons in the decay volume. Clearly several quantities must be known quite accurately: the beam flux, the volume of beam accessible to the detectors, and the efficiency of detection. The most accurate measurement to date using this method was performed by Byrne *et al.*, finding a lifetime of $889.2 \pm 3.0 \pm 3.8$ s. In this experiment, the protons emitted in neutron decay were captured in a Penning trap, then released periodically onto a detector. This

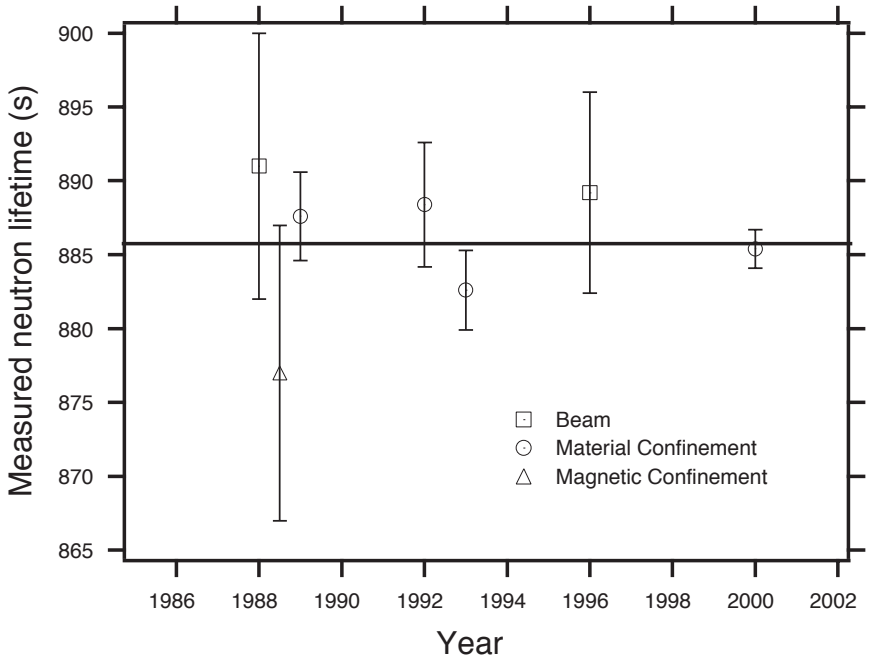

Figure 1.4: Previous measurements of the neutron lifetime. Three basic techniques are shown: beam, material storage, and magnetic storage. The horizontal line indicates the accepted (PDG) value, 885.7 ± 0.8 s. Error bars shown are the linear sum of the statistical and systematic errors.

store-and-dump method allowed a high signal-to-noise ratio; almost all of the counts detected were due to neutron decay. Experiments using the beam method are an important check on measurements of the neutron lifetime using UCN storage, though the formidable systematic uncertainties inherent to the beam method have prevented comparable accuracy; at this time the most accurate measurements of the neutron lifetime use UCN storage.

Storage Method

In the various storage methods, neutrons are contained within an apparatus for some time, then counted. In this case, the number of neutrons in the apparatus is described

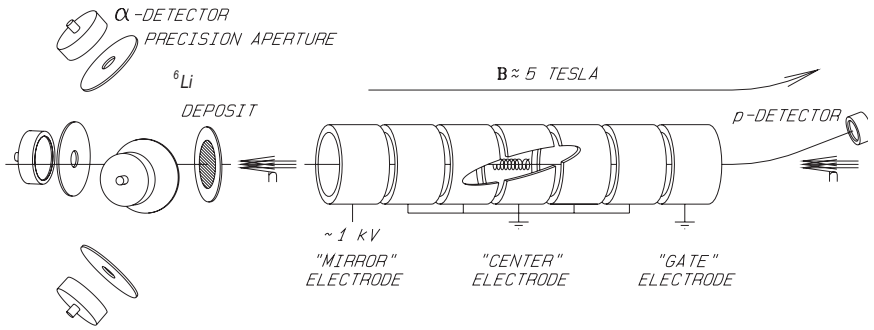

Figure 1.5: Schematic of the apparatus used in the beam lifetime measurement in reference [20]. A ^{10}B target and α-detectors measure the beam flux, while decay protons are stored in an electromagnetic Penning trap and then counted.

by

$$N(t) = N(0)e^{-t/\tau_{eff}(t)}$$

where

$$\frac{1}{\tau_{eff}} = \frac{1}{\tau_n} + \frac{1}{\tau_{loss}(t)}.$$

For all of these experiments there is some loss of neutrons from the apparatus; the key is to understand and minimize these losses. However, $N(0)$ need not be known well; it must only be constant from run to run. In addition, the detection efficiency need not be known well; it also must only be constant from run to run. It is possible that τ_{loss} depends on time through an energy dependence; higher energy neutrons may be more easily lost from the apparatus. In this case the time dependence of the neutron population may be non-exponential.

One version of neutron storage was performed using an sextupole magnetic storage ring. A conceptual drawing of this apparatus is shown in Figure 1.6. Neutrons were loaded into the ring by moving the end of a neutron guide for a very short time into the confinement region. Neutrons then orbited within the storage ring until a ^{3}He counter was placed in the beam. By varying the time at which the remaining neutrons

were counted, the lifetime of neutrons in the storage ring could be measured.

Because the stored neutrons were not energetically forbidden from leaving the storage ring, the difficulty of estimating losses was the major uncertainty in this experiment. Neutrons could be confined in semi-stable orbits, then be lost as translational momentum was transferred to transverse orbital oscillations; these are known as betatron oscillations. Though most neutrons in semi-stable orbits were lost at early times, betatron oscillations could in principle contribute to neutron losses, resulting in a systematic uncertainty in the measurement of the neutron lifetime. The measured neutron beta-decay lifetime in this experiment, 877 ± 10 s, is somewhat shorter than the current accepted lifetime, but constitutes a strict lower limit on the neutron lifetime.

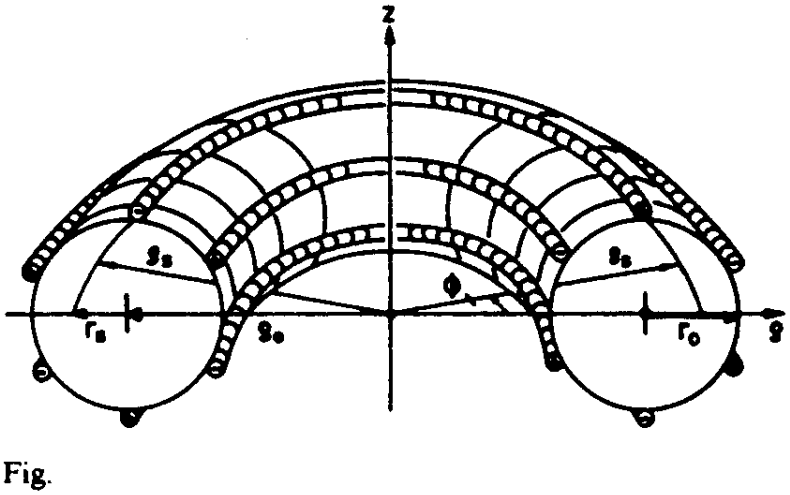

Figure 1.6: A sketch of the idea of the NESTOR experiment.

The most successful measurements of the neutron lifetime have used material confinement of UCN. In these experiments, a population of UCN are introduced into a closed container and then counted some time later. A conceptual drawing of

this sort experiment is shown in Figure 1.7. Table 1.5 lists the Fermi potentials for many different wall materials that can be used to store UCN. But more important than a high Fermi potential is the need for a low neutron loss rate per bounce. The two most successful approaches have used Fomblin oil and solid oxygen; both of these surfaces exhibit very low UCN loss rates. In these experiments, UCN are energetically forbidden from leaving the apparatus; however there is some loss due to UCN upscattering from the surfaces, and this loss can depend on energy, yielding a raw loss rate that is slightly non-exponential.

This loss is described by

$$< \tau_{wall}^{-1} >=< \mu(v)v > /\lambda$$

where $\mu(v)$ is the probability of loss per bounce, v is the velocity, $<>$ represents the average over the velocity spectrum, and λ the mean free path, as in kinetic theory

$$\lambda = \frac{4V}{S}$$

where S is the surface area of the storage vessel and V is the volume. The loss probability is given by

$$\mu(v) = 2f(\arcsin(y)/y^2 - \sqrt{(1-y^2)}/y)$$

where $y = v/v_{crit}$ (v_{crit} is the maximum velocity of the storable UCN as determined by the Fermi potential and f is the ratio of the real to the imaginary parts of the wall potential)[1].

Several approaches may be taken to understand spurious losses. One method is to vary the S/V ratio in the experiment; by extrapolating to infinite volume the lifetime may be extracted. Another method is to vary the energy spectrum of neutrons in the bottle. One clever way to do this is to confine the UCN vertically using only gravity,

Table 1.5: UCN potentials for a variety of materials. This table is adapted largely from references[1] and [21].

Material	N ($\text{cm}^{-3} \times 10^{22}$)	a (fm)	V_{mat} (neV)
Ni^{58}	9.0	14.4	346
BeO	7.25	13.6	257
Ni	9.0	10.6	252
Be	12.3	7.75	244
Diamond-like carbon	12.8	6.65	220
Stainless steel	8.5	8.6	188
Deuterated polystyrene	0.62	106.6	170
Cu	8.93	7.6	168
D_2O	3.04	19.1	150
PTFE (Teflon)	2.65	17.6	124
Fomblin oil	0.043	956	106
Quartz	2.2	16.1	91
O_2	2.68	11.6	80
Al	6.02	3.45	54

with a ceiling of variable height made with polyethylene. Any neutrons with enough energy to hit the polethylene would be lost. By studying the lifetime as a function of energy, the neutron beta-decay lifetime could be extracted. A final way to understand losses is to count upscattered neutrons; this was used profitably in [13]. Upscattered neutrons were detected by ^{3}He counters surrounding the experiment.

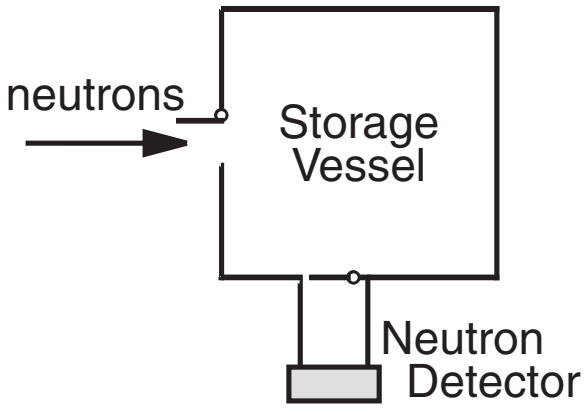

Figure 1.7: In neutron storage experiments, neutrons are contained within a material container. By varying the storage volume and energy of the stored neutrons, the neutron beta-decay lifetime may be extracted.

1.4 Magnetic Trapping of Neutrons to Measure the Neutron Lifetime

In neutron lifetime experiments using material storage, accuracy is limited by the ability to stably control the number of stored neutrons from run to run, control detection efficiency from run to run, and accurately extract τ_{loss}. In 1994, Doyle and Lamoreaux published an idea for measuring the neutron lifetime that eliminates all of these sources of systematic error[22]. In this method, UCN are magnetically trapped within superfluid helium, and their decays are detected continuously by counting pulses of scintillation light from the helium. Because the neutrons are energetically forbidden from escaping from the trap and never touch a material wall, spurious losses can be eliminated. And because the UCN are detected as they decay, variations from run to run in the number of confined neutrons or detection efficiency do not contribute to any systematic uncertainty.

Magnetic Trapping

To say that a particle is "trapped" means that its location is maintained within a given region of space, and it is prevented from touching any physical walls. The last two decades have seen enormous progress in trapping atoms, molecules, and fundamental particles. Trapping allows particles to be probed with long interaction times and can also permit a sample of particles to be thermally disconnected from the outside world. Recent advances in atomic cooling are particularly striking, and depend on the newly developed trapping technology.

One particularly popular sort of trap is the magnetic trap. This sort of trapping field interacts with the magnetic moment of the trapped particle and can thus trap

electrically neutral species. As the magnetic moment of a given particle can be positive or negative depending on its spin state, a given particle can either be attracted to higher or lower magnetic fields. It is not possible to create a magnetic field maximum in free space, but it is possible to create a magnetic field minimum[23]. Low energy particles that are attracted to a lower magnetic field will orbit around the field minimum.

Neutrons do not have a charge, so trapping must be achieved using their magnetic moment. They interact with a magnetic field, $\vec{B}$, by the dipole interaction:

$$H = -\vec{\mu} \cdot \vec{B}$$

Because their magnetic moment is so small, neutrons must have very low energy ($\sim$ 1 mK) to be trapped. In the semi-classical picture, they precess around the magnetic field with a frequency $\omega = 2\mu_n B/\hbar$ (or $\frac{\omega}{2\pi} \approx 29$ MHz at 1 Tesla). If the precession frequency is much higher than the change in the magnetic field seen by the neutron,

$$\frac{2\mu_n B}{\hbar} \gg \frac{d\vec{B}/dt}{|\vec{B}|},$$

then the magnetic moment of the neutron will follow the direction of the field adiabatically. Then the trap depth depends only on the magnitude of the magnetic field, not its direction.

One common magnetic field configuration is known as the Ioffe trap. The currents in an Ioffe trap are depicted in Figure 1.8. The four current bars create a field that rises in magnitude with radius, while the two current loops of the same sense provide axial confinement. This trap configuration has no point at which the magnitude of the magnetic field is zero. Therefore trapped particles precess with a high enough frequency that they do not flip their spin. The trap volume is roughly cylindrical. A

typical trap depth for Ioffe traps made in the past is about 1 T, though it may be possible to build traps as deep as 3.5 T.

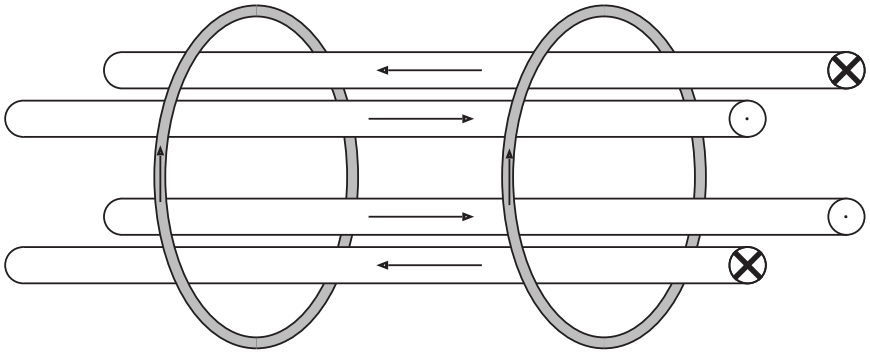

Figure 1.8: Currents in an Ioffe trap

The Superthermal Effect

Because the neutron has only a small magnetic moment ($\mu_{\mathrm{n}} = -1.91\mu_{\mathrm{N}} = -0.7\,\mathrm{mK/T}$), and typical magnetic trap depths are about 1 T, the neutron's energy must be lowered to less than 1 mK to be confined in a magnetic trap. This implies UCN energies, much less than the typical neutron energies available at cold neutron beam facilities. These use a moderating material (typically liquid hydrogen) to lower the energy of neutrons released in fission from nuclear reactors. Neutrons that thermalize in the cold source are reduced to energies of about 20-30 K, and exhibit a Maxwellian velocity distribution:

$$\rho(v)dv = \frac{2\Phi_0}{\alpha}\frac{v^2}{\alpha^2}e^{-v^2/\alpha^2}\frac{dv}{\alpha}$$

where v is the neutron velocity, Φ_0 is the total thermal flux, $\alpha = \sqrt{2k_BT_n/m}$, and T_n is the neutron temperature in the moderator[1]. Some of these neutrons have low enough energies to be considered UCN; by integrating the low energy tail of this

distribution one finds:

$$\rho_{UCN} = \frac{2}{3}\frac{\Phi_0}{\alpha}\left(\frac{E_{UCN}}{k_B T})^{3/2}\right)$$

where E_{UCN} is the maximum UCN energy. The maximum density of UCN that has been achieved using this method is about 90 cm^{-3} at the Institut Laue-Langevin in Grenoble, France.

Because these neutrons are in thermal equilibrium with the moderator, the rate of UCN upscattering to high energies is equal to the rate of high energy neutrons scattering to UCN energies. Consider the cross-section for neutrons scattering from a state of energy Δ to energy E_{UCN}. Detailed balance then implies:

$$\frac{E_{UCN}}{k_B T} e^{-E_{UCN}/k_B T}\sigma(E_{UCN} \rightarrow E_{UCN} + \Delta) = \frac{E_{UCN} + \Delta}{k_B T} e^{-(E_{UCN}+\Delta)/k_B T}\sigma(E_{UCN} + \Delta \rightarrow E_{UCN}) \tag{1.8}$$

which we can then write as an expression for the upscattering rate:

$$\sigma(E_{UCN} \rightarrow E_{UCN} + \Delta) = \frac{E_{UCN} + \Delta}{E_{UCN}} e^{-\Delta/k_B T}\sigma(E_{UCN} + \Delta \rightarrow E_{UCN}). \tag{1.9}$$

Note that the upscattering cross-section decreases exponentially with moderator temperature. If the temperature is low, e.g. $\Delta >> k_B T >> E_{UCN}$, then the upscattering rate can be made arbitrarily small.

This suppression of neutron upscattering allows the possibility of a second method of producing UCN. If neutrons with energy Δ have a resonance for scattering to UCN energies, then the density of UCN will build up to a value proportional to $(E_{UCN}/\Delta)e^{\Delta/k_B T}$. The density thus increases exponentially as the temperature decreases instead of as $1/T^2$ as found in a thermal moderator. The neutrons do not have to come into thermal equilibrium with the moderator for this "superthermal process" to proceed. Observe that in order for the superthermal process to produce a large number of UCN, there must be a significant number of neutrons with energy Δ. If the

neutrons were at the moderator temperature T, then the flux of neutrons at energy Δ would be down by a factor $e^{-\Delta/k_B T}$, thus canceling out the superthermal enhancement. It can thus be seen that the superthermal effect requires a large temperature difference between the neutron beam and the moderator to create a significant population of UCN. If the system is viewed thermodynamically as a neutron population (A) and a moderator (B), then the entropy and phase space of (A) decrease while the entropy and phase space of (B) and the system (A+B) both increase. The increase in entropy and phase space of (B) is a result of the excitation of the moderator, and allows the decrease of entropy and phase space of (A)[1].

In the neutron trapping experiment proposed by Doyle and Lamoreaux, UCN are created within the trap using liquid helium as a superthermal UCN source. To understand how superfluid helium can act as a superthermal UCN source, regard Figure 1.9. This figure depicts the superimposed dispersion spectra of superfluid helium and the neutron. The superfluid helium dispersion curve is the well-known spectrum of phonons and rotons in superfluid helium, while the dispersion curve of the neutron is simply a parabola: $E(q) = (\hbar q)^2/2m$. Neutrons of a critical wavelength 9 Å (where the dispersion curves cross) share the energy E^* and momentum q^* of a possible phonon state. These can therefore scatter to rest by creating a single phonon. After scattering to rest, the ultracold neutron is then highly unlikely to interact with the helium again, because it can only absorb a 9 Å neutron and still conserve energy and momentum. Because this wavelength corresponds to a relatively high energy phonon (12 K), and the population of phonons varies as $e^{-\Delta/kT}$, the neutron can travel through the helium unaffected if the helium temperature is much less than 12 K. The density of UCN in the superfluid helium is set by the lifetime of

the neutrons τ and the production rate $P(E_u)$:

$$P(E_u)dE_u = \Phi(E^*)n\sigma_{coh}\alpha S(q^*)\sqrt{E_u/E^*}dE_u$$

where $\alpha = |v_n/(v_n - v_g)|$ and $v_g = \partial\omega(q^*)/\partial q$, the phonon group velocity. P is equal to the neutron flux at 9 Å, multiplied by the scattering cross-section and integrated up to the maximum UCN energy E_{UCN}. The UCN density increases through superthermal production, but decreases through neutron loss, that is:

$$\frac{\mathrm{d}\rho_\mathrm{u}}{\mathrm{dt}} = P - \rho_u/\tau.$$

The solution of this differential equation is

$$\rho_u = P\tau(1 - e^{-t/\tau}),$$

which implies a maximum UCN density of $P\tau$.

The superthermal effect allows an enormous increase in phase space for the down-scattered neutrons. The incident neutrons occupy a volume in k space of $8\pi k^{*2}k_{UCN}$ and the UCN occupy a volume of $\frac{4}{3}\pi k_{UCN}^3$, a boost in phase space density of $6(k^*/k_{UCN})^2$. This is possible because the created phonons carry away the extra energy, and the entropy of the helium bath increases more than the entropy of the neutrons decreases[24].

Loading the Trap

The mean free path for a 9 Å neutron in superfluid helium is over 100 m. Therefore the UCN production rate in the trap will be essentially uniform. Low-field-seeking neutrons that scatter to an energy below the trap depth U_m will be magnetically trapped.

The trapping field can be approximated by a cylindrically symmetric potential, with infinite potential for $z < 0, z > l$ and rising linearly with radius to a maximum

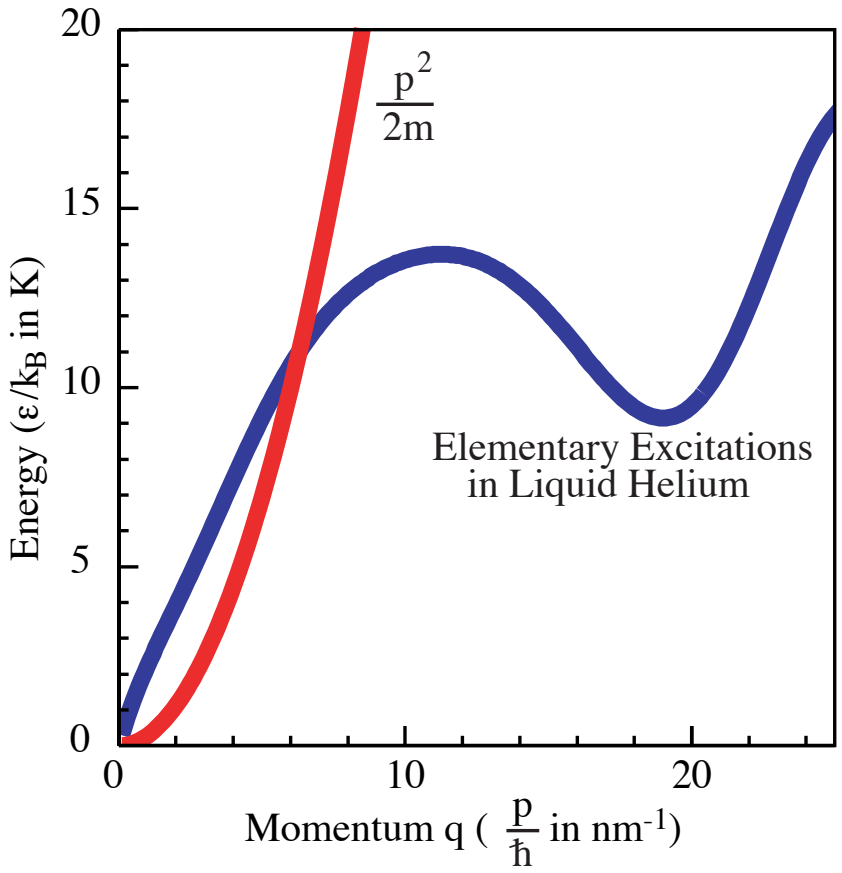

Figure 1.9: The superthermal process in superfluid helium: 9 Å neutrons create phonons in superfluid helium, scattering the neutrons to rest. Upscattering processes are suppressed by the Boltzmann factor $e^{-\Delta/kT}$

.

of U_m at r_0, where r_0 is the radius of the innermost material in the trapping region:

$$U(r,z) = \begin{cases} U_m \frac{r}{r_0} & \text{for } 0 < \mathrm{z} < \mathrm{L} \\ \infty & \text{for } \mathrm{z} < 0, \mathrm{z} > \mathrm{L}. \end{cases}$$

If the neutron scatters to a kinetic energy K such that $E_{total} = K + U(r,z) < U_m$, and it is in the low-field-seeking spin state, then it will be trapped.

Given the total flux Φ_{th} of cold neutrons at the end of a guide tube, the flux at

the critical energy E^* can be found using

$$\Phi(E^*) = \Phi_{th}\frac{E^*}{T^2}e^{-E^*/T},$$

where T is the neutron temperature exiting the cold source. By integrating the production rate P over trap volume and UCN energy , one can calculate the expected number of trapped neutrons. Depending on the neutron flux, trap volume, and trap depth, the number of trapped neutrons can vary between 10^3 and 10^5 per load. A description of Monte Carlo simulations of neutron trapping may be found in reference [25].

Detecting Trapped Neutrons

After the neutrons are accumulated in the trap for about half an hour, the beam is shut off. Neutrons with energies above the trap depth are quickly absorbed, while trapped neutrons spiral around the magnetic field minimum until they decay. When this happens, the electron and antineutrino carry most of the decay energy. The antineutrino leaves the experiment, while the electron deposits its energy within the liquid helium. The helium then scintillates in the extreme ultraviolet (EUV). The scintillation is highly efficient; about 35% of the energy of the recoiling electron is converted into prompt scintillation light. For a electron carrying 250 keV of kinetic energy, this corresponds to 5500 EUV photons. Unfortunately, EUV light cannot pass through most materials, though it easily travels through liquid helium. Therefore the walls of the trap are coated with a coating of fluor that converts the ultraviolet light to visible blue light. The blue light then travels out of the apparatus through light guides and is detected by light-sensitive photomultipliers at room temperature. The detection of neutron decays using liquid helium as a scintillator is discussed in great detail in Chapter 2.

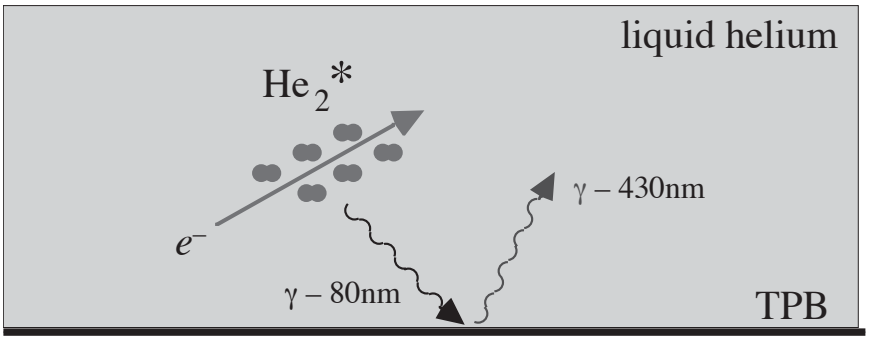

Figure 1.10: The principle behind the detection of neutron decay in superfluid helium.

Systematics

As mentioned above, this experiment should not suffer from many of the sources of systematic error that affect other neutron lifetime experiments. Because the decay curves observed can simply be added together and then fit, the experiment is not affected in a systematic way by fluctuations in neutron beam flux or detection efficiency. And because the neutrons do not interact with material walls, upscattering can be minimized in a simple way. There are several other possible sources of systematic error unique to this experiment, but all of these should be controllable at the 10^{-5} level.

The chance per second k that a given neutron will be absorbed by a ^{3}He nucleus is

$$k = \sigma_t \frac{v_t}{v_{He}} n v_{He} = \sigma_t v_t n$$

where σ_t is the thermal neutron absorption cross-section on ^{3}He, v_t is the velocity of a thermal neutron, v_{He} is the velocity of ^{3}He nuclei in the liquid helium bath, and n is the density of ^{3}He nuclei. The factor v_t/v_{He} takes into account the cross-section enhancement at low relative velocity. Note that the temperature of the helium bath is irrelevant, as the ^{3}He velocity cancels out.

Expressed as an absorption lifetime τ, we have

$$\tau = \frac{1}{k} = \frac{1}{\sigma_t v_t n} = \frac{3.15 \times 10^{-8}}{f}\,\mathrm{s}$$

where f is the ^{3}He/^{4}He ratio. By using helium with a ^{3}He/^{4}He of less than 3×10^{-15} one can suppress neutron absorption loss to 10^{-4} of the neutron beta-decay rate. This can be done using a heat flush method, in which ^{3}He nuclei are removed using a phonon wind in superfluid helium[26].

It is possible that some neutrons might scatter to energies slightly above the trap depth, yet not immediately impinge on the walls of the chamber. These neutrons might suffer from losses other than beta decay, thus rendering the neutron decay spectrum non-exponential and shortening the measured decay lifetime. This can happen if the energy is shared by several modes of motion. For example, a neutron with significant axial motion might slowly convert its kinetic energy to radial oscillations, hit the walls, and be lost. In order to eliminate these marginally trapped neutrons, one can temporarily lower the magnetic field, then raise it back. Calculations have shown that temprarily lowering the trapping field to 30% of its final value should eliminate all marginally trapped neutrons, while throwing away 50% of the trapped neutrons[23].

A second possible effect is a time-dependent detection efficiency due to an evolving distribution of neutrons in the various oscillatory modes within the trap. Because the electron emitted in beta decay can travel as far as 1 cm (a significant portion of the trap radius) within the liquid helium, and any energy deposited in the walls is not converted to EUV light, a slow movement of neutrons to larger radii would result in a detection efficiency that was decreasing with time, systematically decreasing the measured lifetime. This possible systematic would have to be studied by lowering the trap depth temporarily to eliminate trapped neutrons with trajectories near the

cell walls. It is believed that the entropic mixing of trajectory modes is rapid; in this case the detection efficiency should vary little with time over the neutron confinement period.

It is possible for trapped neutrons to flip spin, dropping in potential energy into a high-field seeking state. These neutrons would be immediately lost from the trap, shortening the measured lifetime. This loss mechanism can however be easily minimized by ensuring that the magnetic field experienced by the trapped neutrons is non-zero. Even a small magnetic field will ensure that the neutrons do not spin-flip; calculations show that a bias field of 0.1 T should ensure that the trap loss due to spin flips be less than 10^{-4} of the beta-decay rate[23].

Trapped UCN cannot be absorbed by the ^{4}He because this process is energetically forbidden. However, the UCN can be affected by phonons in the superfluid. As mentioned above, single-phonon absorption is highly suppressed because the temperature of the helium bath is significantly less than the critical phonon temperature of 12 K. Phonons with this energy are very rare at low helium temperatures, and highly unlikely to be absorbed by a trapped neutron. Instead, the dominant interaction of a phonon with a trapped neutron is two-phonon scattering. The rate of two-phonon scattering varies as T^7 where T is the temperature of the helium bath. At a temperature of 150 mK, the UCN upscattering lifetime is 10^8 s, yielding a negligible effect on the trapped neutron lifetime[23].

A final possible source of systematic error is neutron activation of materials surrounding the trap. If elements such as Al, Cu, V, or Si are activated, they will decay with lifetimes on the order of the neutron lifetime, releasing gamma rays, alphas, or betas into the superfluid helium. These decays will compete with the decays of trapped neutrons, creating a systematic uncertainty. This possibility requires careful

shielding of the neutron beam to avoid activation backgrounds.

Chapter 2

Scintillations in Liquid Helium: History and Motivation

2.1 Historical Background

The fact that liquid helium scintillates was established in 1959 by Thorndike and Shlaer[27] and simultaneously by Fleishman, Einbinder and Wu [28]. From their experiments, it was clear that helium emits light in the far ultraviolet when excited by ionizing radiation. The scintillation could be detected by coating the walls of the helium bath with an organic fluor, which would shift the wavelength of the scintillation light to the visible and render it detectable via a photomultiplier tube. Further experiments showed the scintillation pulse to be very fast, with a decay time of less than 10 ns[29]. The light did not pass through any standard window materials, even ones with very low cutoff wavelengths such as LiF[30]. Studying the scintillation pulses more carefully, Moss and Hereford found that the scintillation intensity from α sources had a peculiar temperature dependence below the λ point[31], and Kane *et al.* showed that beta sources did not display the same behavior. Based on this

observation, Hereford and Moss speculated that the scintillation could come from excited atoms or metastable states of the liquid[32]. Later, Jortner *et al.* showed that impurities suspended in the helium fluoresced in the visible, suggesting energy transfer from a helium metastable state[33]. But it was almost a decade before the scintillation mechanism was understood.

Meanwhile, liquid helium was under intense investigation for its fascinating superfluid properties. Its low energy excitations (phonons, rotons, and vortices) were a rich source of information about the superfluid state, and the subject of much experimentation. Then, in 1968, Surko and Reif discovered a new, fourth, kind of long-lived neutral excitation[34]. By immersing an alpha source (^{210}Po) in cold ($T < 0.6$ K) superfluid helium, excitations were produced that could travel through the liquid for distances greater than 1 cm without appreciable scattering or attenuation, causing He^+ ions and electrons to be emitted from the surface of the liquid helium, or positive ions and electrons to be emitted from a metal plate placed in the liquid. Because the excitations could ionize helium atoms ($E_i = 24.6$ eV), they clearly were much more energetic than phonons, rotons, and vortices; however the nature of these new neutral excitations was unknown. Later work showed that there was a substantial delay between the creation of the excitations and their arrival at the surface, and that beta excitation could also produce them[35, 36].

Then a breakthrough experiment gave reason to believe that the unknown source of EUV light and the unknown neutral excitation were both excited helium electronic states. In 1969, Dennis *et al.* measured the visible and near-infrared light spectrum from liquid helium bombarded by an intense 160 keV electron beam and found emission from both helium atoms and diatomic helium molecules[37]. In particular, it was shown that the molecular singlet and triplet ground states, $He_2(A^1\Sigma_u^+)$ and

$He_2^*(a^3\Sigma_u^+)$, were populated at a rapid pace. Both of these molecules are unstable for radiative decay to two ground state helium atoms and both emit a $\sim$ 16 eV (80 nm) photon when they decay. However their radiative lifetimes are much different. The $He_2(A^1\Sigma_u^+)$ molecule decays in less than 10 ns, whereas the radiative lifetime of the $He_2^*(a^3\Sigma_u^+)$ molecule is on the order of 10 seconds, since the decay to two helium atoms requires an electron spin flip[38]. The $He_2^*(a^3\Sigma_u^+)$ molecule was thus a plausible candidate for the neutral excitation discovered by Surko and Reif, while the $He_2(A^1\Sigma_u^+)$ was the source of scintillation pulses.

Additional interesting measurements were made possible by studying the transient behavior of individual atomic and molecular emission bands. If the electron beam were suddenly turned off at time $t = 0$, then the density of $He_2^*(a^3\Sigma_u^+)$ molecules was seen to decay rapidly, with a $1/t$ dependence[39, 40, 41]. This behavior could be explained by the hypothesis that $He_2^*(a^3\Sigma_u^+)$ molecules react with each other by Penning ionization:

$$He_2^* + He_2^* \rightarrow 3He + He^+ + e^-$$

or

$$He_2^* + He_2^* \rightarrow 2He + He_2^+ + e^-.$$

Penning ionization can happen because two excited helium molecules together have enough internal energy to ionize a helium atom. It requires no activation energy and occurs with nearly unity probability if the molecules collide. Penning ionization is a two-body reaction; this implies that the concentration M of metastable molecules is described by the equation $dM/dt = -\alpha(T)M^2$, which has the solution $1/M = 1/M_0 + \alpha(T)t)$, where $\alpha(T)$ is the bilinear reaction coefficient and M_0 is the initial concentration of $He_2^*(a^3\Sigma_u^+)$ molecules. The reaction coefficient $\alpha(T)$ was measured to be about $10^9\,cm^3\,s^{-1}$, and decreased with increasing temperature, indicating that the

reaction rate is affected by the roton density in the liquid. The higher the temperature, the higher the roton density, and the longer it takes two molecules to diffuse through the roton gas, find each other, and react.

It was also found that metastable He(2^3S) atoms are created in copious numbers as a result of the electron beam. But though this atom has an 8000 s radiative lifetime in vacuum[42], it does not last long in the helium liquid. The He*(2^3S) density was found to drop exponentially, with a 15 μs lifetime. A concurrent rise in density of vibrationally excited $He_2^*(a^3\Sigma_u^+)$ molecules was also seen, lending evidence to the hypothesis that in the dense liquid helium environment, ground state helium atoms can tunnel into the (2^3S) potential, forming vibrationally excited $He_2^*(a^3\Sigma_u^+)$ molecules. This reaction does not happen instantaneously because there is a 60 meV potential barrier between the He(2^3S and He(1^1S atoms[43]. This potential barrier is lowered at high densities, indicating that a third helium atom can lower the barrier significantly.

Further work centered on measuring the extreme ultraviolet scintillation spectrum using a grated EUV spectrometer[44, 45, 46]. It was found that a very intense continuum was produced in the wavelength range from 60 to 100 nm, corresponding to the reaction

$$He_2(A^1\Sigma_u^+) \rightarrow 2He(1^1S) + \hbar\nu.$$

The EUV spectrum measured in reference [44] is shown in Figure 2.1. The large wavelength spread is a consequence of the fact that the reaction product (two free helium atoms) is not a bound state. In the Oppenheimer approximation, the slowly moving helium nuclei do not change position during a fast electronic transition. Therefore the amount of energy released as light depends on the distance between the two He nuclei at the time of radiative decay. The remaining energy goes into kinetic energy

of the two final 1^1S helium atoms.

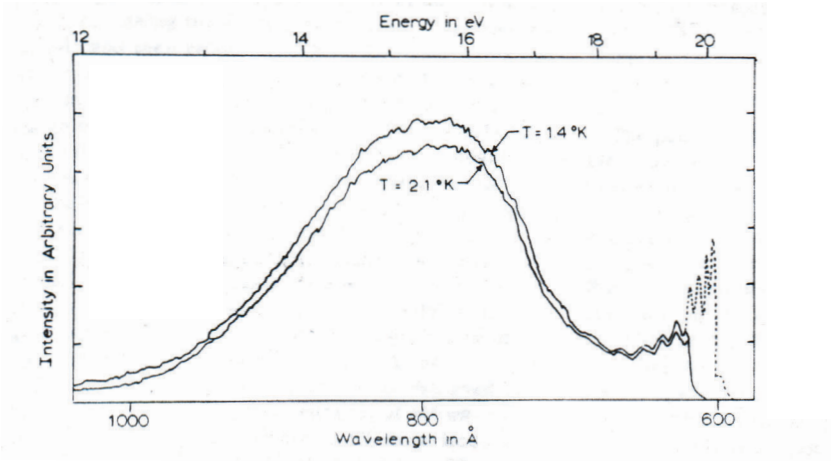

Figure 2.1: The scintillation spectrum of electron-bombarded liquid helium (from reference [44].

The bands at the short wavelength end of the spectrum are believed to be due to the radiative decay of high vibrational states of $He_2^*(A^1\Sigma_u^+)$. The high vibrational levels are probably populated in a similar way as the high vibrational levels of $He_2^*(a^3\Sigma_u^+)$: reactions of excited helium atoms with the surrounding helium. Just as $He^*(2^3S)$ atoms react with surrounding helium atoms to form vibrationally excited $He_2(a^3\Sigma_u^+)$, $He(2^1S)$ atoms react with the liquid to form vibrationally excited $He_2(A^1\Sigma_u^+)$. The time for this process to occur has not been measured, but should be comparable to the 15 μs lifetime of the $He^*(2^3S)$ atom.

It was also found that varying the location of the electron beam relative to the liquid helium surface had little effect on the measured EUV intensity. The scintillation light was unattenuated by as much as 10 cm of liquid helium. The transparency of

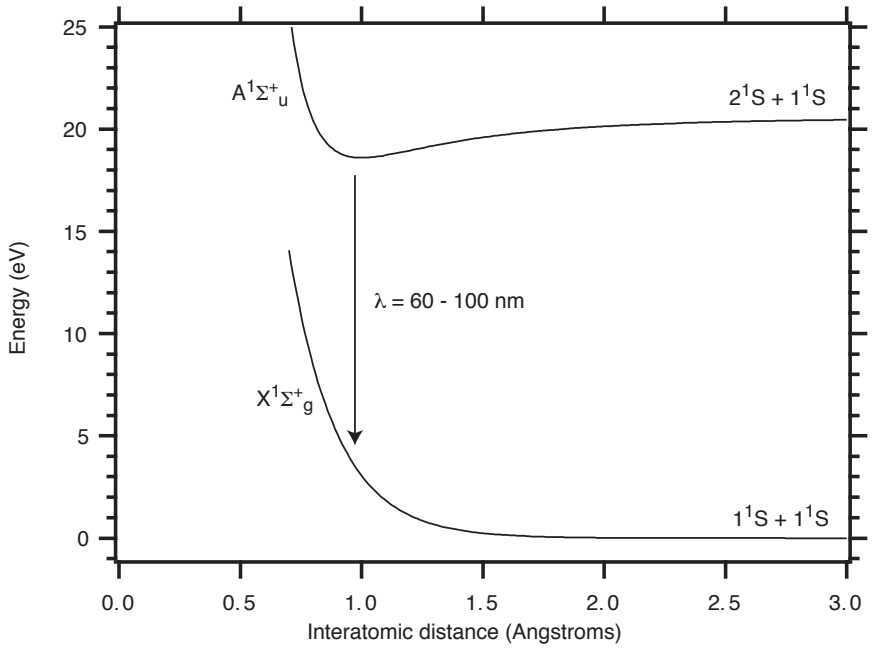

Figure 2.2: The potential curves of $He_2(A^1\Sigma_u^+)$ and the ground state $He_2(X^1\Sigma_g^+)$ (equivalent to two free He atoms).

liquid helium to its own scintillation light can be explained by the high energy needed to excite atomic helium; the difference in energy between the 1^1S ground state and the first atomic helium excited state is 20 eV, more energy than that of the 16 eV photons emitted in helium excimer decay. The fact that singlet production is enhanced in the liquid, plus the fact that helium does not absorb its own scintillation light, results in an extremely bright EUV pulse from $He_2(A^1\Sigma_u^+)$ decay. In fact, the ultraviolet emission accounts for over 99% of the total scintillation intensity[44]. The extraordinary intensity of the ultraviolet emission has been measured recently by Adams *et al.*; they find that 35% of the energy deposited by beta particles in superfluid helium is emitted as prompt EUV light[47, 48].

Because the $He_2^*(a^3\Sigma_u^+)$ molecules are destroyed by Penning ionization in these experiments, the spectrum was dominated by $He_2(A^1\Sigma_u^+)$, which can radiatively de-

cay before reacting with other metastables[40, 41]. But while triplet molecules were destroyed quickly in the spectroscopic measurements that required high molecular densities, they can survive for very long times ($\sim$ 10 s) in experiments where the excitation was more modest (such as the Surko and Reif experiment). If the excitation density were lower, then one might expect to see contributions from $He_2^*(a^3\Sigma_u^+)$ decay as well.

Such experiments using weak radioactive sources were carried out in parallel by the Hereford group at the University of Virginia. But instead of looking at atomic and molecular spectra, these experiments used a wavelength shifting fluor deposited on the cavity walls to convert the EUV scintillation light to the visible. This had the drawback of not being able to discriminate different atomic and molecular states, but allowed the study of individual decay events. Several interesting results followed from this work. First, it was found that the intensity of scintillation pulses created using an alpha source decreased significantly as the helium was cooled; as mentioned above, this was one of the first pieces of evidence for the creation of metastable excited states in the liquid helium. Second, it was shown that the scintillation light could be significantly quenched by the application of an electric field. By studying how the pulse height varied with electric field strength, and estimating the number of ion-electron pairs produced, they estimated that 60% of the scintillation pulse intensity derives from electron-ion recombination. Third, it was found that excited liquid helium emits a large number of photons well after the initial scintillation pulse. The rate of delayed photons depended on both temperature and the size of the helium bath, suggesting that the photons were emitted by metastables that diffused through the liquid helium and were quenched when they hit the wall.

Work in more recent decades has centered on the study of the metastable molecule

$He_2^*(a^3\Sigma_u^+)$. It was found that these molecules in solid helium decay radiatively with a lifetime of about 15 s[49]. This long lifetime could be observed spectroscopically in this case since Penning ionization in the solid was suppressed by slow molecular diffusion. Later attempts to suppress Penning ionization in the liquid by application of a strong magnetic field proved unsuccessful[50]. Another group managed to set a lower limit of 10 seconds on the $He_2^*(a^3\Sigma_u^+)$ lifetime in liquid helium by measuring the time of flight between a discharge and a surface ionization detector[51].

2.2 Fundamental Physics Experiments Using Liquid Helium as a Scintillator

In recent years, the application of liquid helium as a scintillator has received new attention. Possible experiments that would make use of the large scintillation yield of liquid helium are the search for the neutron electric dipole moment, the measurement of the neutron beta-decay lifetime, and the detection of low energy solar neutrinos.

In the search for the electric dipole moment (EDM) of the neutron, a method recently proposed by Golub and Lamoreaux promises significant gains in sensitivity. In this approach, ultracold neutrons are produced in superfluid helium doped with polarized ^{3}He[52]. The neutron absorption cross-section of ^{3}He is strongly dependent on the relative spin of the neutron and ^{3}He nucleus. By giving the neutrons and ^{3}He nuclei each a $\pi/2$ spin flip, the difference between the precession frequency of the neutron and that of the ^{3}He nucleus can be measured by monitoring the rate of $^3\mathrm{He}(\mathrm{n},\mathrm{p})^3\mathrm{H}$ events detected by counting pulses of EUV scintillation light. By alternating the direction of a strong electric field (either parallel or antiparallel to the magnetic field), and looking for a change in the scintillation rate, several orders of

magnitude more sensitivity for the neutron electric dipole moment may be obtained. The gains in sensitivity derive from the high density of UCN produced in the superthermal process and the high electric field that can be tolerated in liquid helium. This experiment requires tight control over stray magnetic fields, and must be surrounded by mutiple layers of magnetic shielding. This places constraints on the type of light collection system used to detect helium scintillation events. The detector will have to be carefully designed, and may make use of wavelength shifting fibers, as this will allow the scintillation signal to be passed out of the cryogenic region without seriously compromising the limits on magnetic field inhomogeneities. However, the signal yield from fiber-based detectors is not high, and in addition the scintillation signal will be significantly decreased by the application of the electric field, since most of the signal from the main pulse is a result of ion-electron recombination[53]. Detector designs based on wavelength shifting fibers will be discussed in Chapter 3.

The detectors described in the next chapter were designed specifically for the monitoring of decays of ultracold neutrons in a superfluid helium-filled magnetic trap. In this experiment, first proposed by Doyle and Lamoreaux in 1994, neutrons are loaded into the trap through inelastic scattering in superfluid helium, and then the same helium is used as a scintillator to detect their decay[22]. Because of the spectre of neutron activation, the design of these detectors was constrained significantly; the only elements allowed in the materials used to construct the detectors were carbon, hydrogen, oxygen, fluorine, and boron. Initially, an additional constraint was imposed: that the neutron beam be allowed to pass through the detector without significant absorption. This constraint was later removed, and allowed more efficient scintillation detection. The program of detector development was begun in 1995, and is the primary subject of the next chapter.

Superfluid helium has also been suggested as a medium for detecting the elastic scattering of low energy solar neutrinos. Because superfluid helium can be easily cleaned of radioactive impurities, it is a promising medium for this low-background experiment. Two distinct approaches to capturing the scintillation signal have been proposed, one using silicon calorimeters[54] (HERON), and one using wavelength shifters and photomultipliers (CLEAN). The two approaches do not only differ in the technology used to detect EUV scintillation, but also employ very different approaches to background rejection. The CLEAN approach was inspired largely by the neutron beta-decay detector development program described in the next chapter, but a full explanation of the CLEAN approach is beyond the scope of this thesis. For those that are interested, the CLEAN method is described in reference [55].

Chapter 3

Detector Development

In recent years, superfluid helium has come under increased scrutiny as a scintillation medium for detecting ionizing radiation. While quite low temperatures are necessary to liquify helium, and therefore experimental conditions are more difficult than with more conventional scintillators, certain experiments in fundamental physics can take advantage of superfluid helium's special characteristics (such as zero neutron absorption and low thermal excitation density) while simultaneously making use of its scintillation properties.

The scintillation from ionizing radiation events in liquid helium can divided into three parts: a prompt component, an afterpulsing component, and a phosphorescence component. These three processes are manifested on radically different time scales and it is chiefly the prompt component that is useful for detecting particle decays. This bright flash of EUV light is useful for detecting such events, and the development of detectors to capture the scintillation light is the subject of this chapter. Helium scintillation detectors based on wavelength-shifting fibers, fluor-coated acrylic tubes, and teflon sheets coated with evaporated fluors were developed for detecting the beta-decay of trapped ultracold neutrons. These detectors all share the property that they

use wavelength shifting fluors to convert the EUV scintillation light to visible light, which can then be transported out of the cryogenic apparatus to detectors at room temperature.

3.1 Fluor Development

Detector development for the neutron trapping experiment began with a measurement of the EUV yield of several fluorescent materials. These materials emit visible light upon the absorption of EUV radiation. Direct EUV detection, although possible with high efficiency, can be problematic due to the inability to transmit or guide EUV radiation to a detector; use of wavelength shifters alleviates this problem. In addition, wavelength shifting can significantly increase the number of photons available for detection.

The EUV scintillators tetraphenyl butadiene (TPB), p-terphenyl (TPH), and diphenyl stilbene (DPS) have emission spectra with peaks at 440 nm, 335 nm, and 409 nm respectively, each with widths of about 50 nm. They are all well suited for energy downconversion because of their high fluorescence efficiencies[56, 57, 58, 59, 60] and they can be evaporated into thin films, yielding adherent, durable coatings. The chemical composition of one of these fluors (TPB) is shown in Figure 3.1. In contrast to these evaporated films, fluor doped plastic films have the advantages of less light scattering, better abrasion resistance, ease of preparation, and index matching to plastic light guides[61]. These qualities have led to the consideration of using doped plastic films in several applications, including detection of Cerenkov radiation[62], ultraviolet imaging[63], and detection of dark matter[56]. However, fluorescence efficiencies of doped plastic films have been measured to be lower than their evaporated film counterparts at short wavelengths[56, 63].

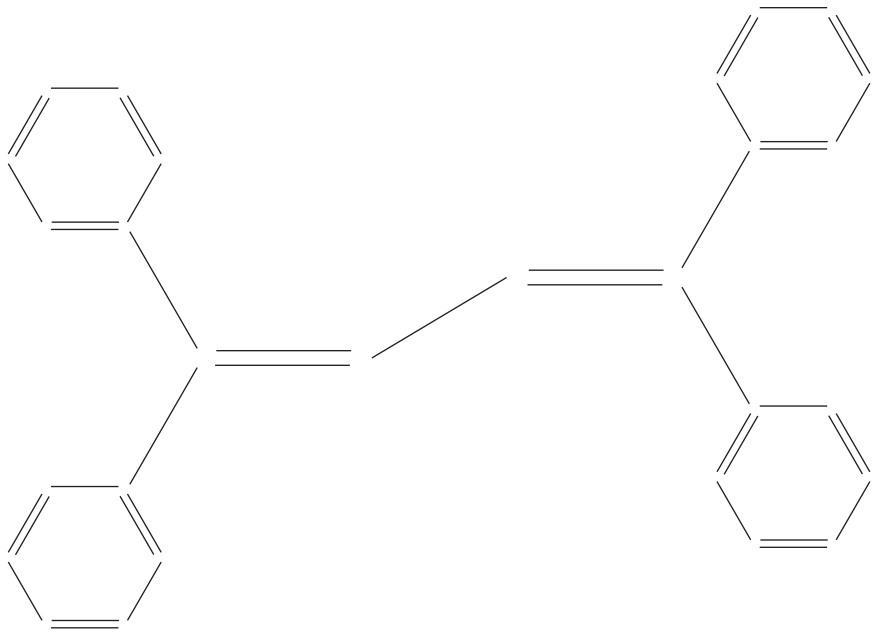

Figure 3.1: The chemical construction of tetraphenyl butadiene (TPB).

In this experiment, we performed studies of evaporated, sprayed, and doped plastic films under excitation by EUV light created in a radio frequency (RF) gas discharge. Optimum thicknesses and dopant concentrations for maximum fluorescence were determined, and fluorescence efficiencies of these films were measured relative to sodium salicylate. A reference standard of known absolute fluorescence efficiency[64], sodium salicylate has an emission spectrum peaked at 420 nm[65], with a width of about 80 nm. Fluorescent materials were deposited onto 25 mm x 10 mm x 0.81 mm nylon substrates[1].

Standard film deposition techniques were used to produce evaporated films of TPB, DPS, and TPH[2]. Evaporation was performed in a vacuum chamber evacuated

[1]Translucent off-white diffusing nylon 6/6 tape purcahsed from McMaster-Carr Supply Company, Dayton, NJ, catalog number 8730K15.

[2]TPB, TPH, and DPS were purchased from Aldrich Chemical Company Inc., Milwaukee, WI. Scintillators correspond to Aldrich catalog numbers 18,521-3, 25,738-

using a diffusion pump with a liquid nitrogen cooled baffle to less than 10^{-5} mbar. Film thickness was controlled by varying the distance from the molybdenum evaporation boat to the film substrate. Sample thickness is measured by weight, and ranges from 49 ± 6 μg cm^{-2} to 2650 ± 100 μg cm^{-2}, with uncertainties in thickness determined by the uncertainty in the weighing technique.

Sprayed phosphor coatings of sodium salicylate and TPB were prepared by airbrushing scintillator solution onto nylon substrates[3]. The scintillator solution consisted of either sodium salicylate dissolved in methyl alcohol or TPB dissolved in ethyl ether. Though easier to prepare, films made using this technique are less uniform than evaporated films. Film thickness was measured by weight, and ranged from 80 ± 40 μg cm^{-2} to 3040 ± 40 μg cm^{-2}.

Doped plastic films used in the EUV discharge source measurements were prepared by either a) controlled dipping of the substrate into a solution of the plastic and dopant, b) dripping the solution directly onto the substrate, or c) spinning plastic-dopant solution onto the substrate using a commercial spinner. In cases a) and b) the solutions consisted of 30 ml toluene per gram of plastic, with a varying concentration of fluor. Film thickness was measured using a micrometer. Dipped films are 12 ± 2 μm thick, while the films formed by dripping are 31 ± 2 μm thick. Chloroform is used as a solvent in the making of the spun films. Thicknesses of spun films (case c) range from 1.6 ± 0.1 μm to 40.1 ± 0.1 μm, as measured with a profilometer. The plastic used for most applications was pure polystyrene, with an average molecular weight of 280,000. Also tested are polyvinyltoluene (PVT), poly(2,4-dimethylstyrene)

9, and D21,375-6.

[3]Airbrush model CCAKCC, Paasche Airbrush Co., Harwood Heights, IL.

(PDMS)[4], polymethylmethacrylate (PMMA), nitrocellulose[5], long chain polystyrene (M.W. = 1,880,000), short chain polystyrene (M.W. = 2727), and dicarboxy terminated polystyrene[6].

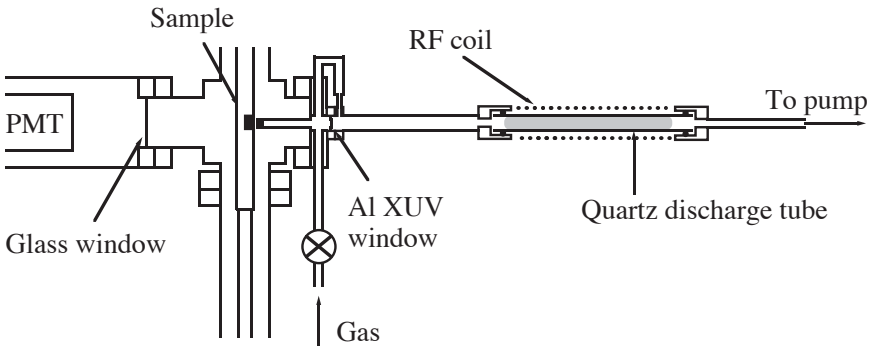

Figure 3.2: Apparatus used to measure fluorescence efficiencies of thin film samples.

Fluorescence efficiency measurements were performed by illuminating thin film samples with EUV light and measuring the intensity of the emitted fluorescent light with a photomultiplier tube (See Figure 3.2). The EUV source was a 66 MHz RF discharge in 99.999% pure helium (58.4 nm) or 99.995% pure neon (74.0 nm) gas. A continuous flow of gas through the system was required to maintain cleanliness. We found this to be important for maintaining a high EUV intensity. Visible and near UV light is filtered from the excitation spectrum by a 200 nm thick aluminum window[65]. The filtered spectrum consists solely of the desired EUV line. This was verified by measuring the output spectrum of the EUV system with a vacuum

[4]PDMS provided by Dr. R. G. Jones, Centre for Materials Research, University of Kent at Canterbury.

[5]Nitrocellulose was purchased from Ernest J. Fullam, Inc., Latham, N. Y., catalog number 11282.

[6]With the exception of PDMS and nitrocellulose, all plastic resins were purchased from Aldrich Chemical Company Inc., Milwaukee, WI. Plastics correspond to Aldrich catalog numbers 18,242-7, 18,282-6, 18,224-9, 32,781-6, 32,771-9, and 18,961-8.

ultraviolet spectrometer[7].

Twenty-one samples could be loaded into the apparatus at one time and could be interchanged and tested *in situ*. The EUV light emitted from the RF discharge illuminated a central area of 5 mm^2 on an individual sample. Scintillation light that entered into the diffusing nylon substrate has its direction randomized. This ensured that for a constant geometry, a fixed portion of light was collected by the bialkali cathode photo-multiplier tube (PMT) positioned directly behind the sample. The PMT was biased within the linear range of its voltage divider circuit. Comparison of the recorded anode currents, corrected for the wavelength dependent photocathode sensitivity, determined the relative fluorescence efficiencies of the samples. No fluorescence was observed for nylon substrates without scintillator coatings. Light attenuation through nylon was taken to be independent of the emission wavelengths of the tested samples.

Fluorescence of each film was compared to sprayed sodium salicylate, a standard with relatively constant response to ultraviolet radiation over a wide wavelength range. The absolute fluorescence efficiency of sprayed sodium salicylate, expressed in units of blue photons per EUV photon, was measured by Bruner[58] to be 0.42 for 58.4 nm excitation and 0.37 for 74.0 nm excitation. We normalize the fluorescence of each tested film to the average of at least five sodium salicylate samples. Based on the observed spread of the fluorescence yields of sodium salicylate and our samples, we estimate that relative fluorescence efficiency measurements of individual films are accurate to within 10%. No attempts are made to directly measure absolute fluorescence efficiencies.

The fluorescence efficiency ($F(\lambda)$) measurements of optimized evaporated, sprayed,

[7]Thanks to Martin Zombeck of the Center For Astrophysics at Harvard for the use of the EUV spectrometer.

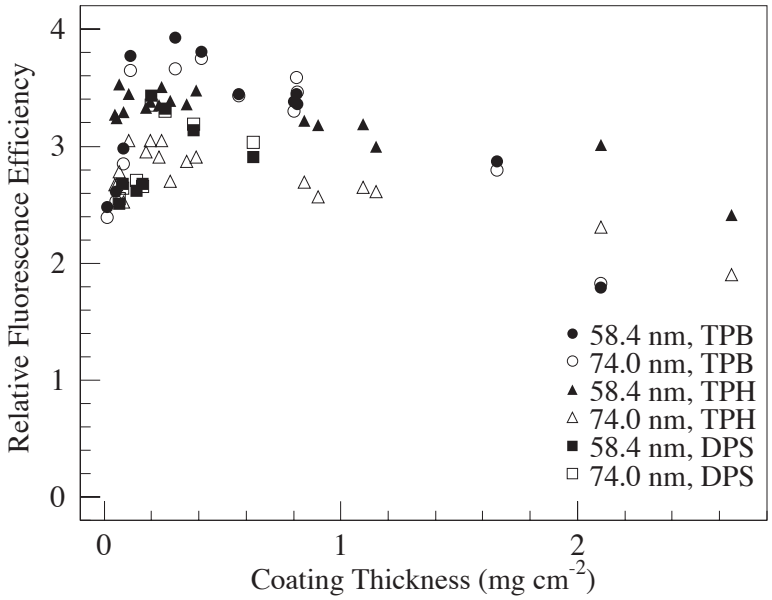

Figure 3.3: Relative fluorescence efficiencies of evaporated films excited by 58.4 nm and 74.0 nm radiation. All fluorescence efficiencies are specified relative to sodium salicylate.

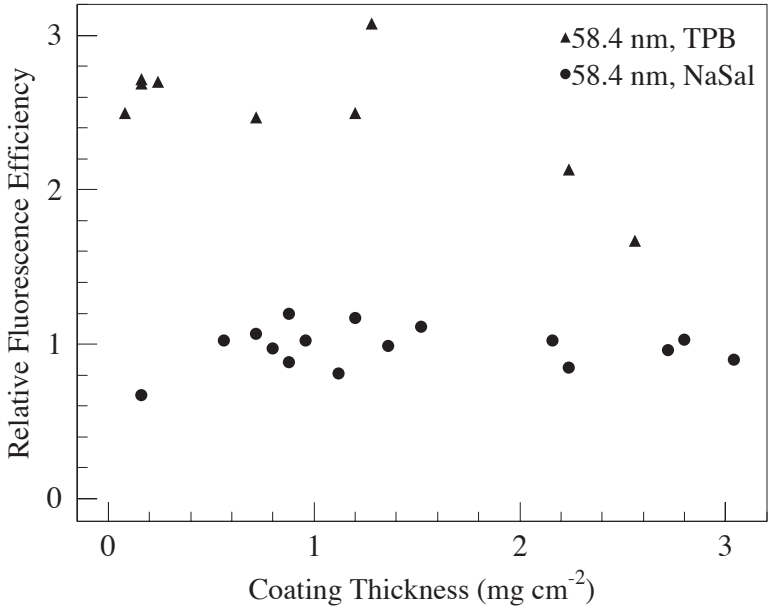

Figure 3.4: Relative fluorescence efficiencies of sprayed films excited by 58.4 nm radiation.

Scintillator	Thickness (mg cm^{-2})	F (58.4 nm)	F (74.0 nm)
TPB	0.2	3.9	3.7
TPH	0.1	3.4	3.0
DPS	0.2	3.4	3.3

Table 3.1: Values of the fluorescent efficiencies of optimized evaporated films relative to that of sodium salicylate.

and plastic-doped films are summarized in Tables 3.1 and 3.2 and Figures 3.3 and 3.4. As discussed earlier, these measurements are relative to sodium salicylate. Variation of fluorescence efficiency with coating thickness in evaporated films is shown in Figure 3.3. TPB yields the highest fluorescence efficiency, measured to be 3.9 ± 0.1 for 58.4 nm downconversion and 3.7 ± 0.1 for 74.0 nm downconversion, with an optimum coating thickness of 0.2 mg cm^{-2} (measured separately for each wavelength).

Scintillator	Matrix	Conc. (%)	F (58.4 nm)	F (74.0 nm)
TPB	polystyrene	≥ 2.0	1.00	0.76
TPB	polyvinyltoluene	≥ 2.0	0.81	-
TPB	poly(2,4-dimethylstyrene)	≥ 2.0	0.85	0.69
TPB	polymethylmethacrylate	10.0	0.35	-
TPB	nitrocellulose	13.3	0.40	-
TPH, POPOP	polystyrene	≥ 1.2	0.77	0.66

Table 3.2: Maximum values for the relative fluorescent efficiencies of doped plastic films relative to that of sodium salicylate.

The fluorescence efficiencies for sprayed films are shown in Figure 3.4. No vari-

ation with coating thickness is observed in sprayed sodium salicylate samples with thicknesses greater than 0.08 mg cm^{-2} (the thinnest tested in these experiments). Fluorescence efficiencies of sprayed TPB films are roughly two and a half times greater than those of the sodium salicylate films. The scatter of points is attributed to the nonuniformity of the sprayed films. The evaporated films show less spread and therefore appear to yield a more uniform coating.

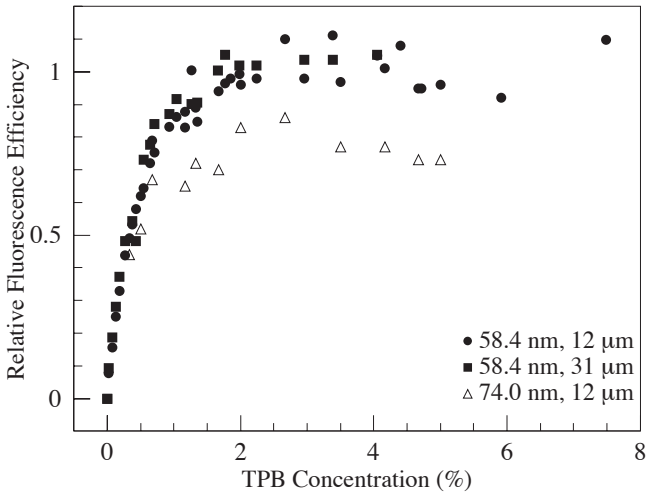

Figure 3.5: Fluorescence efficiencies of thin TPB-doped polystyrene films relative to sodium salicylate.

Figure 3.5 illustrates the effect of dopant concentration on the fluorescence yield of TPB doped polystyrene. EUV fluorescence efficiency depends strongly on TPB concentration at low concentration values, but begins to level off as the TPB concentration reaches 1% by weight. Furthermore, by measuring the fluorescence yield of spun films as a function of film thickness, we find that the relationship between fluorescence efficiency and TPB concentration does not depend on film thickness. Evidently, the absorption length of EUV light in TPB-doped polystyrene is much shorter than the film thicknesses used in this experiment. At low concentrations of TPB, fluorescence efficiencies are limited by EUV absorption by the polystyrene ma-

trix, while the maximum fluorescent yield at higher concentrations is limited by a second process, presumably excitation quenching of the TPB by the plastic matrix. PMMA and nitrocellulose based plastic films were found to yield lower fluorescence efficiencies than polystyrene based films.

Polystyrenes of varying molecular weight and chain termination were tested as matrix materials, showing no noticeable increase in fluorescence efficiency. Matrix materials similar to polystyrene were also tested, including PVT and PDMS, yielding similar results. This stands in contrast to the case of electron scintillators, where it is found that adding methyl groups to polystyrene can increase fluorescence as much as 59%[66, 67]. We attribute the lower fluorescence efficiencies of these materials to the difference in excitation mechanisms: electron scintillators are excited largely by energy transfer from the matrix to the fluor, while EUV light excites the fluors directly.

P-terphenyl was also tested in a polystyrene matrix. In order to shift all emitted light to the visible spectrum, a small (1500 ppm) amount of POPOP[68] was added. The relatively high fluorescent yield of TPH doped polystyrene suggests that widely used electron scintillators, usually doped with TPH and POPOP, could be used to efficiently detect EUV radiation. TPB is however the superior fluor for this application because of its high fluorescence efficiency and because it is less likely to crystallize in the film than TPH or DPS, allowing greater optical clarity.

In summary, fluorescence efficiencies of evaporated, sprayed, and doped plastic films at incident wavelengths of 58.4 nm and 74.0 nm were measured. Optimum coating thicknesses and dopant concentrations have been found for these films. We have found that the thick evaporated films necessary for efficient soft UV detection can be replaced by thinner, less opaque films when detecting EUV radiation. Evaporated

films of TPB, PTP, and DPS have been found to yield especially high fluorescence efficiencies. Doped plastic films are a useful alternative to evaporated films. Although they have lower fluorescence efficiencies than comparable evaporated films, they can be index matched to plastic light guides, avoiding the need for a secondary waveshifter for light guide coupling. In addition, tubes coated with transparent plastic films show significantly better transmission than tubes coated by evaporation, which can be an advantage. These clear films could also find use as sensitive coatings for EUV imaging systems, where low scattering and high transmission of the fluorescent light are important.

3.2 Fiber Cells

Our first cells built for detecting neutron decays in liquid helium were constructed using TPB and wavelength-shifting fibers. The idea was that the TPB would convert the EUV scintillation light from the helium into blue visible light, and then the fibers would convert the blue light to green light within their cores, trapping the green light and transporting it out of the cryogenic apparatus. The number of photoelectrons detected for each beta event can be expressed as

$$N = YF(1-S)Ce^{-\ell/\ell_{att}}\frac{S}{1-R(1-S)}Q$$

where Y is the EUV photon yield of the liquid helium, F is the fluorescence efficiency of the wavelength shifting fluor, S is the fraction of the wall surface covered by the wavelength shifting fiber, C is the conversion and capture efficiency of the wavelength shifting fiber, ℓ is the length of the fiber, ℓ_{att} is the attenuation length of the fiber, R is the reflectivity of the fluor coating, and Q is the quantum efficiency of the light detector.

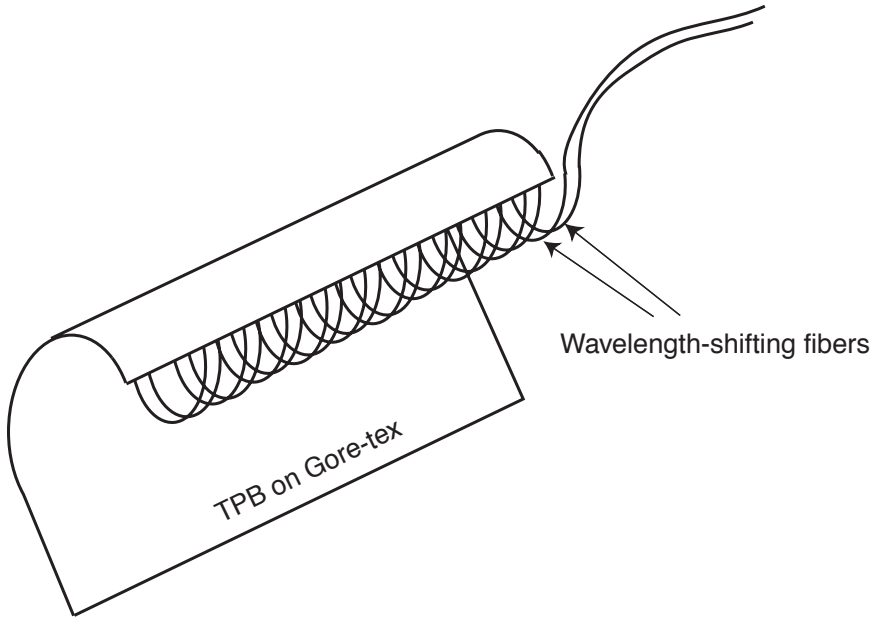

Figure 3.6: A fiber cell is built from pair of wavelength shifting fibers and a sheet of Gore-tex with TPB evaporated on its inside surface. The fibers are held in place with three boron nitride rods (not shown).

In our initial testing, the detection cells were each 15 cm long, and consisted of a Gore-tex sheet, three boron nitride rods, and two wavelength shifting optical fibers[8]. The fibers were bent into a double helix of diameter 32 mm and held in position using the BN rods. The Gore-tex was coated on one surface with evaporated TPB and wrapped into a tube[9]. This tube of Gore-tex, with TPB on its inner surface, was placed around the wavelength shifting fiber helix and held in place using Mylar tape. The detection cell assembly was then slid into a G-10 tube of inner diameter 38 mm. The fibers were held in place with three 3 mm x 3 mm x 150 mm rods of boron nitride, with 24 holes drilled in them (one every 6 mm). Thus each fiber had

[8]0.8 mm diameter double-clad Y11(250) fibers from Kuraray.

[9]Gore-tex gasketing material purchased from Big River Rubber and Gasket, Owensboro, KY (800) 626-7030 (www.bigriverrubber.com)

Table 3.3: Results for a variety of tests using WLS fiber based cells. Tests using the Cs-137 source could not be normalized per unit of energy deposition, as Cs-137 is an intense gamma as well as beta emitter. Here, ℓ stands for the length of each fiber and σ stands for the TPB coverage on the Gore-tex sheet.

Test	ℓ (m)	σ (μg/cm^2)	PMT	Source	Count rate (s^{-1})	Counts per 250 keV β	Remarks
1	0.9	55	8644	Cs-137	17881	-	
2	0.9	60	8644	Cs-137	13507	-	DPS used
3	0.9	58	8644	Cs-137	16281	-	
4	0.9	0	8644	Cs-137	1493	-	
5	0.8	95	8644	Cs-137	25158	-	d = 12 mm
6	0.9	173	8644	Cs-137	28578	-	
7	2.8	143	8644	Cl-36	2976	3.25	
8	2.8	240	R943-02	Cl-36	2613	2.83	thru window
9	2.8	231	R943-02	Cl-36	3597	3.89	ball lens
10a	3.9	160	R943-02	Cl-36	2153	2.33	PMT 1
10b			R943-02		1796	1.94	PMT 2
10c					457	0.50	Coincidence

12 coils, bent into a diameter of 32 mm. The construction of a fiber cell is shown in Figure 3.6.

Table 3.3 describes the series of tests on fiber cells that were completed in the summer of 1997. Tests 1 to 6 were done in a small dewar with a narrow neck, filled directly with liquid helium from storage dewar. A ^{137}Cs source could be raised and lowered vertically within the cell, allowing one to compare signals with and without helium excitation in the detection region. The Cs source emitted betas with an

endpoint energy of 514 keV, and its activity was measured to be 2830 betas per second using a pancake counter[10]. Tests using the Cs-137 source could not be normalized per unit of energy deposition, as Cs-137 is an intense gamma as well as beta emitter. One end of each fiber exited the dewar and pushed up against the front window of a single 19 mm diameter PMT[11] with heightened long wavelength response (quantum efficiency of about 12% at 500 nm). The cell tube was open at the bottom to allow liquid helium to enter the detection region. It was shown that TPB worked better than DPS (diphenyl stilbene, another fluor used for wavelength shifting EUV light), and that a 6 mm coil spacing worked better than a 12 mm coil spacing. By doing one run without any TPB on the Gore-tex, It was observed that the liquid helium from the storage Dewar fluoresced somewhat in the visible; this can be explained by frozen air impurities in the helium. Fluorescence from impurities in liquid helium has been observed in previous work[33].

Tests 7 to 9 were done in a tall 12.7 cm dewar. In this apparatus (see Figure 3.7), the G-10 tube was closed at the bottom with a copper flange. The fibers traveled up through the tube to Swagelok feedthroughs and exited the cryogenic apparatus. The G-10 tube could be filled with helium separately from the surrounding helium bath, and this allowed us to test cells using highly purified helium from a gas bottle. After filling the region outside the G-10 tube with liquid helium from a storage Dewar, the outer region could be pumped to lower temperatures, allowing the pure helium to be condensed within the cell. By varying the rate of pumping, the temperature of the cell could be lowered to 1.8 K. A superconducting wire level gauge allowed us to measure the level of helium within the G-10 tube.

[10]calibrated to within 10%

[11]Burle 8644

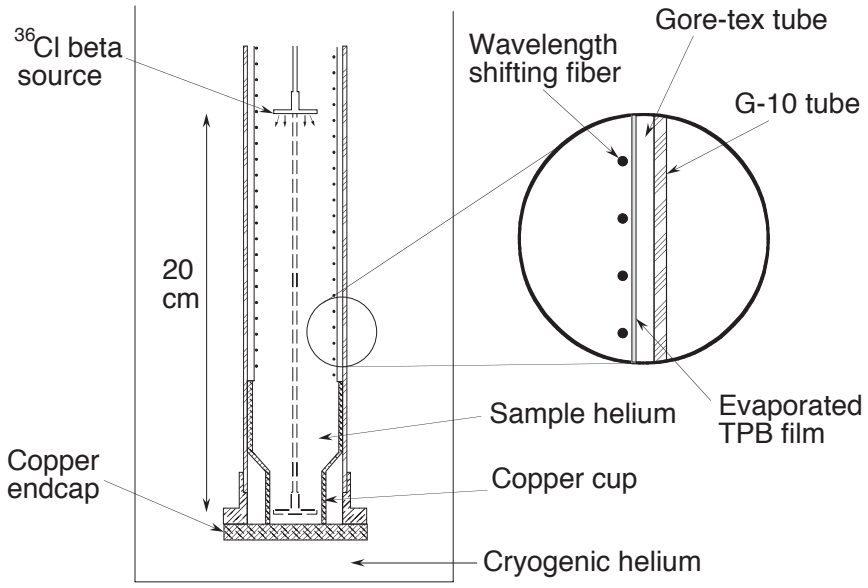

Figure 3.7: Diagram of the cryogenic apparatus used to test fiber-based detection cells.

Tests 7 to 9 were done using a ^{36}Cl source, whose beta decay spectrum (average energy 252 keV, maximum energy 710 keV) mimicked closely that of the neutron. This source had an intensity of 920 betas per second (measured using a pancake counter), and could be lowered or raised witin the cell using a motion feedthrough at room temperature at the top of the apparatus. By alternately lowering the source into a copper cup at the bottom of the tube and raising it into the center of the detector, a measurement of the helium scintillations could be performed. After doing a first test using the 19 mm photomultiplier, we switched to a photomultiplier with better response in the green[12]. This photomultiplier had to be cooled to achieve low dark counts[13], and had a recessed GaAs photocathode, making it more difficult to couple it to the fiber effectively. At first we simply sent the fiber light through an

[12]Hamamatsu R943-02, with a quantum efficiency of 19% at 500 nm.

[13]Peltier cooler purchased from Products For Research.

acrylic window, but later we found that a 10 mm ball lens could be used to focus the light from the fiber into the photocathode. With a TPB concentration of about 0.2 mg cm^{-2} we found that we could detect about 3.9 counts per β particle. This is comparable to the count rate predicted with the following assumptions:

Y = 11,000 ± 1,000 EUV photons for a 250 keV beta.

$F = 1.6 \pm 0.1$ for TPB.

$S = 0.12 \pm 0.01$ for a fiber coil every 6 mm.

$C = 0.025 \pm 0.002$ for the conversion and capture efficiency of the Y11 fiber (one end).

$\ell = 2.8 \pm 0.2$ m (the total fiber length from the center of the detector).

$\ell_{att} = 2.9 \pm 0.2$ m (the attenuation length of the wavelength shifting fiber).

$R = 0.75 \pm 0.10$ (estimated reflectivity of TPB)

$Q = 0.13 \pm 0.02$ (quantum efficiency of the R943-02 multiplied by optics efficiency)

These assumptions predict a total collection of $6.7\ ^{+2.7}_{-2.0}$ photoelectrons per 250 keV beta. This is somewhat greater than the observed 3.9 counts per beta. Obviously the large number of assumptions that go into this calculation make it rather uncertain. The error is dominated by the uncertainty in the reflectivity of TPB-coated Gore-tex. We have not yet measured this quantity; plain Gore-tex is known to have a reflectivity of 90%; the evaporation of TPB makes it visibly less white.

The cell used for the first attempt to detect trapped neutrons was 30 cm long (twice as long as the cells initially tested), with two fibers wrapped in helixes of opposite sense. Two sets of 15 cm long BN rods (6 rods total) and two Gore-tex sheets were used. Each boron nitride rod had 24 holes drilled through it, and each fiber was wound through two sets of boron nitride rods, so each fiber had a total

of 24 coils. All four fiber ends were taken out of the cryogenic apparatus. At first, all four fibers were fed into a single Hamamatsu R943-02 photomultiplier. However, we soon found that the neutron trapping apparatus suffered from a large quantity of neutron-induced luminescence, and we began running in coincidence, with the two ends of each fiber fed into its own PMT.

After approximately one month of beam time and failing to observe trapped neutrons because of the high levels of luminescence, we tested the efficiency of the larger cell. This test (number 10 in the table above) revealed that the light yield in each PMT was decreased significantly by the increased fiber length. The decrease in light yield is consistent with the 2.9 m light attenuation length in the wavelength shifting fibers. We found that only about half of the decay events were detectable in coincidence. Altogether, the fiber-based cells of the type used in the attempt to detect trapped neutrons yielded 4.27 photoelectrons per ^{36}Cl decay (summing the yield in the two photomultipliers). Since a large fraction (33 $\pm$ 10 %) of the photoelectrons came from triplet $He_2^*(a^3\Sigma_u^+)$ decay, this photoelectron yield must be multiplied by 66% $\pm$ 10 % to find the total number of photoelectrons in the prompt pulse. This fraction is estimated from the intensity of triplet molecule decay (see Chapter 4). Assuming a PMT quantum efficiency of 19 $\pm$ 1% and a light collection efficiency of 40 $\pm$ 10% for transport of the light from the fiber coils, through the 1.5 m of fiber between the coils and the photomultiplier, into the ball lens, and onto the PMT photocathode, one finds that the fiber cells yielded 224 $\pm$ 60 photons/MeV.

While the fiber-based cells never were demonstrated to have high light collection efficiencies, this sort of design may be useful in the future. Because the fiber has a small cross-section area, it can be snaked out of an apparatus without taking up

much room[14]. The fiber design was used initially in the neutron trapping experiment because it was felt that the neutron beam should not be stopped within the apparatus because of neutron activation and heat load issues. With this contraint removed, we turned to a second detector design, developed largely at HMI, Berlin by Klaus Habicht and Bob Golub[69].

3.3 Tube Cells

The second sort of detector insert used in the neutron trapping experiment was based on acrylic tubes whose inside surfaces were coated with TPB-doped polystyrene. This mixture was tested using the fluorescence efficiency rig (see Section 3.1) and found to have good EUV-to-visible conversion properties (F of 40%). Polystyrene doped with TPB is transparent and can be index matched to light guides, allowing efficient transportation of visible light out of the detection region. Based on this discovery, our collaborators at HMI began using TPB-doped polystyrene coated on the inside surface of acrylic tubes as a basis for helium scintillation detection [69].

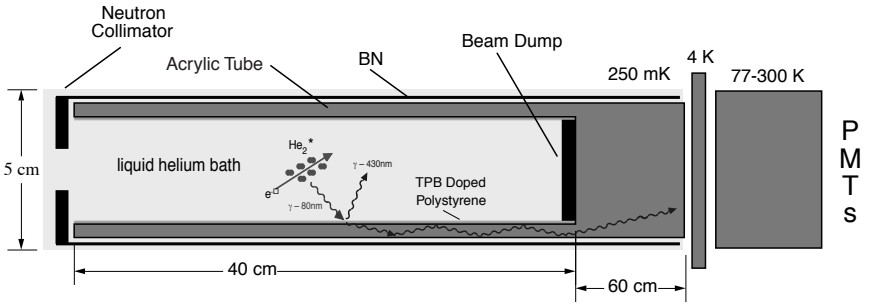

Figure 3.8: A sketch of the detector insert used in the 1999 neutron trapping run.

[14]The neutron EDM experiment may use fiber-based detection because the detection cell must be surrounded by magnetic shielding, whose effectiveness would be compromised by any large holes.

After we discovered large amounts of neutron-induced luminescence in our cell, we concluded that a more efficient detector insert was needed to boost the signal out of the single photoelectron noise. We abandoned the requirement that the neutron beam be able to pass through the apparatus, abandoned the wavelength shifting fiber-based cells, and instead investigated the possibility of using an acrylic tube-based design. In this approach (see Figure 3.8), the TPB-polystyrene coating converts the EUV scintillation light to blue light. About half of the blue light is then trapped in the tube walls, and a fraction of this light makes it to the end of the tube. This light then passes into an acrylic light guide, passing around a black boron carbide disc (the neutron beam dump). The light signal continues through two windows (at 200 mK and 4 K) and a light guide at 77-300 K, and then is detected using photomultiplier at room temperature.

The photomultiplier we used for these measurements was the Burle 8850. This 5 cm diameter tube has a bialkali photocathode and is maximally sensitive at 400 nm, well matched to the emission of TPB. But its most interesting property is its low gain dispersion. The term "gain dispersion" refers to the uncertainty in the size of the electronic pulse made by the photomultiplier, given a number of photoelectrons emitted by the photocathode. Because the gain dispersion of the Burle 8850 is so low, it is possible to distinguish one photoelectron events from larger events, based on the size of the signal from the anode of the PMT. This property of the Burle 8850 is illustrated in Figure 3.9. By requiring that events register more than one photoelectron, a cut on neutron-induced luminescence was possible. Of course, it was then necessary to ensure that actual neutron decays produced well more than a one photoelectron signal.

To optimize the design of the tube-based detector inserts, an apparatus was built

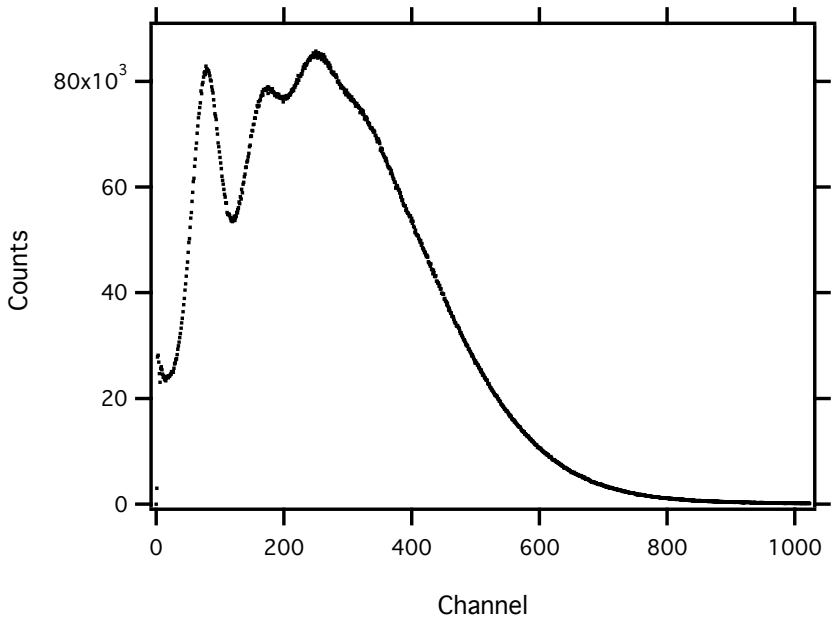

Figure 3.9: This figure shows the pulse-height spectrum observed when pulsing an LED into a Burle 8850 photomultiplier, making an average of 3 photoelectrons per pulse. Each bump corresponds to a different number of photoelectrons, allowing precise discrimination based on photoelectron number.

to test them individually. This apparatus is shown in Figure 3.10. It consists of a long G-10 tube, suspended along the vertical axis of a Dewar that could be filled with liquid helium. At the bottom of the G-10 was attached a brass flange. The G-10 tube could be closed by fastening a copper flange to the bottom with an indium seal. In the bottom of the G-10 tube is placed a 40 cm-long, 3.8 cm diameter, transparent acrylic tube. Its wall thickness is 3.2 mm, and its inner surface was coated with TPB-doped polystyrene. Centered in the acrylic tube, held from below by a stainless steel rod, was a radioactive source; this could be either an α source (^{210}Po or ^{241}Am) or a β source (^{113}Sn). Butting up against the acrylic tube from above is a 3.8 cm diameter acrylic light guide that travels up to room temperature. A 5.1 cm diameter acrylic plug stands above the top of the light guide, and an O-ring vacuum seal is made against the plug. Above the the plug, index matched to it using optical grease, is a

PMT facing down into the light guide. The photomultiplier is enclosed within a metal housing to protect it from helium gas, which can diffuse into the glass photomultiplier tube causing it to create afterpulses, and eventually destroy it.

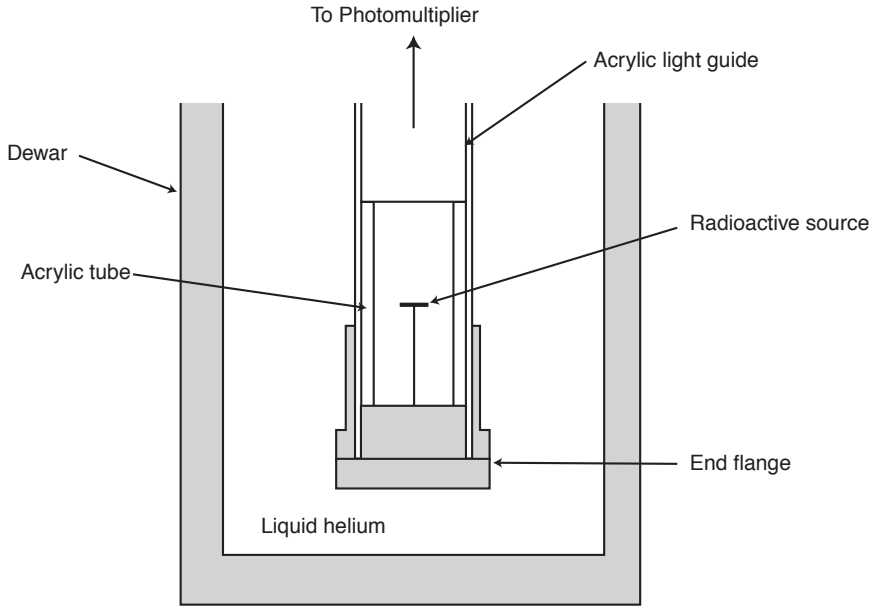

Figure 3.10: Apparatus used to measure the relative efficiencies of detection inserts based on TPB-coated acrylic tubes. (Not to scale.)

The G-10 tube can be filled with high purity helium gas[15]. By filling the dewar with liquid helium and pumping on it, the helium gas inside the G-10 tube could be condensed to liquid and cooled. When the acrylic tube was filled with liquid helium, scintillations induced by the radioactive source could be detected by the

[15]Helium content 99.999%. The helium is also passed through a liquid helium-cooled tube filled with copper mesh before entering the cell.

photomultiplier at room temperature. The PMT signal was fed to a charge preamp[16] and thence to a scintillation amplifier[17] and multichannel analyzer. Pulse-height analysis was performed on the resulting distribution of signal sizes. By comparing the scintillation peak position with the position of the one photoelectron peak, the average number of photoelectrons made by a scintillation events could be determined. The construction of the acrylic tube could then be varied in attempts to optimize the design of the detector insert.

The acrylic tubes were coated with TPB-doped acrylic through a careful procedure. First, the acrylic tube was cut to length (40 cm) and its ends polished. Only ultraviolet transmitting grade (UVT) acrylic was used to maximize blue light transmission. Then a mixture of research grade toluene, crystalline TPB, and polystyrene pellets was stirred and heated within a beaker. When the mixture was dissolved and warm, the acrylic tube was lowered about 1 cm into the liquid. The top of the tube was covered with a rubber plug with a hole in the center. Leading from the hole was a rubber hose with a valve midway thru its length, and the far end of the hose terminated at a pump. By carefully throttling the valve, the liquid could be sucked up into the acrylic tube. After a few seconds, the pump was shut off and the liquid level allowed to slowly drop (over a 20 second period). The tube was then set aside to dry. When dry, the tube was wrapped with Tyvek paper[18] to protect the tube.

A variety of tests were performed on the acrylic tube-based detector inserts. These tests are summarized in Table 3.4. Most of the early tests were done using a high energy alpha source, so as to have lots of scintillation signal. It was found that a

[16]Canberra 2005

[17]Shaping width 1 μs

[18]DuPont Chemical Corporation.

Table 3.4: Results for a variety of tests using acrylic tube-based cells

Test	Date	Source	Excitation	PMT	Peak signal (p.e.)	Remarks
1	6/20/98	Po-210	5.3 MeV α	8850	177	HMI cell, 40 % TPB
2	6/22/98	Po-210	5.3 MeV α	8850	73	40% TPB, center blocked
3	6/24/98	Po-210	5.3 MeV α	8850	112	4% TPB
4	6/26/98	Po-210	5.3 MeV α	8850	146	TPB on Gore-tex
5	9/20/98	Am-241	5.5 MeV α	8850	147	12% TPB
6	9/20/98	Am-241	5.5 MeV α	8850	112	4% TPB
7	2/5/99	Am-241	5.5 MeV α	8850	145	8% TPB
8	2/5/99	Am-241	5.5 MeV α	8850	144	8% TPB, dewar helium
9	2/11/99	Am-241	5.5 MeV α	8850	40	2% TPB, center blocked
10	2/13/99	Am-241	5.5 MeV α	8850	72	30% TPB, center blocked
11	2/23/99	Sn-113	364 keV β	8850	18.5	40% TPB
12	2/24/99	Sn-113	364 keV β	8850	5.5	neutron cell; 40% TPB
13	2/28/99	Am-241	5.3 MeV α	8850	62	40% TPB, center blocked
14	3/6/99	Sn-113	364 keV β	8850	8.5	40% TPB, center blocked

TPB concentration of 30% to 40% (TPB to polystyrene by weight) yields the highest signals, though TPB concentrations as low as 8% gave as much as 80% of the optimal signal. Attempting to achieve more than 40% TPB concentration generally resulted in TPB crystallization, spoiling the optical properties of the tube. It was also found that blocking the center of the tube dropped the signal yield by 60%, showing that most of the light was not traveling inside the tube walls. Results similar to these were reported by out HMI collaborators[69].

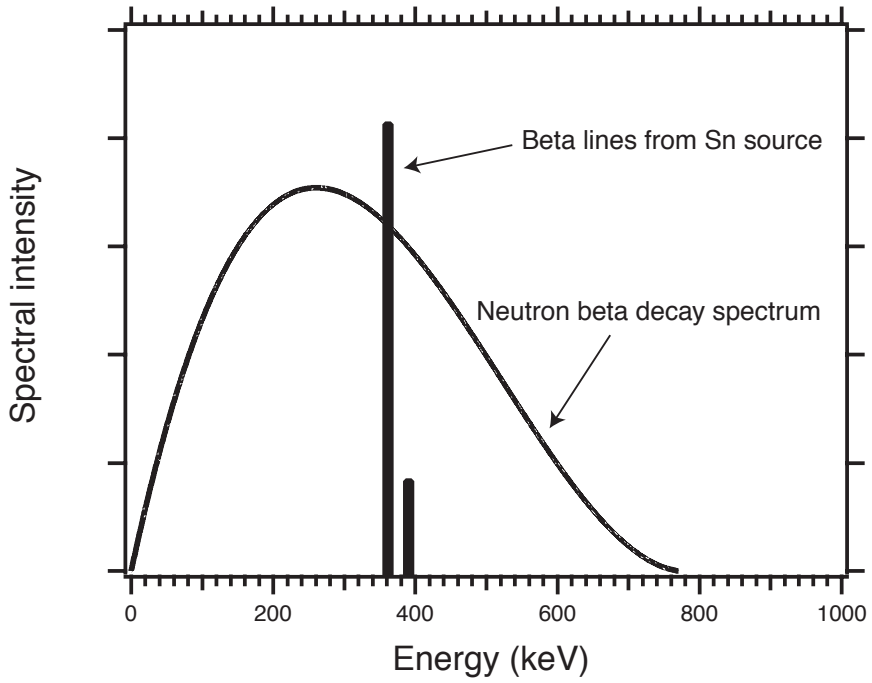

Figure 3.11: The beta-decay spectrum of the neutron, superimposed with the ^{113}Sn beta spectrum.

Later, tests were performed using ^{113}Sn, a conversion beta source with a line energy of 364 keV. This source was chosen because 364 keV is a comparable energy to that released in neutron beta decay (see Figure 3.11) and because a monoenergetic line is more easily identified in a pulse-height spectrum than a broad beta decay spectrum. The results of three of these tests are shown in Figure 3.12. Depending on

whether the center of the cell was blocked with a black neutron beam dump, either 8.5 or 18.5 photoelectrons could be detected per ^{113}Sn decay. When one of these cells was placed within the neutron trapping experiment along with the ^{113}Sn source, an average of 5.5 photoelectrons was detected. The decrease in average pulse size was due to a more complicated, less efficient, set of optics for transporting the light to room temperature.

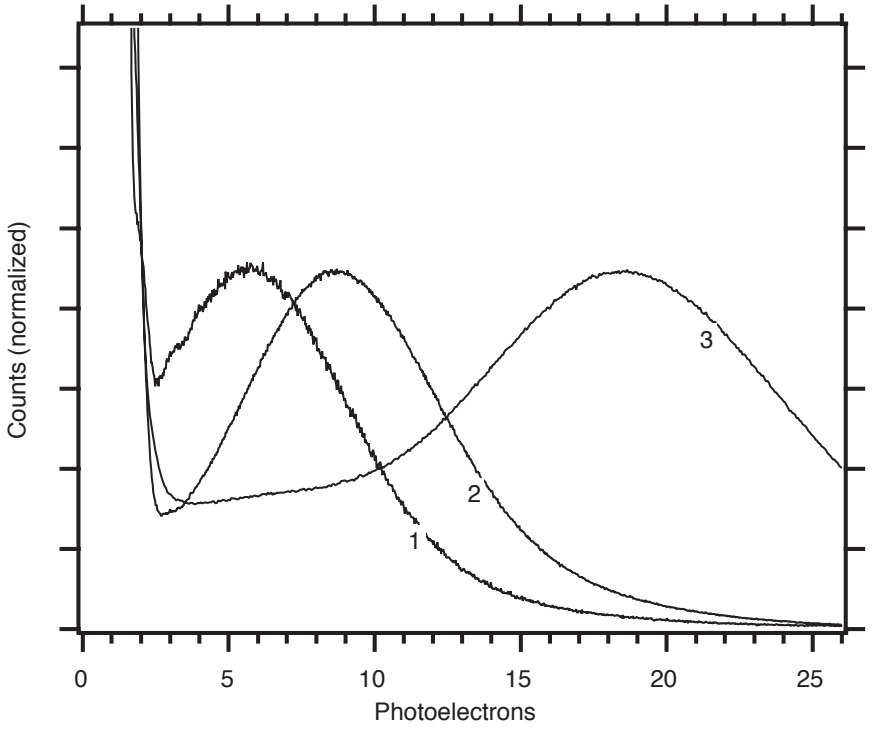

Figure 3.12: Three calibration runs of acrylic tube-based scintillation detectors. A ^{113}Sn source, emitting β particles at 364 keV, is used to create pulses of EUV light in the liquid helium. Curve 1 shows the response of a cell used to detect trapped neutrons in April-May 1999. Curve 2 shows the response of a similar cell tested in a cell testing rig. Only light passing through the acrylic wall is allowed to pass; the rest is clocked by a black neutron beam stop. Curve 3 shows the response of a cell without the center blocked.

The intensity of the scintillation signal was also measured as a function of source position. By attaching an alpha source to a string and installing an arrangement

of hooks within the cell over which the string traveled, the vertical position of the alpha source could be varied along the length of the acrylic tube. This roughly linear variation in signal is shown in Figure 3.13.

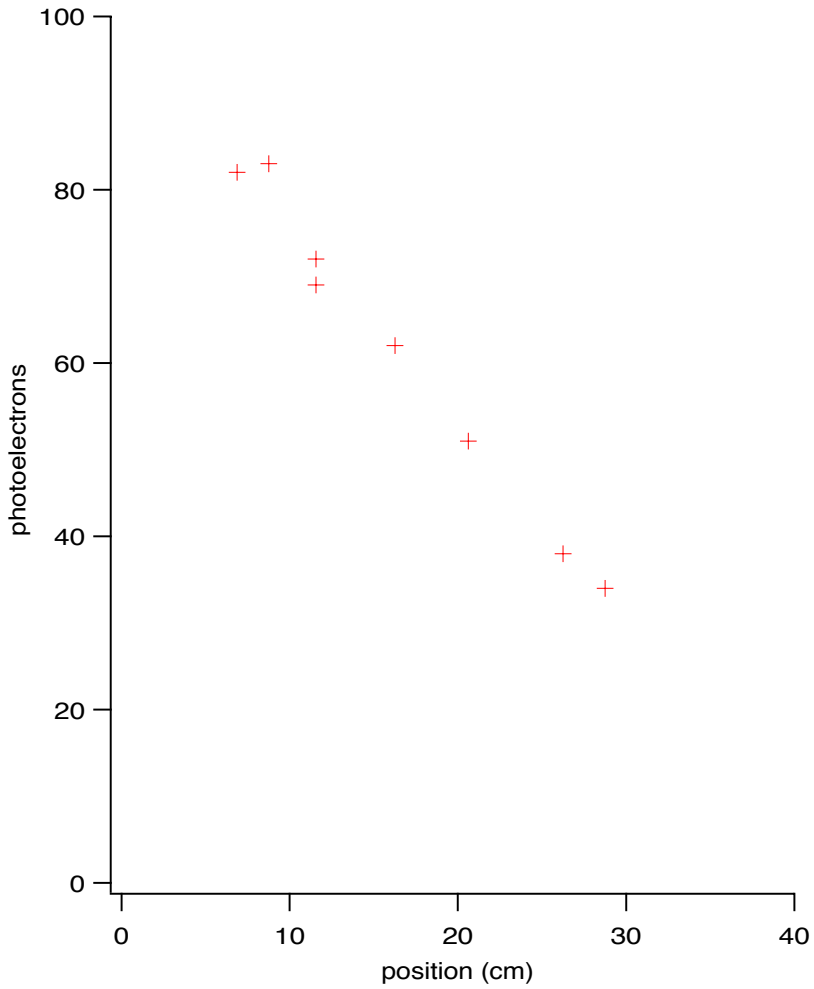

Figure 3.13: Position dependence of the scintillation signal for the tube-based detector.

The efficiency of the light guide in the tube cell testing rig was measured by attaching a piece of organic scintillator with a beta line source attached, alternately to the end of the light guide (so that the light from the scintillator traveled up the light guide and into the PMT) and directly to PMT itself. It was found that the light

guide is 31% efficient. Given that the Burle 8850 has approximately a 20% quantum efficiency for detecting blue light, it follows that about 140 photons per ^{113}Sn beta event are released from the end of the acrylic tube if its center is blocked, and about 300 photons if it is not. Given the high EUV yield of liquid helium (22,000 photons per MeV for β particles) it follows that only 3.8% of the EUV photons released in the liquid helium result in a blue photon exiting upward into the light guide, and this number drops to 1.8% if the center is blocked. This low yield of blue photons is a combination of the fluorescence yield of TPB doped polystyrene (approximately 25%) and the transmission of the acrylic tube (6.9% in the tube wall, 8.3% down the center). Of course these numbers would be different for a different acrylic tube; a larger wall thickness or shorter tube would increase these numbers significantly.

3.4 Gore-tex Cells

One of the results (number 4) shown in Table 3.4 revealed that a cell built using a sheet of Gore-tex rolled into a tube, with TPB evaporated on its inside surface, could also perform well as a detector. However, since there is no tube wall to propagate light around the beam dump, all the light extracted from a Gore-tex cell must come down the center. Therefore, a black beam dump makes the use of a Gore-tex cell impossible. However, after 1999 we put significant effort into developing a transparent beam dump, one that could both absorb the neutron beam and pass scintillation light. Eventually we chose to use a cylinder of high purity boron oxide B_2O_3 as a beam dump. The program of transparent beam dump development is described in Chapter 5.

Because our new magnetic trap has a larger bore diameter (105 mm) than the previous one (51 mm), the light emitted from a Gore-tex cell is now more easily

collected. In addition, evaporated TPB has a higher fluorescence efficiency than TPB-doped polystyrene. For larger bore detectors, with easier optical access to the trapping region, the Gore-tex cell proved superior. The number of photoelectrons collected using this detector insert is higher than in previous cell designs. In March, 2001, a calibration run was performed in the neutron trapping apparatus which was equipped at the time with this type of detector. Using a Burle 8854 photomultiplier (quantum efficiency 17%) a prompt peak of 35 photoelectrons was seen. The optics transmission efficiency at the time is estimated to be 49% (this was before the optics were modified to reduce infrared heating, see Chapter 5); thus about 1150 photons leave the Gore-tex tube per MeV of beta energy deposition. This type of detector was used to detect trapped neutrons in August, 2001, and will be discussed in more detail in Chapter 5.

Table 3.5 summarizes the results of this chapter. It shows the efficiencies of the various detector technologies for turning helium scintillation events into detector photoelectrons. The "Photons/MeV" column specifies the estimated number of photons that escape the trapping region. The "Optics" column specifies the estimated chance that a photon passes from cryogenic temperatures to a detector at room temperature. The "QE" column specifies the quantum efficiency for the photomultiplier used in that measurement. The "P.E./MeV" column specifies the estimated efficiency for turning a single beta excitation in the liquid helium into prompt photoelectrons in the detector.

Table 3.5: Summary of detector efficiencies

Detector type	Photons/MeV	Optics	QE	P.E./MeV
Wavelength shifting fibers	224 ± 60	40 ± 10%	19 ± 1%	17 ± 2.6
Acrylic tube (center blocked)	377 ± 57	31 ± 3%	20 ± 2%	23.4 ± 1.4
Acrylic tube (center open)	819 ± 116	31 ± 3%	20 ± 2%	50.8 ± 1.4
TPB evaporated on Gore-tex	1150 ± 203	49 ± 5%	17 ± 2%	96 ± 8.0

Chapter 4

The Physics of Liquid Helium Scintillations

This chapter describes several experiments designed to investigate the time dependence of EUV fluorescence following ionizing radiation events. It is found that both alpha and beta particles create an afterpulsing tail that decays exponentially with a 1.7 μs time constant. It is speculated that this exponential tail results from the reaction of He(2^1S) atoms with the liquid helium. Another discovery is that alpha particles create an additional fluorescence tail whose intensity varies as 1/time, that the intensity of this tail depends on the temperature of the superfluid helium, and that this long-lived scintillation tail is not created by beta particles to any substantial degree. It is also found that liquid helium phosphoresces on the time scale of many seconds; this remarkable property is a result of the radiative de-excitation of triplet helium excimers and exhibits an exponential time constant of 13 $\pm$ 2 s.

4.1 Prompt Scintillation

After an ionizing particle passes through liquid helium, a large number of excited atoms, free electrons, and ions are created. The energy deposition per unit length depends strongly on the charge and mass of the exciting particle. This variation in dE/dx has a big effect on the dynamics of the particles created by the track. For example, because a high energy electron deposits on average 50 eV/μm and the average energy to produce an ion-electron pair is is 42.3 eV, it follows that ionization events are on average 850 nm away from each other. With an average separation of 10 nm between the ion and its lost electron, it is clear that ion-electron pairs are well separated under beta excitation[70]. But under alpha excitation, this is not the case. If the excitation is an alpha source, the deposition is 2.5×10^4 eV/μm, and therefore the average spacing between events is only 2 nm.

In any case, the excited atoms, electrons, and ions quickly thermalize with the liquid helium. The electron, once thermalized, forms a bubble in the liquid, pushing away surrounding helium atoms. Experiments on electron bubbles show that the bubble formation happens within 4 ps[71]. The bubble displaces a large number of helium atoms; therefore the electron has a large effective mass ($m \sim 240$ helium atoms), and moves slowly throught the liquid.

The He^+ ion reacts within 100 - 500 ps with the surrounding helium to form He_2^+. It forms in a high vibrational state[72, 73], but soon drops to a lower vibrational state through inelastic collisions with surrounding helium atoms. Then the He_2^+ ion can react again to form a triatomic ion:

$$He_2^+ + He \rightarrow He_3^+.$$

This ion is thought to then form the core of a helium "snowball", which forms within 5 ps[74]. In a snowball, surrounding helium atoms are attracted to the He_3^+ ion. The

snowball has an effective mass of 40 helium atoms and thus has a large effective mass (though not as large as the electron bubble).

As mentioned earlier, the average distance between the electron bubble and its parent ion is 10 nm. Based on this initial separation and the effective snowball mass, the average recombination time is 0.3 ns for electron excitation. The ion production and recombination process has been studied carefully by Benderskii *et al.* [75]. A helium snowball will react with a free electron as follows:

$$(\mathrm{He}_3^+)_{\mathrm{snowball}} + (\mathrm{e}^-)_{\mathrm{bubble}} \rightarrow \mathrm{He}_2 + \mathrm{He}.$$

This reaction is the source of large numbers of He_2 molecules, produced in both triplet and singlet states. While the ratio of singlet and triplet formation rates found in in low-density gases normally approaches a 1:3 statistical weight, it is found that molecular formation in liquid helium exhibited relatively more singlet formation if the helium is excited by a high energy electron. This is attributed to the fact that most electrons do not escape from their parent helium atom following ionization of singlet ground state helium atoms. This makes it overwhelmingly likely that a given liberated electron will recombine with its parent if the excitation is produced by a high energy electron. However, if the excitation is created by an alpha particle, then the ions are created much closer together, Then it is much more likely that a given electron will not recombine with its parent, and the triplet/singlet ratio will approach 3:1.

The claim that ionic recombination is the chief source of He_2 molecules is buttressed by the measurements done by Roberts *et al.*; in these experiments an electric field applied to the helium strongly attenuates the scintillation pulse (as much as 60%).

Even if there is a high electric field, significant scintillation is produced by helium

atoms. Excited atoms are also produced, 0.45 per ion[76]. Again, because the initial helium atom is a singlet state, the excited atom is also likely to be in a singlet state. Of these, 83% are in the singlet state, and 17% are in the triplet state, when excited by electrons. It is well known that triplet atoms willl react with the surrounding helium to form triplet He_2 molecules. There is however a 60 meV activation energy for this reaction to occur[43]. It is believed that the high liquid density makes molecule formation more likely, as the $He^*(2^3S)$ - $He(1^1S)$ potential can be affected by the presence of a third atom. It has been found that $He^*(2^3S)$ atoms react to form $He_2^*(a^3\Sigma_u^+)$ in 15 μs, but the time required to form $He_2(A^1\Sigma_u^+)$ molecules from $He(2^1S)$ atoms has not yet been measured[40, 41].

In our case (with no electric field present), the prompt pulse of EUV light created immediately after an ionizing radiation event is due mainly to the radiative decay of $He_2(A^1\Sigma_u^+)$ molecules, which have been formed largely through electron recombination. The shape of the initial scintillation pulse was studied carefully by Klaus Habicht, and a more detailed discussion can be found in his thesis[69]. The pulse shape that we observe has a fast rise time (about 5 ns), and a 1/e decay time of 10 ns. This 10 ns decay time represents an upper limit on the lifetime of the $He_2(A^1\Sigma_u^+)$ molecule molecule, but certainly includes other effects such as the emission lifetime of the TPB and the response time of the photomultiplier.

4.2 Afterpulsing

After the prompt pulse eliminates the $He_2(A^1\Sigma_u^+)$ molecules, other electronic excitations remaining are singlet atoms, triplet atoms, and triplet molecules. The interactions between these species within the ionizing track can result in more scintillation light following the prompt component. Because the excitation density depends on

the kind of ionizing radiation, different ionizing particles can exhibit different pulse shapes. As the excitation track spreads in size and excitations are removed, the rate of reactions decreases. The pulse shape and intensity can therefore depend on the mobility and density of these excitations.

We observe a strong exponential tail following the prompt pulse, with a 1.7 μs lifetime. This tail is created from both alpha and beta excitation. An experimental trace illustrating this decay is shown in Figure 4.1. This trace was taken by triggering a multichannel scalar (MCS) [1] on the prompt pulses from a ^{113}Sn source in a Gore-tex-based detector (see Chapter 3) and counting single photon afterpulses. The average number of photoelectrons in the main pulse was 12. The cell used in this test is the same cell used to detect magnetically trapped neutrons in August, 2001, and was made of a Gore-tex tube coated with an evaporated layer of TPB. The cell was viewed by a photomultiplier with high gain and good single photoelectron resolution[2]. It should be noted that this 1.7 μs lifetime is demonstrably not a result of a slow component in the TPB fluorescence decay; this can be seen from the results of Klaus Habicht [69], where it is shown that the scintillation curve in cold *gaseous* helium exhibits a considerably different time dependence on μs time scales. One would not expect the TPB lifetime to depend on whether the cell contains liquid or gaseous helium; therefore the 1.7 μs lifetime seen here is evidence of a reaction in the helium.

As can be seen from the above fit, the afterpulsing from beta particles fits well to a single exponential, with a 1.7 μs decay lifetime and total intensity $A\tau$ of 3.3 photoelectrons. This scintillation tail probably derives from a metastable entity reacting with the background helium. A plausible candidate is the metastable atom

[1] SRS model SR430, Stanford Research Systems, Sunnyvale, CA

[2] Burle 8854 photomultiplier, Burle Industries, Lancaster, PA

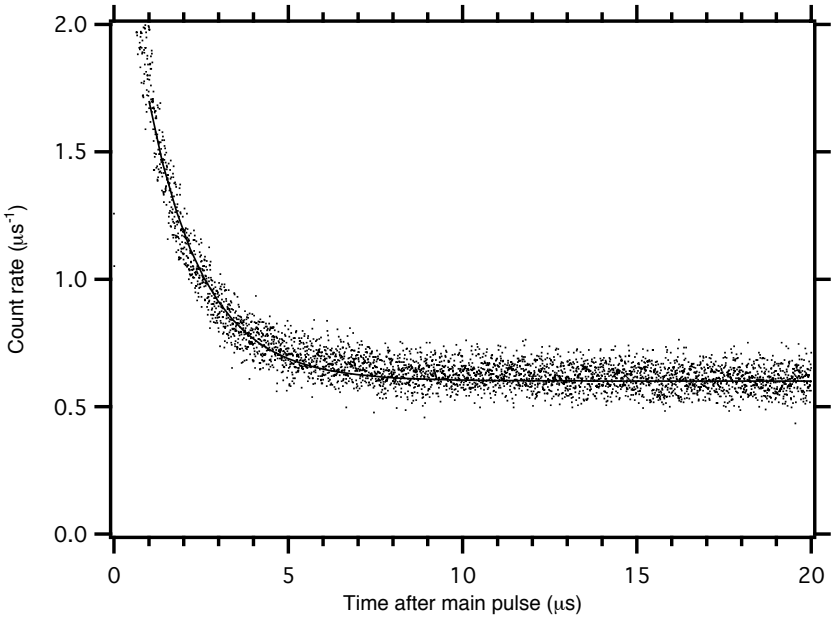

Figure 4.1: Afterpulse intensity from a beta source, as a function of time, plus a fit to the function $Ae^{-kt} + B$, where t is measured in μs. The background B is 0.6005 $\pm$ 0.0004 μs^{-1}, the amplitude A fits to 2.07 $\pm$ 0.02 μs^{-1}, and k fits to 0.633 $\pm$ 0.005 μs^{-1}. This data was taken at a temperature of 250 mK using a Gore-tex cell. There is an average of 12 photoelectrons in the main pulse (first 1.0 μs), and the total intensity of this exponential tail is 3.3 photoelectrons.

He(2^1S), which has a vacuum lifetime of about 1 second. There is evidence from spectroscopic measurements of electron-beam excited liquid helium that this particular atom species reacts with the surrounding helium atoms to form the $He_2(A^1\Sigma_u^+)$ molecule, which then can radiatively decay immediately[44]. Though the timescale of this process has never been measured, a similar reaction with He(2^3S) atoms has been shown to occur with a 15 μs characteristic lifetime[41].

This exponential lifetime is also found in alpha-induced scintillations[69]. But in addition it is found that a second component is present, decaying with a 1/time dependence. This decay can be seen in Figure 4.2, which shows the decay curve of afterpulsing in an acrylic tube-based cell. The source of this component is uncertain,

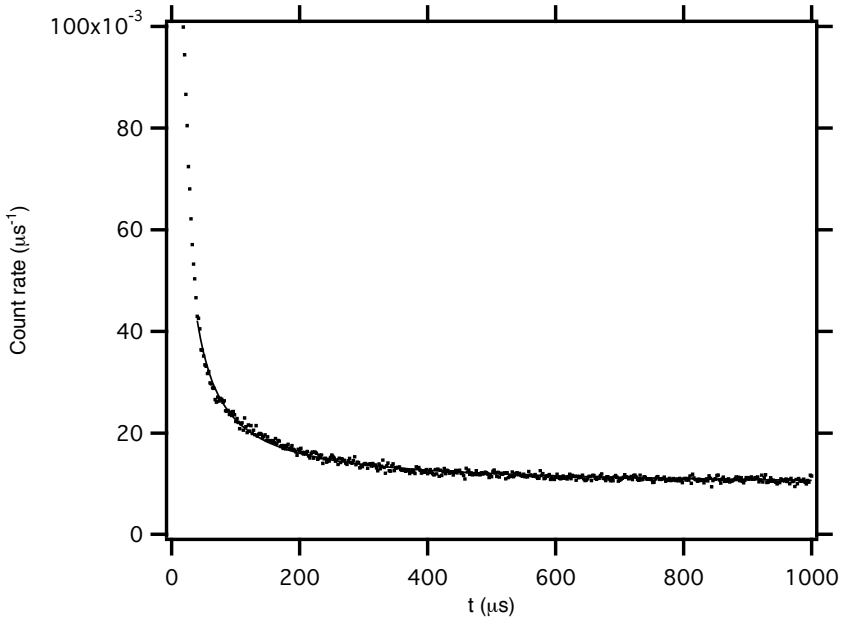

Figure 4.2: Afterpulse intensity as a function of time, plus a fit to the function At^p+B, where t is measured in μs. The background B is 0.009353 $\pm$ 0.00003 μs^{-1}, and the amplitude A fits to 1.25 $\pm$ 0.03 μs^{-1}, and p fits to -0.987 $\pm$ 0.005. This data was taken at a temperature of 1.8 K using an acrylic tube-based cell. There is an average of 146 photoelectrons in the main pulse.

though there are several possible mechanisms. A strong clue as to its source is the fact that this component is not present in beta excitation. The main difference between alpha and beta excitation is the density of ionization; beta sources in liquid helium will have a path length on the order of 1 cm, while an alpha will only travel about 2.5×10^{-2} cm[77]. Therefore it is probable that the mechanism relies on multi-body interactions; it does not derive from a species interacting solely with the surrounding ground-state helium, as is the case with the purely exponential decay discussed above. Another clue is that there are not many species that are known to be stable for long times in liquid helium and carry enough energy to make photons: metastable $He_2^*(a^3\Sigma_u^+)$ molecules, free electrons, and ions. There are then three distinct models that come to mind: $He_2^*(a^3\Sigma_u^+)$ molecules interacting with each other, $He_2^*(a^3\Sigma_u^+)$

molecules interacting with ions or electrons, or from ions and electrons recombining. Let us examine each of these models in turn:

Metastable-metastable interactions

Metastable-metastable interaction is a well known phenomenon in organic scintillators. In these materials, as in liquid helium, both singlet and triplet states are excited. And as in liquid helium, the singlet states decay rapidly, leaving triplet states still carrying chemical energy from the original ionizing event. Following King and Voltz[78], the concentration of triplet states c_T then evolves as

$$\frac{\partial c_T(r,t)}{\partial t} = D_T \nabla_r^2 c_T(r,t) - \chi_{tt} c_T^2(r,t) - \frac{1}{\tau_T} c_T(r,t),$$

where D_T is the triplet diffusion coefficient, χ_{tt} is the triplet destruction coefficient, and τ_T is the triplet lifetime. In this model, triplet destruction can feed singlet creation. If triplet destruction can create singlets with rate k_{tt}, then light will be produced at a rate proportional to $\chi_{tt} k_{tt}$. Thus triplet-triplet interactions can feed a short-lived scintillation component. In liquid helium, an appropriate mechanism for triplet-triplet annihilation is Penning ionization, for which the reaction rates have been measured previously[40]. The alpha track in liquid helium is approximately 60 nm in diameter and 2.5×10^{-2} cm long[70].

The above equation is non-linear, and must be solved using approximation methods. The triplet decay term $\frac{1}{\tau_T} c_T(r,t)$ can be ignored, as the triplet lifetime is very long compared to the time scale of the track dynamics. It can also be seen that, in the pure diffusion equation without triplet annihilation, that the triplet density at the center of the track decreases with a time constant $t_d = r_0^2/4D_T$, where r_0 is the initial width of the track, assumed here to be cylindrically symmetric and Gaussian,

i.e.

$$c_T(r,0) = c_T(0)e^{-(r/r_0)^2}.$$

On the other hand, if there were no diffusion, then the density of triplets would decrease entirely through triplet-triplet destruction with a characteristic lifetime $t_{tt} = 1/(\chi_{tt}c_T(0))$. Depending on whether t_d or t_{tt} is smaller, either diffusion or annihilation controls the process.

Under the approximation that the track continues to be Gaussian as the track expands, the rate of singlet radiation from triplet annihilation $I'(t)$ can be shown to be[78]

$$I'(t) = \frac{k_f k_{tt}\tau_s}{2\chi_{tt}t_{tt}} \frac{N_T(0)}{\left[1+\frac{t_d}{2t_{tt}}\ln(1+\frac{t}{t_d})\right]^2 (1+\frac{t}{t_d})}.$$

For the case of alpha particles in liquid helium, this expression can be simplified. After the alpha particle excites the helium, the temperature within the alpha track rises considerably. If the alpha particle deposits 5.3 MeV in a volume of $8\times10^{-13}\text{cm}^3$ (for a track of radius 30 nm and length .025 cm), then the temperature should rise to about 2 K. At this temperature, D_T should be about $4\times10^{-4}\text{cm}^2\text{s}^{-1}$[79]. Then $t_d = r_0^2/4D_T = 25$ ns. The annihilation time $t_{tt} = 1/(\chi_{tt}c_T(0))$ will be much longer, about 125 ns, as χ_{tt} is $2\times10^{-10}\text{cm}^3\text{s}^{-1}$ at a temperature of 2.0 K (as measured in electron-bombarded superfluid helium[40]), and the concentration c_T should be about 4×10^{16} (for 30,000 metastables in the track). At later times, the ratio t_d/t_{tt} should decrease further, as D_T will increase somewhat as the temperature within the track drops. If we take the limit $t_{tt} >> t_d$ and $t >> t_d$, the expression for the afterpulsing rate simplifies to

$$I'(t) = \frac{k_f k_{tt}\tau_s N_T(0)}{2\chi_{tt}t_{tt}} \frac{t_d}{t}.$$

Because the alpha particle sets the temperature of the helium within the track, the qualitative time dependence of the afterpulsing has little dependence on the temperature of the helium bath. However the intensity of the afterpulsing decreases with temperature as it is lowered from 1.0 K to 0.5 K (see Figure 4.3). This can be explained by a lower density of metastable molecules at lower temperatures, which can in turn be attributed to a more rapid radial spreading of the ionization track immediately following the initial event. Roberts and Hereford have shown that the temperature dependance of the prompt pulse size from alphas in liquid helium can be explained by this hypothesis; they observe this effect as the temperature is dropped from 1.2 to 0.6 K[77]. The similarity of this temperature range to the temperature range in which the afterpulsing varies in intensity indicates that the two phenomena are closely linked, and indeed may be identical. The fact that the afterpulsing does not continue to decrease as the temperature is lowered below 0.5 K must then indicate that the expansion of the track below 0.5 K is not inhibited by scattering from excitations in the surrounding liquid helium, but instead is limiting by scattering among its own constituents.

Metastable-stable interactions

A second explanation for the afterpulsing is metastable destruction from scattering with some other, more stable species. This more stable species would probably be helium ions or electrons, as there are no other candidates that would last for the long times required. This explanation is favored by Roberts and Hereford in their model for alpha particle prompt scintillation; they claim that the temperature dependence they observe is not fit well by metastable-metastable annihilation[77]. However, Roberts and Hereford assume that the metastable annihilation contribution to the prompt

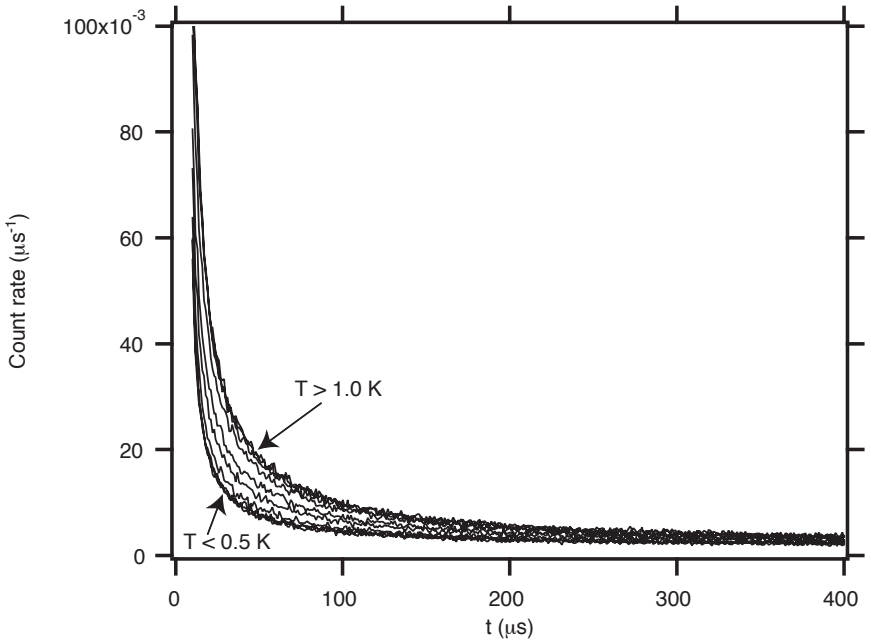

Figure 4.3: Afterpulse intensity as a function of time. The curves shown correspond to different helium bath temperatures (220, 360, 500, 670, 780, 830, 880, 960, 1060, and 1140 mK). The intensity of the afterpulsing increases as the temperature is raised from 500 to 960 mK. There is an average of 89 photoelectrons in the main pulse.

pulse is completely suppressed at the lowest temperatures, and the fact that a $1/t$ afterpulsing curve remains, albeit with lower amplitude, calls this assumption into question. It is also not clear why the temperature dependence would be much different in the two models if the metastable density dependence is primarily determined by diffusion, not annihilation. Also, it seems highly unlikely that many electrons escape quick recombination; it is estimated that the average recombination time is 0.3 ns[70]. In the Onsager theory, the probability of an electron-ion pair losing each other is proportional to e^{-r/r_0}, where $r_0 = \epsilon e^2/kT$, where ϵ is the dielectric constant. Therefore r_0 increases greatly at lower temperatures, and it is quite unlikely for an electron and ion in liquid helium to escape prompt recombination.

Ion-electron recombination

The third explanation for the afterpulsing is ion-electron recombination. In this model a fraction of the electrons and ions released as a result of the alpha particle do not recombine immediately, but escape to a large enough distance from each other that they are not attracted significantly by each other's field. Instead, they find each other on microsecond time scales, recombining to form singlet molecules that immediately decay. Again, a $1/t$ dependence is possible if diffusion is the dominant process determining the density of the interacting species. If, on the other hand, recombination dominates over diffusion, then the reaction should proceed as $1/t^2$. This can be explained by the density of electrons and ions each varying as $1/t$, which is the solution to $n_{\pm} = -\alpha n_{+} n_{-}$. Experiments measuring scintillation in liquid xenon do see an afterpulsing tail attributable to recombination, and it decays as $1/t^2$. In similar experiments in liquid krypton and liquid argon, a recombination tail is not seen; this is attributable to a recombination cross-section that increases for the lighter noble gases, and the lower temperatures of their liquids[80]. In the xenon experiments, the tail could be eliminated through the application of an electric field[80]. Similarly, this explanation for the afterpulsing in liquid helium could be tested by application of an electric field. Again, it seems unlikely that many electrons escape recombination, because of the low temperature of the helium and small average distance between electron and parent ion.

Thus it would seem that either metastable-metastable destruction, metastable-stable destruction, ion-electron recombination, or some combination of the three could be the source of the $1/t$ afterpulsing component. Each of these solutions assumes that the species responsible for the afterpulsing diffuses outward from the ionization track. It is the judgement of this author that metastable-metastable interactions

are the most plausible scenario, as electron-ion recombination in liquid helium is known to be quite efficient and because recombination should be enhanced at liquid helium temperatures. On the other hand, helium is unique among the noble gases for the extremely long lifetime of its $He_2^*(a^3\Sigma_u^+)$ molecule, and the fact that liquid helium is also unique in its exhibition of a $1/t$ afterpulsing tail probably reflects this attribute. Further discrimination between these possible solutions might be achieved by application of an electric field to the excitation region.

4.3 Helium Phosphorescence

The metastable helium molecular state $He_2^*(a^3\Sigma_u^+)$ is unique for its long lifetime in liquid helium, and the interactions and decay of this molecule are the most likely sources for the slowly decaying components observed following helium ionization. According to the theory of Hickman, Streets, and Lane[81], $He_2^*(a^3\Sigma_u^+)$ exists in liquid helium within a bubble of diameter ≈ 1 nm. Helium atoms near the bubble encounter a strong repulsion, produced by the outlying electron of the molecular state. The molecules in liquid helium have similar spectroscopic characteristics to those in vacuum, with spectral lines which are somewhat shifted. The metastable $He_2^*(a^3\Sigma_u^+)$ molecule can be de-excited by radiative decay, reactions with other helium metastables, and collisions with the container walls. Movement of the molecule through the liquid is limited by diffusive scattering with rotons, phonons, and ^{3}He impurities[82]. The density of phonons and rotons within the liquid depends strongly on temperature. This causes the molecular diffusion constant (D) to also change markedly.

The radiative decay of $He_2^*(a^3\Sigma_u^+)$ in vacuum is suppressed for several reasons. Radiative decay to the ground state (two free helium atoms) is forbidden, since transitions from triplet excited states to the singlet ground state involve a spin flip. Also,

the ≈ 2 eV deep triplet molecular potential is minimum at an internuclear distance of about 0.1 nm. At this distance, two ground state helium atoms repel each other strongly, giving a correspondingly small Franck-Condon factor. The radiative lifetime of the $\nu = 0$ level of the $He_2^*(a^3\Sigma_u^+)$ state in vacuum has been calculated[83, 38] to be 18 s. When the molecule decays radiatively, emission can be expected to occur in a continuum peaked in the extreme ultraviolet, similar to the Hopfield continuum.

Nonradiative de-excitations of this molecule in liquid helium that is free of metastable He are relatively rare. This stands in contrast to metastable triplet *atomic* helium (radiative lifetime $\tau \sim 8000$ s), which has been shown to survive only 15 μs in the liquid for temperatures in the range 1.4 to 2.2 K[39, 42]. After a few milliseconds, the only electronic helium excitations left are molecules in the $He_2^*(a^3\Sigma_u^+)$ state. As a result, these molecules are the dominant long-lived electronic excitations in liquid helium.

Despite the intrinsic interest of the highly forbidden $He_2^*(a^3\Sigma_u^+)$ decay, the radiative decay of molecular triplet helium has never before been continuously observed in the liquid. This is because the high concentration of helium molecules needed to perform spectroscopy results in a high rate of bimolecular recombination through exchange-dipole Penning ionization:

$$He_2^*(a^3\Sigma_u^+) + He_2^*(a^3\Sigma_u^+) \begin{array}{l} \nearrow 3He(1^1S) + He^+ + e^- \\ \searrow 2He(1^1S) + He_2^+ + e^- \end{array}. \tag{4.1}$$

If a high density of molecules n_0 is created in the liquid and allowed to decay through this two body reaction, the density of helium molecules, n, will at first vary as

$$1/n = 1/n_0 + \alpha(T)t \tag{4.2}$$

where α is the bilinear reaction coefficient. Experimental studies[39, 40] indicate that $\alpha(T)$ varies inversely with the number density of rotons, or as $e^{\Delta/T}$, where $\Delta \sim$

8.6 K. With α on the order of $10^{-10}\,\mathrm{cm}^3\,\mathrm{s}^{-1}$, triplet molecule decay in liquid helium is dominated by this diffusion limited process for $n \geq 10^9\,\mathrm{cm}^{-3}$. Cryogenic experiments using infrared spectroscopy to monitor the molecular state populations in the liquid (these experiments require relatively high molecule densities for detection) have so far been unable to observe the molecules for longer than 100 ms [40, 50]. In solid helium, however, where diffusion of molecules is much slower, the lifetime of the $He_2^*(a^3\Sigma_u^+)$ state has successfully been measured[49] using infra-red spectroscopy to be ≈ 15 s.

While developing detectors for the decays of trapped neutrons, we found that a significant portion of scintillations in the liquid helium occured on a time scale comparable to the theoretically predicted molecular triplet lifetime. Our explanation for the observed slow phosphorescence is that the high sensitivity of these detection systems has allowed us to observe molecular decay in a density regime which is dominated by radiative decay rather than Penning ionization.

We have observed these scintillations in liquid helium using an apparatus that employs a beta source. The effect has also been confirmed by measurements with a second apparatus that uses ^{3}He neutron capture to create scintillations[69]. Both experiments have in common the creation of $He_2^*(a^3\Sigma_u^+)$ molecules with ionizing radiation and the frequency downconversion of the resulting EUV light to blue light at about 440 nm using tetraphenyl butadiene (TPB), an efficient frequency downconverter of EUV radiation.

A diagram of the fiber-based apparatus is shown in Figure 3.7. Briefly, beta particles from a radioactive source cause scintillations within the liquid helium. This EUV light impinges on the sides of the cell, which are coated with tetraphenyl butadiene (TPB). The emitted blue light is reflected within the cell until it is absorbed by wavelength shifting fiber. A portion of the green light is then trapped in the fiber

and travels out of the cell to be detected via a photomultiplier tube. This apparatus is described in more detail in Chapter 3.

At the beginning of each run, the source is placed in the middle of the cell. The source is then mechanically removed from the detection region and the decay of counts is recorded. A sample spectrum, with a constant 42 s^{-1} background level subtracted, is shown in Figure 4.4. This measurement was performed at a temperature of 1.8 K and resulted in a measured decay lifetime τ of 13 $\pm$ 2 s. The measured decay is not purely exponential; this will be discussed below. Note that the drop in intensity immediately after the source is lowered gives an estimate of the fraction of light emitted by prompt fluorescence; since the signal drops immediately by a factor of 3, the singlet:triplet ratio must be roughly 2:1 (This assumes that the beta source gives little scintillation resulting from Penning ionization of triplet molecules, see Section 4.2.)

We checked that this slowly decaying signal originates from processes within the helium by performing runs in which blue light (from an LED) or ultraviolet light (from a UV lamp) were shone into a liquid helium filled cell. Turning off the light resulted in a sharp drop in PMT counts; the signal dropped to a constant background level within our timing bin size of 100 ms.

The roton collision-limited diffusion coefficient[82] for the triplet helium molecules in liquid helium is about $3 \times 10^{-4}\,cm^2\,s^{-1}$ at a temperature of 1.8 K. As a result, the molecules travel less than 1 mm before decaying, and are unlikely to hit the walls of the cell. Molecules could however hit the stainless steel rod which holds the beta source used in one of the experiments, producing a decay curve which is not a pure exponential.

A possible explanation for the non-exponential behavior at early times is extremely

slow vibrational relaxation of the triplet molecules. Since the calculated radiative lifetime of the molecule in vacuum decreases with increasing vibrational quantum number[83], a significant population of vibrationally excited molecules surviving to long times would clearly contribute to non-exponential decay. Vibrational relaxation of the molecules has already been found to be very slow in the liquid; Eltsov *et al.*[84] measure a $\nu = 1$ to $\nu = 0$ vibrational relaxation time of 0.3 ± 0.2 s. Since our detection method cannot differentiate between molecules of different vibrational states, the measured phosphorescence lifetime can only be strictly interpreted as a lower limit on the lifetime of the longest lived molecular state in liquid helium.

The decay curves could also be rendered non-exponential by two-body recombination with other metastable helium molecules. In a given ionization track, the molecule density can be quite high relative to the surrounding helium, and the resulting Penning ionization could lead to singlet molecule formation. This could lead to non-exponential fluorescence timing curves, especially at short times or high liquid temperatures at which diffusion is slow.

It is not expected that *different* ionization tracks interfere significantly in these experiments, since the sources of radiation that we use are relatively weak. The distance between tracks is therefore large, and the molecular density in the overlap of two expanding tracks is too small to result in many bilinear reactions.

Radiative decay of the $He_2^*(a^3\Sigma_u^+)$ has been continuously monitored in a low density regime. Obviously, improved statistical precision in the measurement of the lifetime in liquid helium could be accomplished by using a more intense source of ionizing radiation. The metastable densities achieved in this experiment are much less than the densities produced by other techniques where Penning ionization dominates the decay process. A better understanding of how interaction between species in the

ionization track influences phosphorescence behavior is desirable.

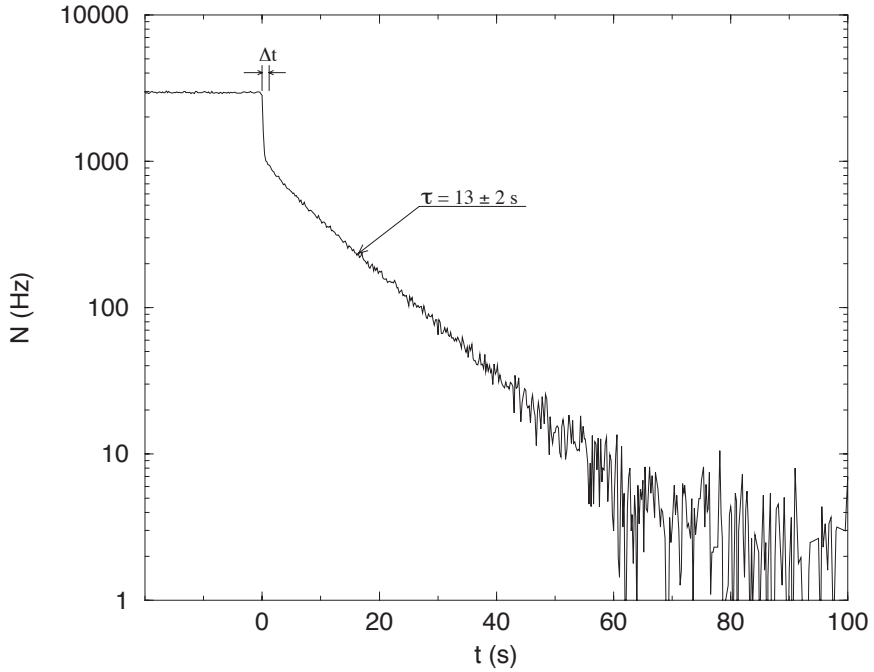

Figure 4.4: Count rate N of detected $He_2^*(a^3\Sigma_u^+)$ decays versus time. A ^{36}Cl β source is placed in the center of the detection region and then removed in a time $\Delta t < 1$ s. This measurement was performed at a temperature of 1.8 K and resulted in a measured decay lifetime τ of 13 $\pm$ 2 s.

4.4 Summary of Helium Scintillations

In summary, following an ionizing radiation event in liquid helium, the following processes occur:

- Ionizing radiation passing through liquid helium creates large numbers of excited atoms and molecules.
- The excited atoms and molecules are quickly quenched to their lowest energy singlet and triplet electronic states, yielding a population of $He_2(A\Sigma_u^1)$ and

$He_2^*(a^3\Sigma_u^+)$ molecules and $He(2^1S)$ and $He^*(2^3S)$ atoms.

- The singlet $He_2(A^1\Sigma_u^+)$ molecules radiatively decay within 20 ns of the original event, releasing an intense pulse of EUV light.

- The excited atoms $He(2^1S)$ and $He^*(2^3S)$ react with the ground state helium atoms of the liquid, forming vibrationally excited $He_2(A^1\Sigma_u^+)$ and $He_2^*(a^3\Sigma_u^+)$ molecules. The $He(2^1S)$ quenching reaction is apparently evident in the after-pulsing data, producing scintillation light on a 1.7 μs time scale.

- Triplet $He_2^*(a^3\Sigma_u^+)$ molecules diffuse out of the ionization track, reacting with each other via Penning ionization, forming some products that immediately decay, emitting more EUV light. This reaction appears to be especially evident when an α source is used, since the high excitation density in turn yields a high metastable density. The scintillation light created decays as 1/time.

- Triplet $He_2^*(a^3\Sigma_u^+)$ molecules that make it out of the track diffuse through the liquid helium. Eventually these molecules either radiatively decay or are quenched at the container walls. The lifetime of these molecules in liquid helium is 13 ± 2 s.

These processes are summarized in Figure 4.5.

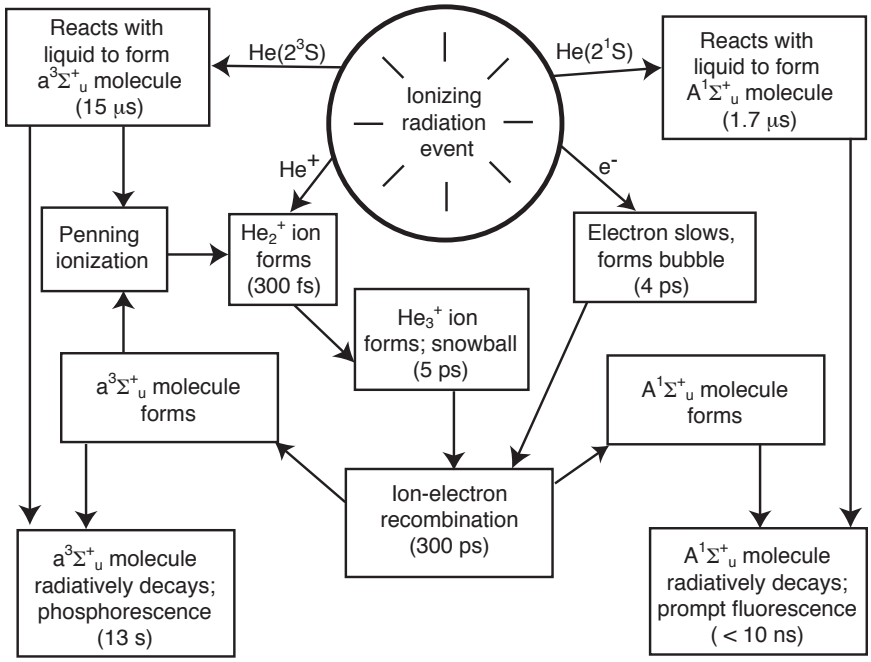

Figure 4.5: A summary of the processes and timescales following ionization in liquid helium.

Chapter 5

Experimental Apparatus

5.1 Overview

Magnetic trapping of neutrons requires a neutron beam, a magnetic trap, a bath of superfluid helium within the trap, and a scintillation detection system. This chapter describes the magnetic trapping apparatus in detail, as it was constructed in August, 2001. The neutron source is a monochromatic neutron beam at the NIST Center for Neutron Research (NCNR). We have designed and constructed a neutron monochromator, and placed it at the beam aperture of NG6, a cold neutron beam. The neutron beam created by the monochromator passes through the axis of a horizontally mounted magnetic trap and is absorbed by a transparent disc of boron oxide. Suspended along the axis of the magnetic trap is a copper-nickel tube, containing the bath of superfluid helium and the detector insert. Ultracold neutrons created in the superfluid helium decay and cause the helium to scintillate. Light created in the detector insert passes through the boron oxide beam dump and into light guides that transmit the light to room temperature, where it is detected by photomultiplier tubes. The photomultiplier signals are digitized and analyzed off-line.

Major improvements to the apparatus since 1999 are: a deeper, larger, demountable magnetic trap, an improved detection system using a transparent beam dump, a superfluid heat link, and a 9 Å monochromator.

5.2 The Neutron Beam

The neutron trapping experiment is located at the end station of the NG6 beamline at the NCNR. The NCNR houses a 20 MW research nuclear reactor, creating neutrons from uranium fission. Neutrons are moderated with heavy water surrounding the core and a liquid hydrogen cold source placed near the reactor core. The cold source is a hollow shell filled with liquid hydrogen at 20 K. Neutrons created in the reactor core can partially thermalize with the liquid hydrogen, then exit through a hole in the sphere. Surrounding this exit hole are multiple neutron guides. One of them, NG6, is used by fundamental neutron experiments, including the neutron trapping experiment described in this thesis.

NG6 is a rectangular guide, 60 m long, 15 cm tall, and 6 cm wide. It is evacuated to minimize neutron absorption, and is coated on its inner surface with ^{58}Ni, which has an effective Fermi potential of 335 neV (see Section 1.3). This potential corresponds to a maximum perpendicular velocity of 8 m/s. Neutrons with a perpendicular velocity component less than this will be reflected by the nickel, passing down the full length of the guide tube to be emitted from the NG6 final aperture. The beam divergence depends on neutron wavelength, since longer wavelength neutrons are reflected from a wider range of angles than short wavelength neutrons. The ^{58}Ni coating is reflective up to a critical angle of 2 mrad/Å.

The layout of the NG6 beam station (as of August, 2001) is shown in Figure 5.1. Neutrons from the lower half of the guide pass through or are reflected by a 5 Å

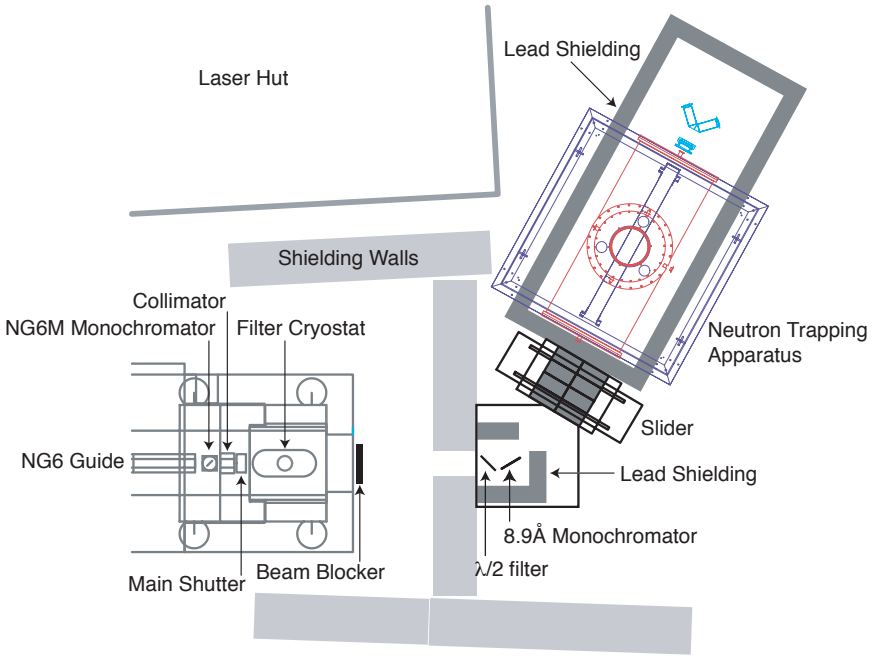

Figure 5.1: Arrangement of neutron beam, neutron filters, monochromator, and neutron trapping apparatus.

monochromator (NG6M); those that are not reflected are absorbed by a beam dump. The cold neutron beam from the top half of the guide passes through a filter cryostat, which contains two blocks each of bismuth and beryllium (each 7 cm wide, 7 cm tall, and 5 cm in length). The bismuth blocks absorb gamma rays from the neutron beam, while the beryllium reflects neutrons with wavelength less than 3.95 Å out of the beam. The filter cryostat is cooled to liquid nitrogen temperature to reduce phonon scattering of the cold neutrons. The end of NG6 is equipped with a manually controlled "shutter" which controls the flux of cold neutrons exiting the NG6 beam line. In addition, we have added a "blocker" over the end of the NG6 final aperture (a 6 cm diameter hole in a lithium glass plate). The blocker is computer controlled, and consists of lithium plastic covering an aluminum plate. It does not absorb gamma rays significantly, but absorbs the entire cold neutron beam.

The NG6 beam line is shielded with steel containers filled with polyethylene and steel shot. This mixture absorbs neutrons more effectively than pure steel or pure polyethylene. The high-Z steel shot is effective at scattering neutrons, thus reducing their energy and increasing the time they spend in the shield. The hydrogenous polyethylene is a more effective moderator for the neutrons and will eventually absorb them.

After exiting the NG6 defining aperture, the neutrons enter a lead hut containing a 9 Å neutron monochromator. This is a custom built apparatus designed to Bragg reflect neutrons with the correct wavelength to undergo superthermal scattering in liquid helium. The design of this instrument is described more completely in the thesis of Carlo Mattoni[25]. The monochromator reflects a 9 Å neutron beam toward the cryogenic trapping apparatus. It also reflects neutrons of half this wavelength, so an additional graphite monochromator tuned to $\lambda/2$ is placed in the neutron beam to filter out these unwanted neutrons. The neutron flux exiting the neutron monochromator assembly is $1 \times 10^7\,\mathrm{cm}^{-2}\,\mathrm{s}^{-1}$.

The final beam controlling device is the computer-controlled "slider", so named because it slides a stack of lead bricks in and out of the beamline. The front of the stack of bricks is covered with a layer of boron-doped plastic to absorb the neutron beam in the case the shutter and blocker are open with the slider closed.

5.3 Dewar and Cryogenics

The cryogenic apparatus is shaped like an upside-down "T", with the magnetic trap and detection insert held in the horizontal section and the dilution refrigerator held in the vertical section. The dilution refrigerator is connected to the helium bath through a superfluid helium-filled heat link. The apparatus is shown in Figure 5.2.

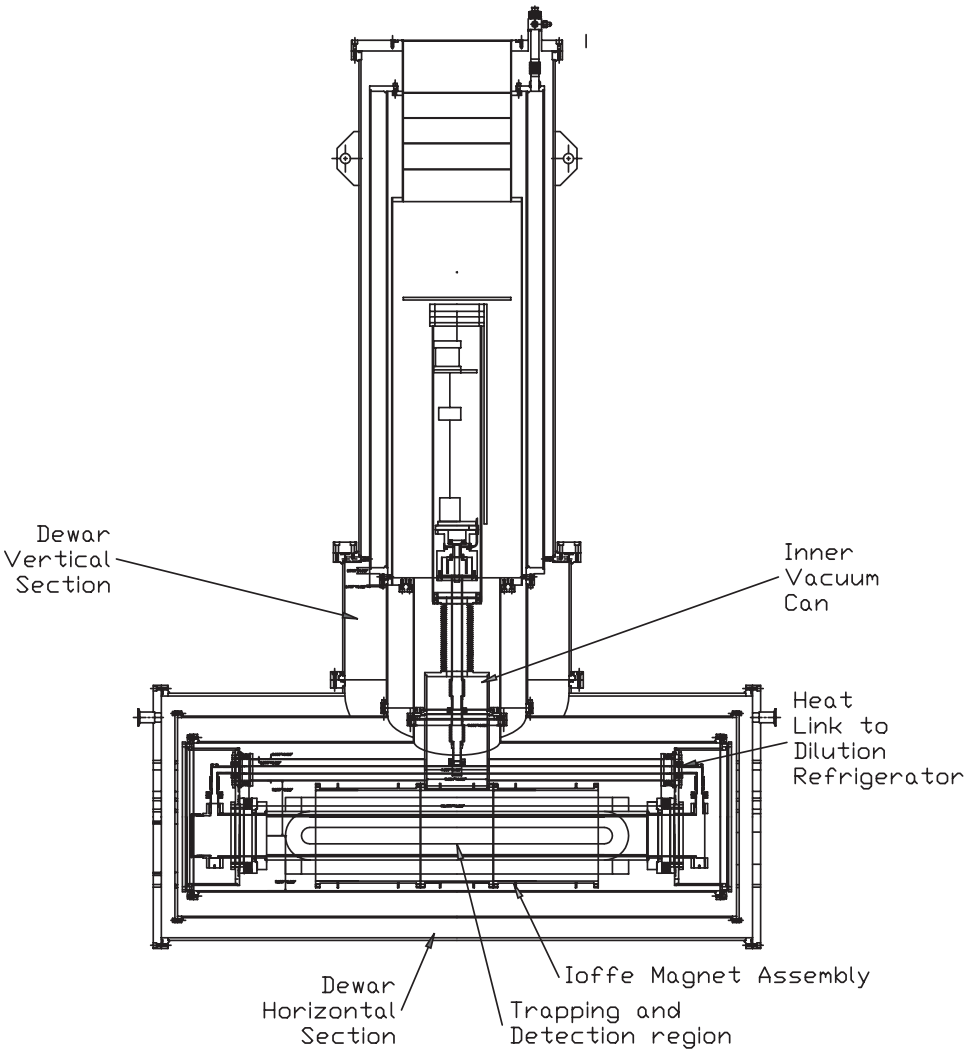

Figure 5.2: Diagram of the neutron trapping apparatus. The neutrons are trapped within a cell whose temperature could be lowered to 200 mK using a dilution refrigerator. Surrounding cryogenic layers at 4 K, 77 K, and 300 K provide thermal insulation.

Dewar

The Dewar is made of several cryogenic layers, at room temperature (300 K), liquid nitrogen temperature (77 K), and liquid helium temperature (4 K). The layers are separated by vacuum, with the space between 4 K and 77 K and between 77 K and 300 K evacuated using the same pump and connected through small holes in the 77

K shield. This space is known as the Outer Vacuum Chamber (OVC). Inside the 4 K shield, between the liquid helium bath and the dilution refrigerator, is the Inner Vacuum Chamber (IVC). The cryogenic layers are wrapped with aluminum-coated mylar (super-insulation) to cut down on infra-red radiation from warmer temperatures.

There are only a few minor changes to the cryogenic design since the writing of Clint Brome's Ph.D. thesis, and for a more detailed description of the Dewar, the reader is referred there[23]. In 2001 the IVC "T" section was modified to accomodate the new superfluid-filled heat link, and the IVC end cans were shortened to accomodate the new, larger magnetic trap within the helium bath.

Dilution Refrigerator

Suspended in the center of the vertical section is a dilution refrigerator. The coldest and lowest point on the dilution refrigerator is the mixing chamber, in which the phase boundary between a ^{3}He rich phase and a ^{3}He dilute phase is maintained. Cooling in a dilution refigerator is provided by pumping ^{3}He out of the ^{3}He dilute phase. The heat of mixing is then extracted from the system as ^{3}He diffuses from the ^{3}He rich phase to the ^{3}He dilute phase within the mixing chamber. A sketch of the dilution refrigerator is shown in Figure 5.3, and more details on the working of a dilution refrigerator can be found in reference[85]. The refrigerator is specified to have a minimum cooling power of 0.4 mW at 100 mK. In practice we do not reach this low temperature because of infrared heat loads on the cell. The lowest cell temperature measured with the detection cell and optics in place was 200 mK.

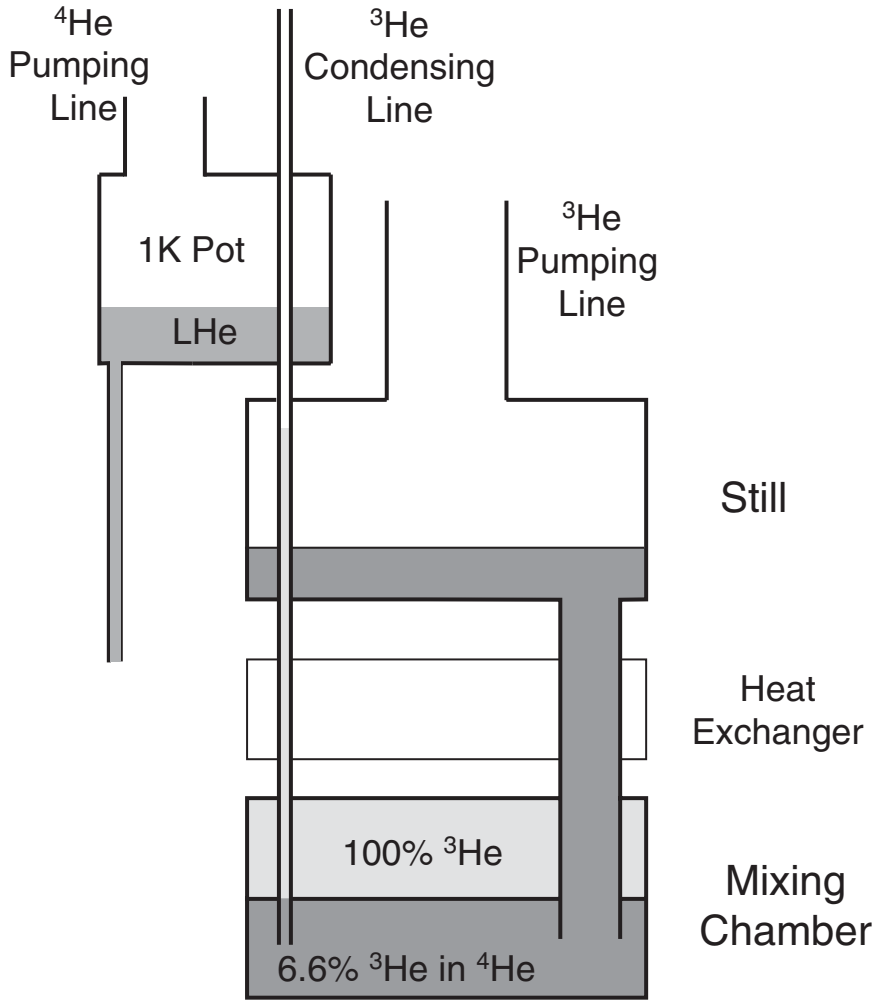

Figure 5.3: A sketch of a dilution refrigerator.

The Superfluid Heat Link

The "buffer cell" is a copper-walled cavity with several input lines for helium (see Figure 5.4) that is bolted to a copper "transition plate", which is in turn bolted to the bottom of the mixing chamber. Both the transition plate and buffer cell are plated with gold to ensure good thermal conductivity between the mixing chamber,

transition plate, and buffer cell[1]. Each of the fill lines is connected to the buffer cell with a small indium seal. Two of these lines are 1.6 mm diameter and pass through the condensing lines of the dilution refrigerator, are heat sunk to the 1 K pot, and are heat sunk at ever-warmer temperatures on their way up to room temperature. The third line is of larger diameter (6 mm) and is heat sunk to the 50 mK plate, still, and 1 K pot. This line is closed while condensing helium, and was added to allow us to pump out the detection cell. More details about the heat sinking of the fill lines can be found in reference [25].

Inside the buffer cell are two silver-sintered fins. These were added to decrease the Kapitza resistance between the copper buffer cell and the superfluid helium[2]. The sinter was bonded to the fins by enclosing the fins with the sinter in a small rig, squeezing the sinter to the fins with 2 MPa of pressure, then heating for 30 minutes at 120 degrees C. At the present operating temperature of the experiment, the Kapitza resistance turned out not to be significant.

The buffer cell houses a capacitance-based level gauge for measuring the level of liquid helium within it. This is critical for determining the helium level in the cell. It is constructed from two stainless steel tubes, one inside the other. Depending on the amount of helium between the tubes, the capacitance of the tube system varies because the dielectric constant of liquid helium is different from that of gaseous helium. The helium level meter is described more completely in reference [25].

A 2.5 cm diameter seamless cupro-nickel tube full of superfluid helium leads out

[1]Gold plating performed by Epner Technology, Brooklyn, NY (718) 782-8722, (www.lasergold.com)

[2]Silver sinter is 99.99% purity, 3 μm diameter, purchased from Leico Industries, Inc., New York, NY.

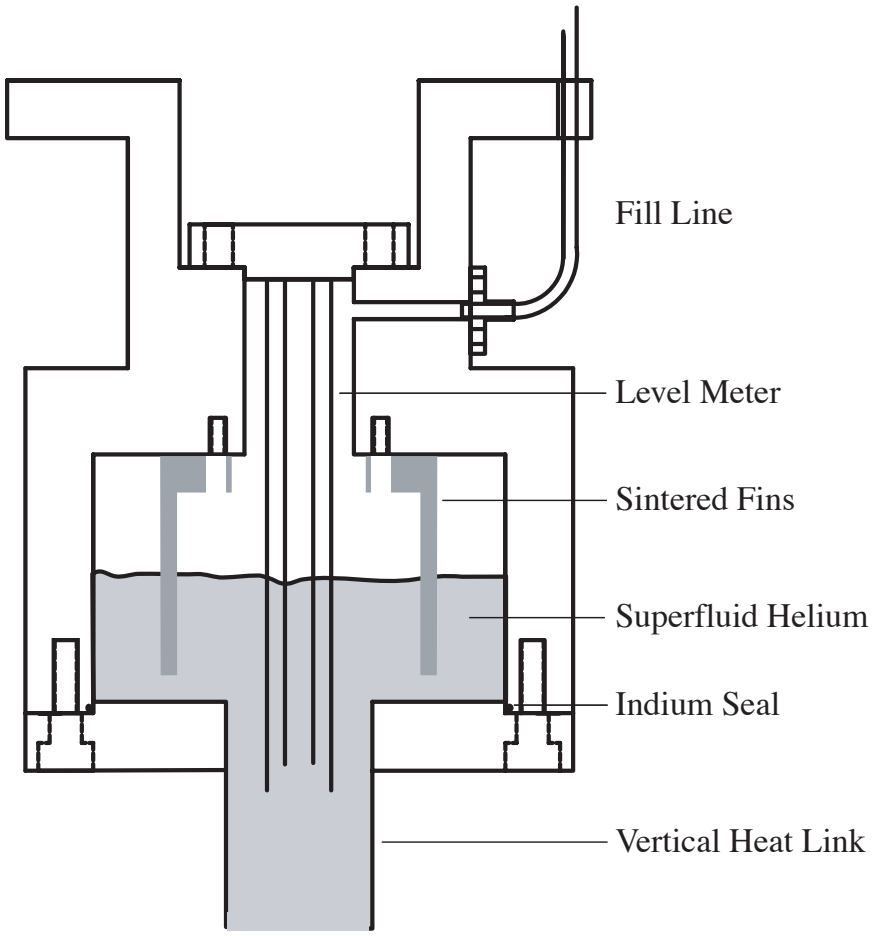

Figure 5.4: A sketch of the buffer cell.

of the bottom of the buffer cell[3]. This is the beginning of the "heak link" that leads to the trapping cell. Mechanical flexibility in the heat link is provided by several beryllium-copper molded bellows: one in the vertical section and one at each end of the trapping cell[4]. Each end of each beryllium-copper bellows is brazed to a section

[3]Copper-nickel tube purchased from Clayton Steel Supply, Kirkwood, MO (800) 760-4944 (www.claytonsteel.com)

[4]Beryllium-copper bellows (BC-1000-40-12M and BC-500-42-14) purchased from Mini-Flex Corporation, Ventura, CA, (805) 644-1474 (www93.thomasregister.com/olc/mini-flex/).

of copper-nickel tubing, which is in turn brazed to a flange. The various sections of the heat link are attached together by indium seals. A drawing of the heat link is shown in Figure 5.5.

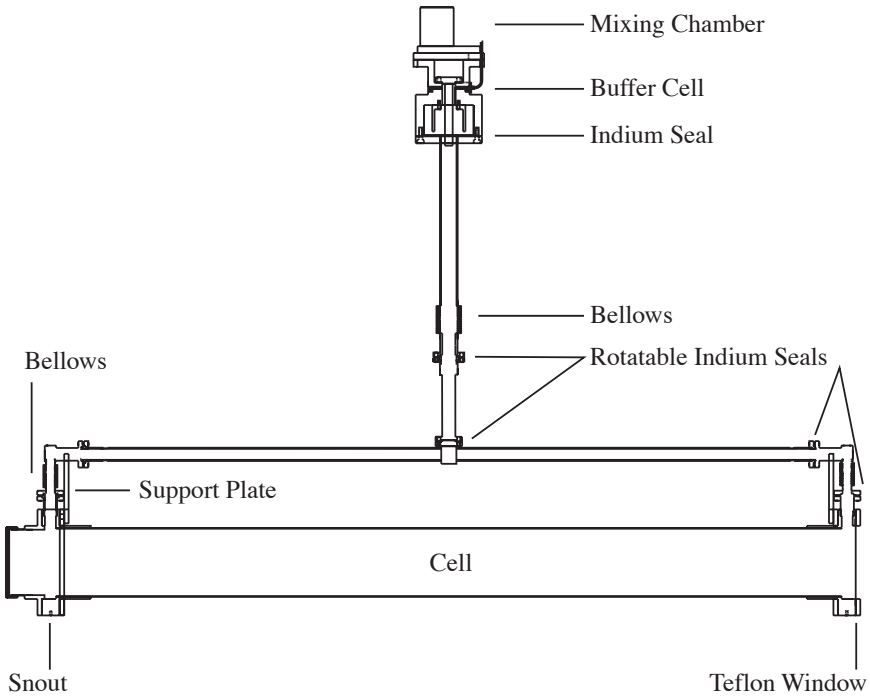

Figure 5.5: Diagram of the superfluid heat link

Use of a superfluid heat link constitutes a substantial improvement over the previous apparatus. The previous heat link was made of copper, with a mechanical flexibility provided by copper braids at the T-section. The copper heat link had a measured thermal conductance of $2.3 \times 10^{-4}\,\mathrm{W\,K^{-1}}$ [23]. Because a large copper heat link would suffer from high eddy currents when we ramped our new magnet, and because we wished to cool the cell to a lower temperature, we designed the new apparatus with a superfluid heat link. This design also eliminated the need for separate helium fill lines going down to the trapping cell.

To calculate the thermal conductivity of the heat link, we assumed that the trans-

Table 5.1: Mixing chamber temperature, cell temperature, and estimated heat link conductance as a function of heat load.

$\dot{Q}_R[\mu W]$	$T_{MC}[mK]$	T_{Cell} [mK]	K [W/K]
0	179	258	0.47×10^{-2}
102	197	273	0.62×10^{-2}
213	212	286	0.78×10^{-2}
398	233	302	1.03×10^{-2}
771	275	342	1.69×10^{-2}
1515	350	408	3.49×10^{-2}

port of phonons through the helium is ballistic, but that the phonons scatter diffusely from the tube walls. In this limit the conductivity can be expressed as

$$K = 16\frac{W}{K}(\frac{d}{\mathrm{cm}})^3(\frac{L}{\mathrm{cm}}^{-1})(\frac{T}{\mathrm{K}})^3)$$

where d is the diameter of the tube and T is the helium temperature. The combination of tube diameters and lengths in the constructed heat link gives a calculated conductance of $1.03\frac{W}{K}(\frac{T}{K})^3)$.

The heat link was tested by condensing liquid helium into the cell and measuring the chamber temperature and cell temperature over a range of heat loads. Heat was applied using a resistor on the cell. The tests are summarized in Table 5.1 below, where $\dot{Q}_R$ is the power applied by a resistor attached to one end of the cell and T_{MC} and T_{Cell} are the temperatures of the cell and mixing chamber respectively.

The conductance is estimated by fitting the cell temperature to

$$T_{cell} = \frac{\dot{Q}_R + \dot{Q}_0}{KT_{MC}^3} + T_{MC},$$

where the approximation is assumed that the conductance is set by the mixing tem-

perature temperature. Here K and $\dot{Q}_0$ are free parameters. The measured mixing chamber and cell temperatures and best fit are shown below in Figure 5.6. The best fit implies a conductance K of $0.81 \pm 0.04 \frac{W}{K}(\frac{T}{K})^3)$, with an intrinsic heat load $\dot{Q}_0$ of 360 μW. This matches the calculated conductance $(1.03 \frac{W}{K}(\frac{T}{K})^3))$ to within 20%.

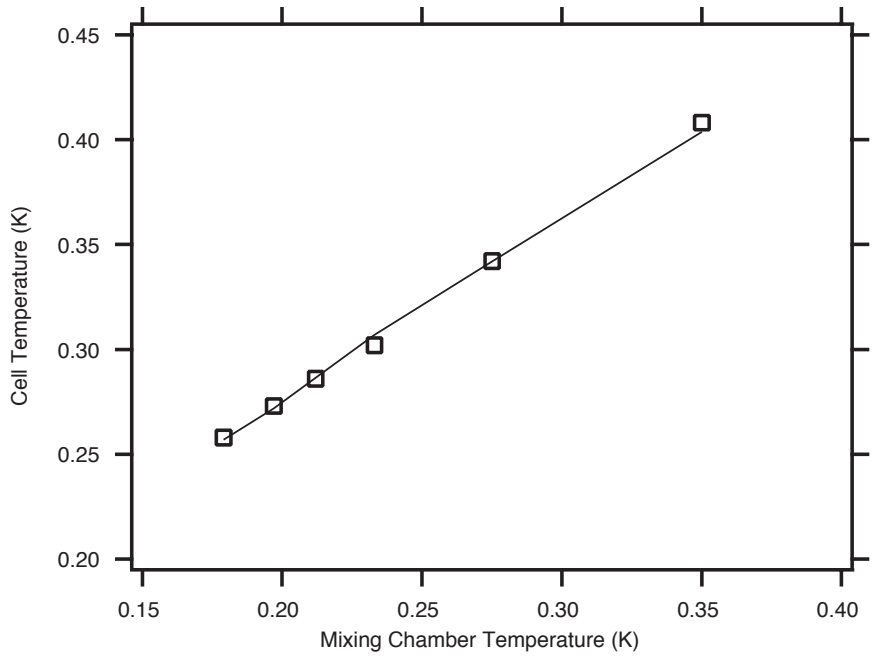

Figure 5.6: Conductivity of the superfluid heat link.

By cooling the mixing chamber, gaseous helium introduced through the fill lines gradually liquifies within the buffer cell and drips down into the experimental cell. The cell can be filled and cooled to base temperature within 18 hours after condensing is begun. While cooling, good thermal contact is maintained between the cell and the mixing chamber, even when the helium is above the λ point. This can be attributed to convection, since the superfluid is more dense than the normal fluid and cooling is performed at the top of the system. However, if the mixing chamber is warmed while the cell is full, it is possible for there to be a large thermal mismatch between the cell and the mixing chamber, with warm (> 4 K) normal fluid floating above the

superfluid.

The Cell

The experimental cell is a copper-nickel tube suspended along the axis of the magnetic trap. Copper-nickel[5] was chosen because it satisfies the requirements of low electrical conductivity and soldering capability, and is not ferromagnetic. Most other materials do not satisfy these requirements; for example, titanium, aluminum, and stainless steel cannot be soldered, while copper has high electrical conductivity. Soldered to each end of the experimental cell is a copper-nickel "endcap". The two endcaps are brazed to the two ends of the superfluid heat link, and have bolt circles to allow the two ends of the cell to be sealed. The end of the cell where the beam enters (side A) is closed with a teflon window seal[86]. The end of the cell where the scintillation light exits is sealed with a indium seal to the "snout".

The snout (see Figure 5.7) is a superfluid-tight acrylic window, sealed to a copper-nickel flange with Stycast epoxy [6]. The design of the snout incorporates a thin metal fin extending from the copper-nickel flange. The transparent acrylic window is made of two parts: a short acrylic tube and a round plate. The plate is glued into the end of the tube, and the tube is in turn glued onto the metal fin. This design allows for the thermal contraction of the acrylic window; as the apparatus is cooled and the window shrinks, the metal fin bends but does not break. The snout fin is machined with a sample of the acrylic tube as a guide to the final outer diameter of the fin; the fin is approximately 250 μm thick and is machined so that the tube fits over the fin with a clearance of < 25 μm. This design allows a superfluid-tight window seal, and

[5]70 % copper, 30 % nickel, purchased from Clayton Steel Supply

[6]Stycast 1266, made by Emerson & Cumming, http://www.emersoncumming.com

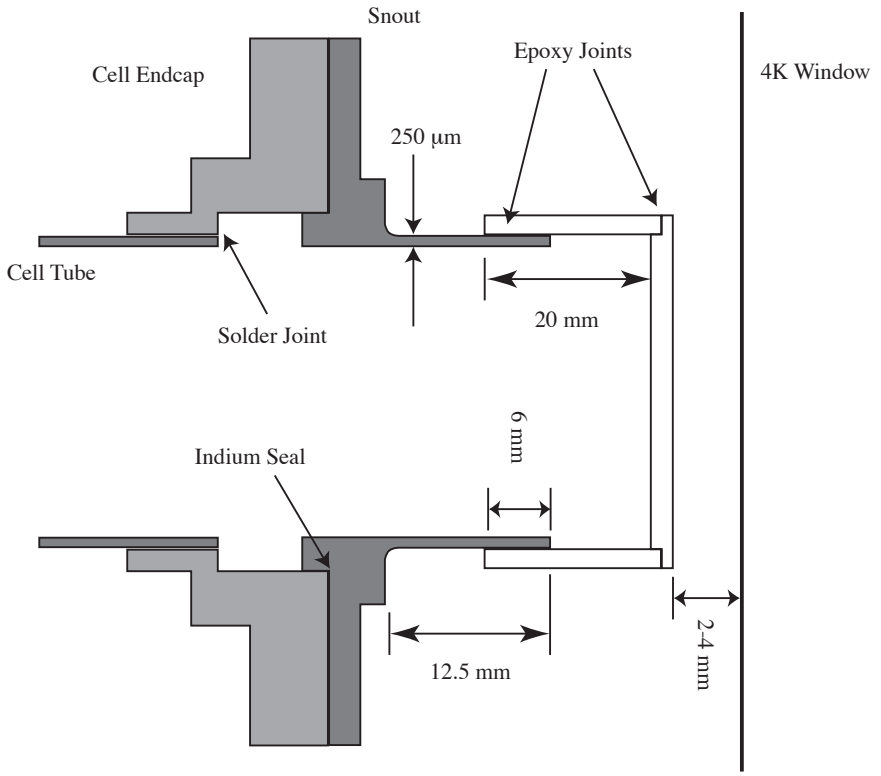

Figure 5.7: Design of the snout

has proved remarkably leak-free from cool-down to cool-down.

The cell is held in place using Kevlar yarn that wraps around the cell tube and is held from the IVC (see Figure 5.8). Kevlar is used for this purpose because of its combination of low thermal conductivity and high tensile strenth. The yarn is made of 4 twisted threads, each with a diameter of 400 μm. Its thermal conductivity is $3 \times 10^{-4}\,\mathrm{W\,cm^{-2}\,K^{-1}}$. The yarn is wrapped around the cell and attached to two "cell positioning devices". The cell positioning devices mount to the IVC and can pull the cell up and down without twisting the Kevlar (see reference [23] for more details). The cell is prevented from moving in the z direction by additional Kevlar strings (one at each end of the dewar) connecting the cell to the IVC. The distance between the cell and the 4 K window is set to be 2 mm. The thermal load on the cell through the

Kevlar from 4 K is estimated to be 15 μW.

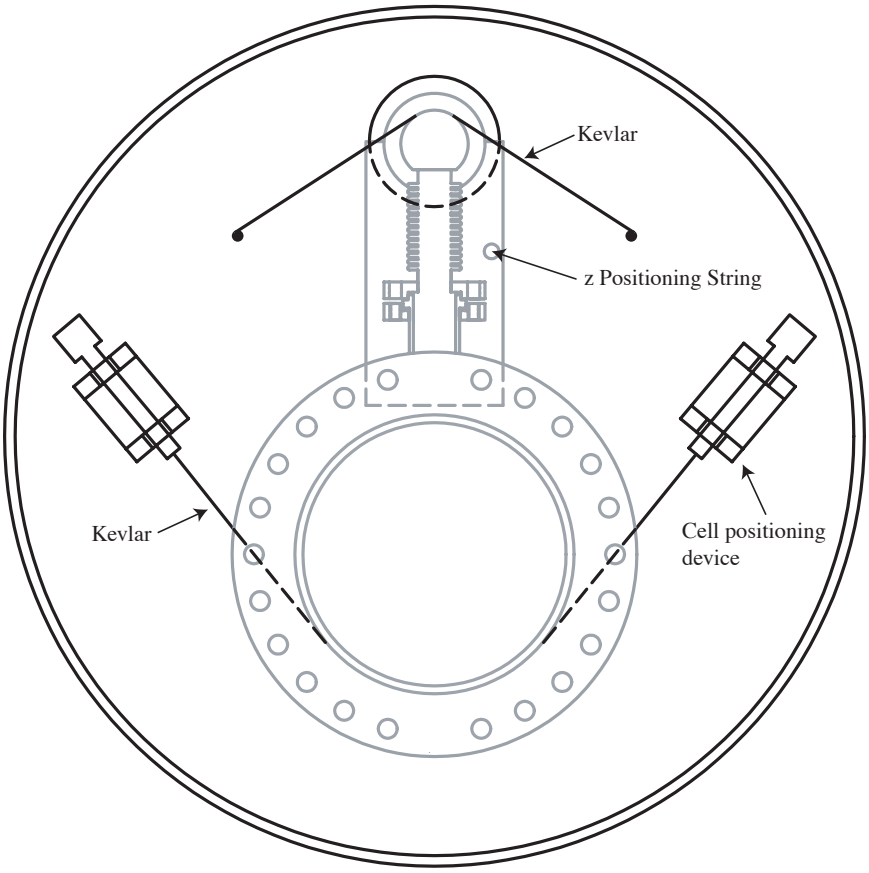

Figure 5.8: View of the IVC showing the cell positioning system.

Inside the copper-nickel tube is a thin tube of boron nitride, and inside of that is a thin tube of graphite. The boron nitride and graphite tubes are constructed in short lengths and are keyed to fit together without gaps. The boron nitride is essential for shielding the copper-nickel tube from scattered neutrons, and the graphite tubes absorb any neutron-induced luminescence emitted by the boron nitride (see reference [25]).

Boron nitride is also used as a shielding material at 4 K, 77 K, and 300 K on the neutron beam (A) side of the apparatus. The design of this shielding, as well as the

vacuum seals and black-body radiation issues pertaining to the A-side windows, are fully discussed in reference [25].

5.4 The Detection Insert

This section describes the design and calibration of the detection insert used to count trapped neutrons in August, 2001. The detection insert is based on tetraphenyl butadiene (TPB) evaporated on a Gore-tex sheet, rolled up into a tube and slid into the trapping region.

The development of helium scintillation detectors for this experiment is described in full detail in Chapter 3 of this thesis, and the physical mechanism of the scintillation is described in Chapers 2 and 4. The great majority ($> 80\%$) of the scintillation light from singlet decay is emitted within 20 ns of the ionization event. Each neutron decay event creates a bright flash of EUV light, which is converted to a pulse of blue light by the wavelength shifter. This visible light is transported to room temperature through windows and light guides, and is detected by photomultipliers at room temperature. In this way, neutron decays events result in bursts of photoelectrons, which are detected and recorded electronically.

A sketch of the detection insert and associated optics is shown in Figure 5.9. The detection insert is located in the center of the trapping region and surrounds the region where neutrons beta-decay. It is made from two sheets of TPB coated Gore-tex rolled into tubes and placed end-to-end[7], making a tube that is 35 cm long and 8.4 cm in diameter. Each sheet is first cut to a rectangle 17.5 cm x 28 cm in area. The sheets are then placed in an organic evaporation rig and coated with TPB as

[7]Unembossed GoreTex GR gasket material, Gore Corporation (www.gorefabrics.com).

described in Chapter 3. Each sheet required 4 evaporations to achieve a high enough TPB density, measured by concurrently evaporating TPB onto 2.5 cm x 6.3 cm glass slides placed in the evaporation rig along with the Gore-tex. The density of TPB on the Gore-tex is not uniform and is estimated to be between 200 and 400 $\mu g\,cm^{-2}$. The TPB absorbs EUV light and fluoresces in the blue, with a peak wavelength of 440 nm. Blue photons, after being emitted by the TPB, on average reflect several times from the TPB coated Gore-tex before escaping out through one of the two tube ends. Some of the light is absorbed by the TPB coating, which is not a perfect reflector. The reflectivity and specularity of TPB-coated Gore-Tex has not been measured, and thus it is difficult to estimate the fraction of blue light emitted by the TPB that finally escapes the Gore-Tex tube.

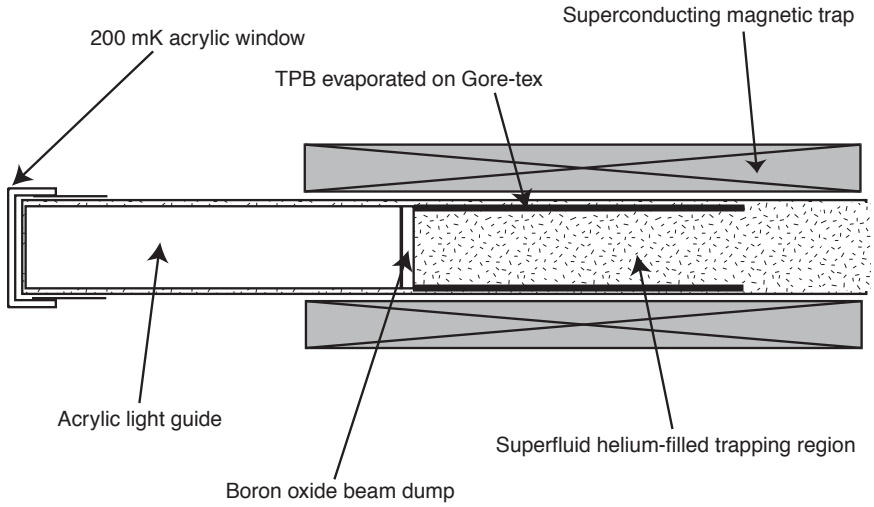

Figure 5.9: The neutron detection cell

In order for the TPB luminescence to be collected by light guides and transported to room temperature, it must pass through an optically transparent, neutron-absorbing disc of boron oxide located directly after the trapping region. Considerable effort went into developing a neutron beam dump that was both transparent and free

of elements that would activate under neutron irradiation. This was desirable because a transparent beam dump would allow most of the scintillation light through, greatly improving the detection efficiency of trapped neutron decay events. The three materials that we considered for transparent beam dumps were lithium fluoride (LiF), pure boron oxide (B_2O_3), and a glass fashioned from a melt of B_2O_3, Li_2CO_3, and ZrO_2.

Lithium fluoride was initially the most promising of these materials; however it was found that LiF luminesces very brightly for a considerable time after being irradiated by neutrons[25]. No other material was found to luminesce as much as LiF; this is attributable to color center relaxation in the crystalline matrix.

The second approach was undertaken in collaboration with the group of Edgar Dutra Zanotto in Brazil. High purity powder samples of B_2O_3, Li_2CO_3, and ZrO_2 were used. After several attempts, a transparent glass (the "Brazilian glass") that was stable in atmosphere was produced by the Zanotto group. It consisted of 70% B_2O_3, 27% Li_2CO_3, and 3 % ZrO_2 by weight[8]. Each of these compounds was calculated to yield little activation (< 1 decay s^{-1}) after 30 minutes of neutron acivation. However, after exposing the Brazilian glass to the neutron beam and monitoring its gamma ray emission via a germanium counter, it was found that a high flux of 511 keV gamma rays was emitted. Then, by exposing the glass again to neutrons and placing it in contact with a piece of plastic scintillator, it was found that the activity decays with a half-life of 6480 $\pm$ 40 s (see Figure 5.10). This identified the activated species as ^{18}F, a β^+ emitter with a 6590 second half-life. It is believed that the combination of lithium and oxygen in the same material brought about the reaction $^{16}O(t, n)^{18}F$ following tritium emission by the lithium upon neutron capture. The unexpected,

[8]Chemicals purchased from Alfa Aesar (www.alfa.com)

intense positron emission from the Brazilian glass made it unusable for the neutron trapping experiment.

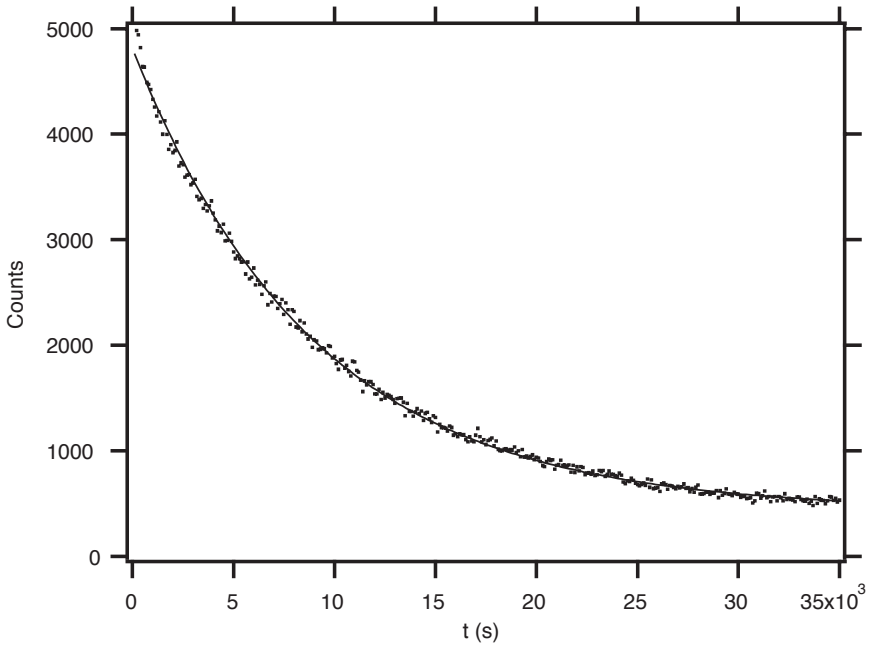

Figure 5.10: The positron emission decay curve of the Brazilian glass after 15 minute exposure to the neutron beam.

The final beam dump was fashioned from a disc of boron oxide, 99.9999% purity[9]. The difficulty with boron oxide is that it clouds up when exposed to atmosphere (it is hygroscopic). However, we found that by minimizing its exposure to the atmosphere, its transparency could be maintained within acceptable limits. It was polished at the NIST glass shop, then kept under vacuum until needed. We found that it could be kept in the atmosphere for up to 15 minutes before clouding significantly (see Figure 5.11). The boron oxide also lumineseces a bit when exposed to neutrons; this is believed to be the prime source of luminescence background in the experiment (see reference [25]).

[9]Boron oxide disc purchased from All-Chemie Ltd., Mt. Pleasant, SC (843-884-

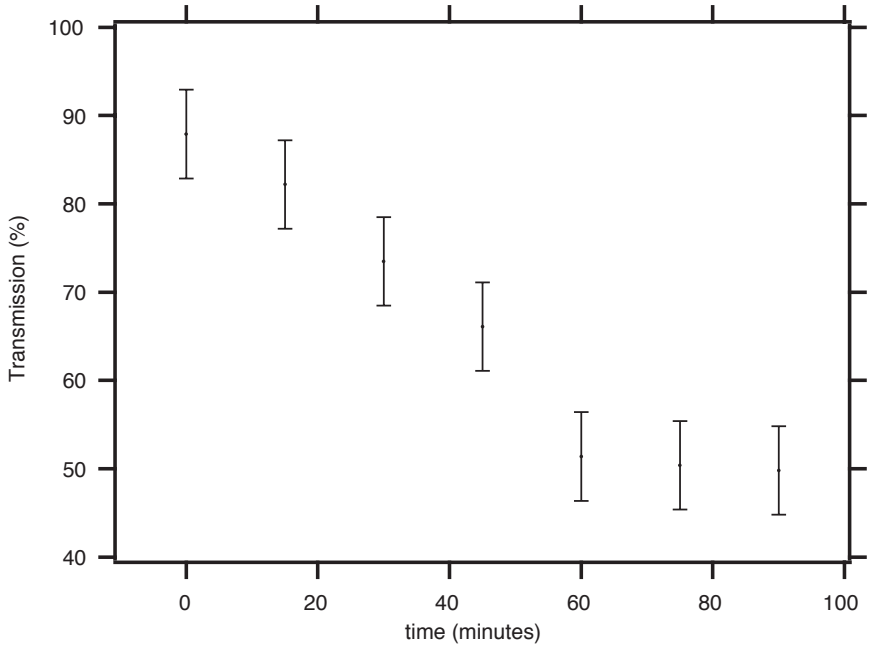

Figure 5.11: The transmission of boron oxide as a function of atmospheric exposure time. This measurement was performed by measured the transmitted light from an LED with a photodiode.

Following the beam dump is a UVT acrylic light guide of diameter 8.7 cm and length 40.7 cm that transports light from the Gore-Tex tube to the end of the experimental cell[10]. The beam dump is held to the light guide with FEP teflon tape[11]. The light guide is wrapped in a 175 μm thick layer of Tyvek, a paper that protects the light guide from scratches and fingerprints and increases its light transport efficiency[12]. The light guide slides inside the experimental cell, and is surrounded by tubes of graphite and boron nitride. Three stainless pegs radially extend from the light guide in the endcap region, and position the light guide within the cell. The

4400) (www.allchemie.thomasregister.com)

[10]UVT acrylic material purchased from Boedecker Plastics, Shiner, TX (www.boedeker.com). All light guides polished by Universal Plastics, Akron, OH

[11]McMaster-Carr, New Brunswick, NJ

[12]Tyvek is a paper made from filaments of polyethylene, made by DuPont.

pegs are 3 mm diameter, 10 mm long, and are recessed 5 mm deep into lightguide. The axial position of the pegs is chosen so that the end of the light guide ends up just inside the snout window.

The optics arrangement used to carry light to room temperature is shown in Figure 5.12. Scintillation light that passes out of the light guide and through the snout window must pass through acrylic and quartz windows at 4 K. The acrylic window makes an indium seal to a flange at 4 K, separates the IVC and OVC, and absorbs black-body infrared radiation from higher temperatures. Because the thermal conductivity of the acrylic window is poor, a thin (0.33 mm thick) sheet of quartz is epoxied to the outer surface of the acrylic window to prevent a hot spot from developing in the center of the acrylic window. This is critical in minimizing black-body radiation (see reference [25]). Unfortunately, the quartz cracked quite a bit as the experiment cooled down; this reduced light transmission.

After the 4 K window is a second light guide, this one of larger diameter (11.4 cm) than the first. This acrylic rod transports scintillation light from 77 K to 300 K, and is 35 cm long. The 77 K end of the light guide is heat sunk to the 77 K flange using strips of aluminum foil and has copper wires glued to its end face; this evens out the temeprature at the end of the light guide and thereby reduces the emission of blackbody radiation (see reference [25]). The wire pattern covers 11% of the face of the light guide and therefore reduces light transmission.

A vacuum seal is formed around the second light guide using a Viton O-ring seal. A metal clamp fastens tightly around the light guide and prevents it from being pulled into the OVC. The O-ring "UltraTorr" seal and clamp are described more completely in reference [23] and are sketched in Figure 5.13.

At room temperature, the optics are surrounded by aluminum cans that contain

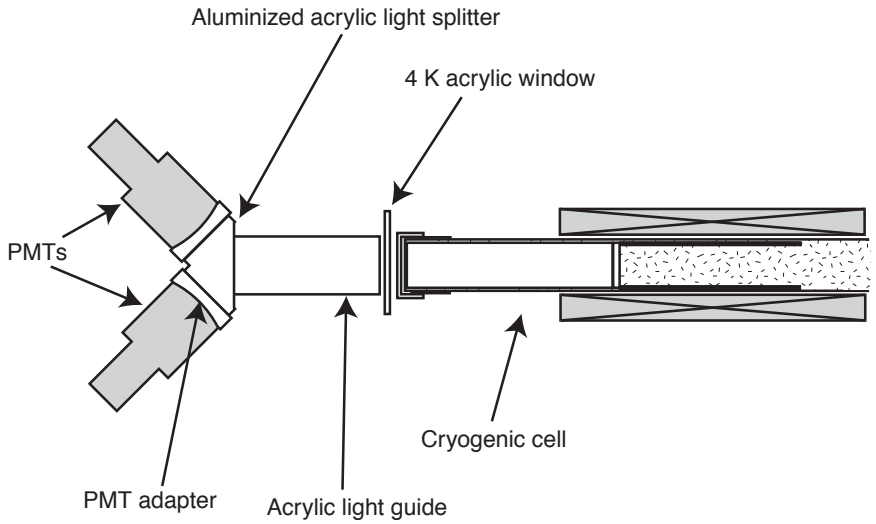

Figure 5.12: Light collection optics

the photomultiplier tubes. These cans are held together by O-ring seals and can maintain a positive pressure relative to the guide hall atmosphere. Dry nitrogen is flowed through the photomultipliers cans to flush out any helium; this precaution is taken to avoid helium poisoning of the photomultiplier tubes (which causes them to afterpulse). In normal operation, the scintillation light is split into two photomultipliers by a "light splitter", which is two light guides glued together at right angles and aluminized[13]. The scintillation light then enters the photocathode of the two photomultiplier tubes. The photomultipliers are coupled to the light guide splitter, and the light guide splitter coupled to the large light guide, by optical grease[14].

The scintillation light is split into two photomultiplier tubes to avoid backgrounds from dark counts and neutron-induced luminescence. Because time-dependent lu-

[13]Alumization performed by Evaporated Coatings, Inc., Willow Grove, PA (www.evapcoatings.thomasregister.com)

[14]RX-6 optical grease purchased from Rexon, Inc., Beachwood, OH (www.rexon.com)

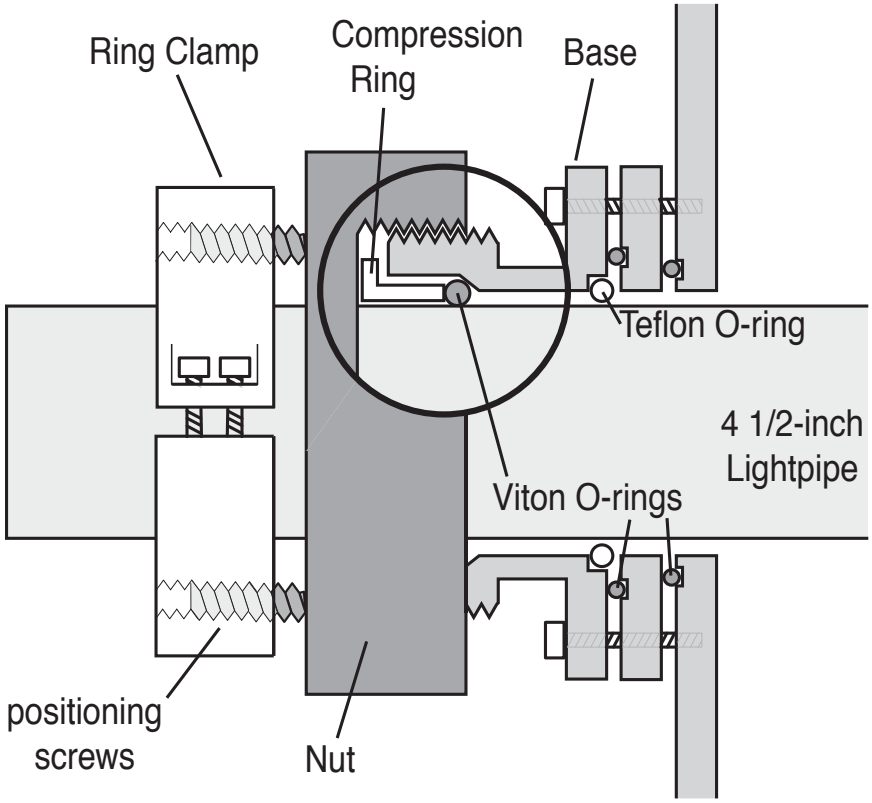

Figure 5.13: The fitting used to form a vacuum seal around the light guide.

minescence is produced in the boron oxide beam dump following neutron irradiation, special steps must be taken to avoid counting luminescence events as neutron decays[25]. While we believe that luminescence creates single, uncorrelated photons, a neutron decay should produce a large, brief pulse of blue light. By requiring that two PMTs detect a signal in coincidence, luminescence backgrounds should be highly suppressed. We have found that requiring coincidence is more effective than requiring a high photoelectron number in a single photomultiplier, since there are occasional large afterpulses seen following single photoelectron events. While afterpulses are rare, the large luminescence signal can easily drown out the small expected neutron decay signal if a single photomultiplier is used.

Luminescence backgrounds are also reduced by using the photomultiplier model Burle 8854. As described in Chapter 4, this photomultiplier (like the Burle 8850) has a high gain GaP second dynode, which gives lower gain dispersion than most other commercial tubes. Because of this, the number of photoelectrons resulting from a given event can be determined with high accuracy, and events that result in a low number of photoelectrons may be easily cut from the data set in off-line analysis. The dark count spectrum of the Burle 8854 is shown in Figure 5.14.

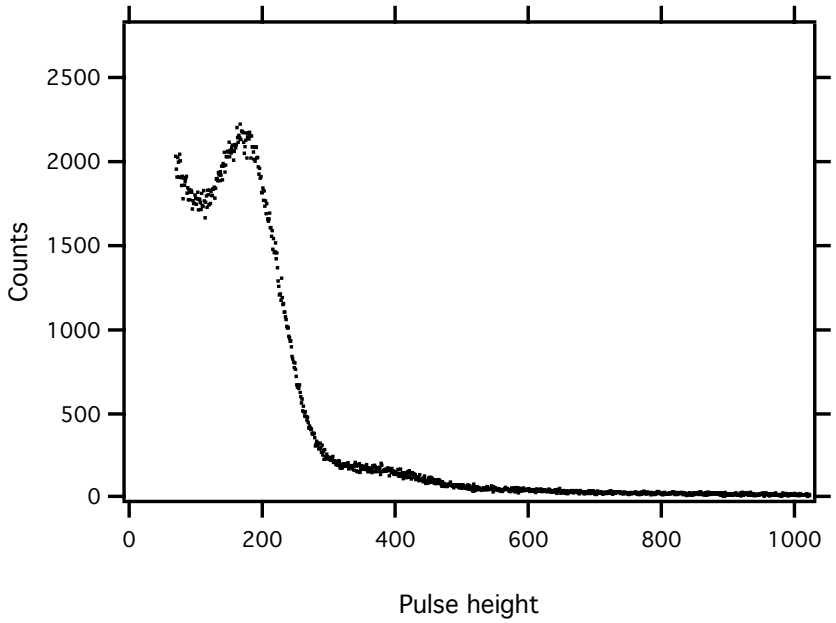

Figure 5.14: The dark count pulse height spectrum of the Burle 8854 photomultiplier. The peak around channel 200 corresponds to single photoelectron events.

Magnetic Shielding

Because photomultiplier gain and quantum efficiency decrease in a magnetic field, and the magnetic field from the trap solenoids is large at the position of the photomultiplier tubes, careful steps must be taken to magnetically shield the photomultipliers. Each photomultiplier is surrounded by a tube of μ-metal, and the optics assembly at

room temperature is surrounded by a large μ-metal "Y"[15]. Finally, a pair of Helmholtz coils is placed around the light guide at room temperature to cancel the field from the pinch coil. When the magnetic trap is on (see next section) and the Helmholtz coil is tuned to the correct current, the field from the magnetic trap decreases the quantum efficiency of the photomultipliers by less than 5%. The arrangement of the magnetic shielding and compensating solenoids is shown in Figure 5.15.

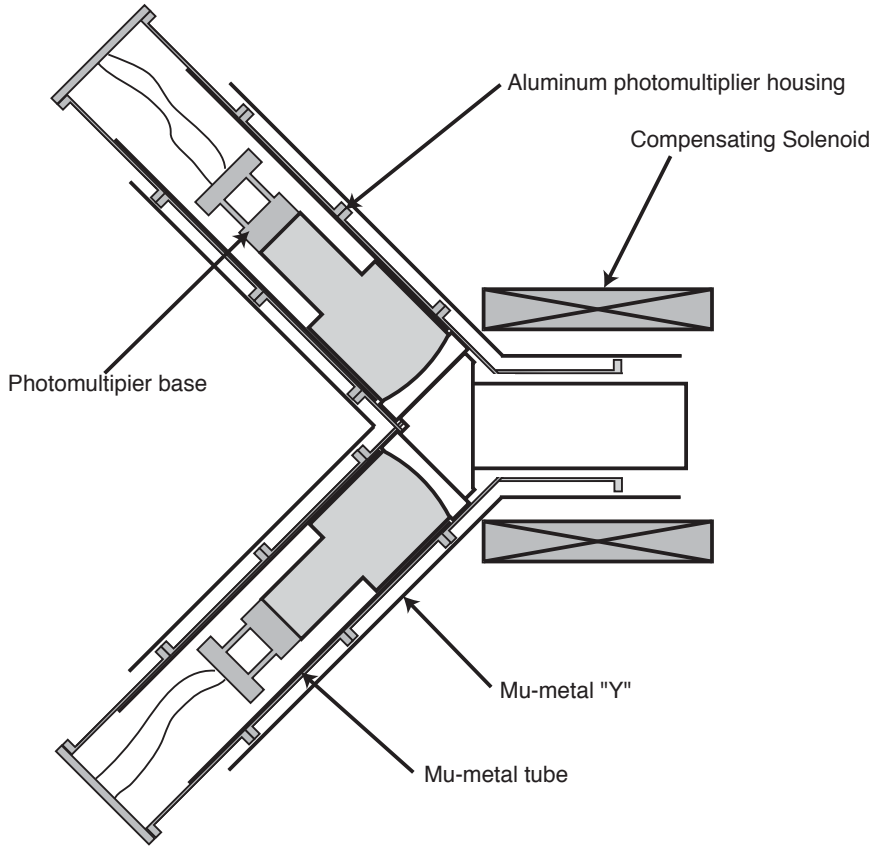

Figure 5.15: Sketch of the magnetic shielding used to protect the photomultipliers from the field generated by the magnetic trap.

[15]Mu-metal tubes and mu-metal "Y" assembly purchased from Amuneal, Inc. Mu-metal tubes are 1 mm thick, Y is 1.6 mm thick.

Detector Calibration

The detector was calibrated by placing a ^{113}Sn source in the center of the trapping region and cooling down the entire experiment. Then, placing a single Burle 8854 photomultiplier at the end of the 77 K light guide, it was found that the 364 keV beta from the ^{113}Sn source caused an average signal of 10.7 photoelectrons to be detected. The value of 10.7 photoelectrons was derived by dividing the channel position of the 364 keV beta peak by the channel position of the single photoelectron peak. The calibration peak is shown in Figure 5.16.

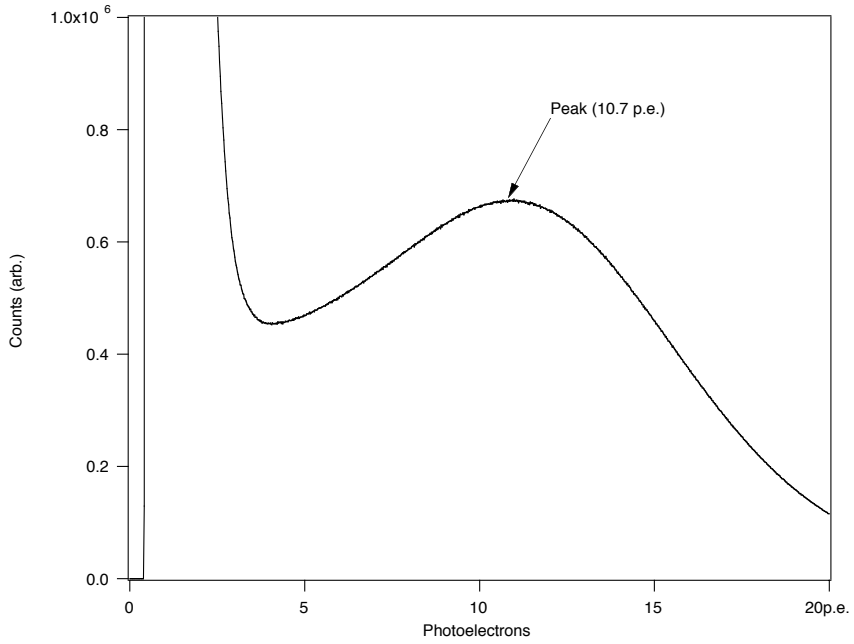

Figure 5.16: The calibration pulse height spectrum, taken with a ^{113}Sn source. A single 8854 photomultiplier is connected directly to the 77 K light guide.

A calibration curve (see Figure 5.17) was also taken with a S83006F photomultiplier; this tube has the disadvantage of high gain dispersion and poor single photoelectron resolution, but has higher quantum efficiency than the 8854 (25% instead of 17% at 440 nm). It displays a correspondingly better peak from the ^{113}Sn source.

Because this tube does not display a distinct single photoelectron peak, it is more difficult to estimate the average number of photoelectrons in the peak; however one may estimate this based on the quoted quantum efficiencies of the 8854 and the S83006F to be $10.7(25/17) = 15.7$ photoelectrons. Despite its higher quantum efficiency, the S83006F was not used in neutron trapping runs; this is because of the considerable single-photon luminescence detected following neutron irradiation of the cell. Because of the poor gain dispersion of the S83006F, luminescence events could be more easily mistaken for neutron decay events.

The efficiency of the light guide splitter was determined by comparing the peak channel position with one photomultiplier to the peak channel position with the splitter installed and two photomultipliers attached. It was found that the light guide splitter is 94% efficient; that is that 47% of the scintillation signal seen with one photomultiplier is seen in each of the two photomultipliers when the light guide splitter is used.

Based on the measured pulse height spectrum, the average detection efficiency for our apparatus can be calculated using a simple Monte Carlo simulation. This simulation takes into account the neutron recoil spectrum, our simple model of position dependence, finite "Y" efficiency, and considers the splitting of photons between the two PMTs to be a Poisson process. The dominant error is the uncertainty in the position dependence of the detection efficiency. The detection efficiency is estimated to be 61^{+8}_{-10} % for a threshold of 2 photoelectrons/PMT.

The efficiency of the optics used to transport light from the trapping region to the photomultipliers was tested using a ^{113}Sn source and a disc of plastic scintillator. The source-scintillator combination makes a pulse of light of constant size. By placing this combination directly against the PMT face, measuring the signal magnitude, and

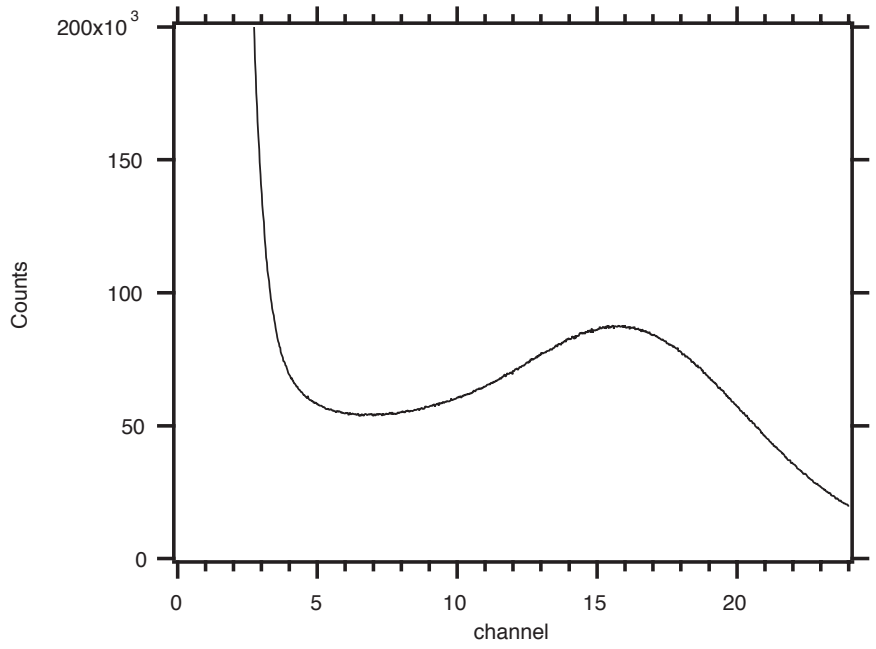

Figure 5.17: The calibration pulse height spectrum using a single S83006F photomultiplier, taken with a ^{113}Sn source. The photomultiplier is connected directly to the 77 K lightguide.

comparing this to the case where the source-scintillator combination is placed at the end of the trapping region, the efficiency of the optics could be determined. Using this method, the optics were found to be 26 ± 3% efficient. Light losses come from reflections at the many window surfaces, scattering at the surface of the light guides, scattering at the cracked quartz on the 4 K window[16] , and absorption by the wires on the 77 K light guide[17]. Combining this result with the expected transmission of the boron oxide beam dump (85%), the total transmission of the optics is 22 ± 3%. Further tests with the source-scintillator combination showed that the optics efficiency could be improved to as much as 49% by repolishing the 77 K light guide, eliminating the wires on the 77 K light guide, ensuring that the 250 mK light guide is

[16]Light lost by scattering in the quartz is measured to be 15%.

[17]Light lost by absorption on the wires is measured to be 30%.

close to the snout window, and minimizing the gap between the 77 K light guide and the 4 K window. Thus, future neutron trapping measurements using this apparatus should enjoy much higher neutron decay detection efficiencies.

5.5 The Magnetic Trap

This section describes the design and construction of our new superconducting Ioffe trap. The Ioffe configuration consists of 4 current bars in a quadrupole assembly. This provides radial confinement, while a pair of pinch coils, each with the same current sense, provides for axial confinement. See Figure 1.8 for a sketch of the Ioffe configuration, and Section 1.4 for a description of how magnetic trapping works.

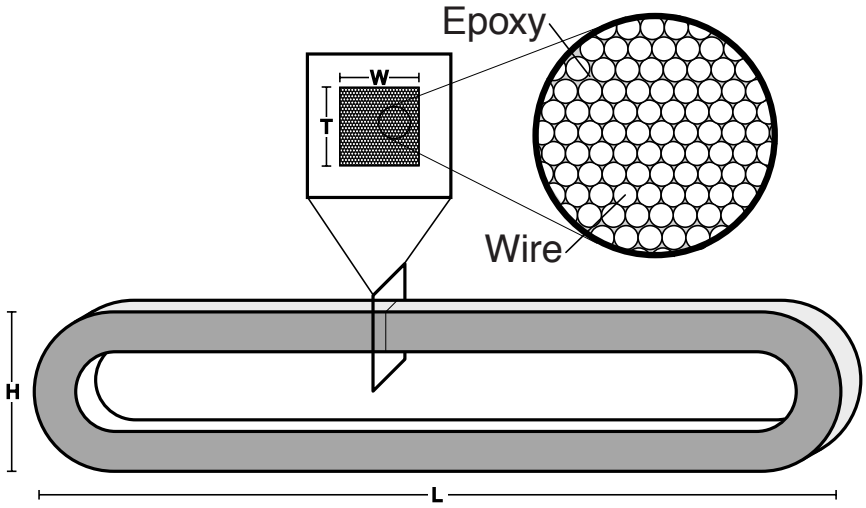

Figure 5.18: The design of a racetrack magnet coil.

A practical way to make the 4 current bars is to use 4 racetrack coils. Each racetrack coil is made from many turns of a single long strand of superconducting wire. The preferred superconducting material is niobium titanium, which is superconducting below 9.8 K. Along with the length, width, and cross-sectional area of the

racetrack coils, an important parameter to consider is the wire diameter. A larger wire diameter implies a larger current supplied to the magnet to achieve a given current density in the racetrack coil. This current is generally supplied from power supplies at room temperature, and the necessary cross-sectional area of the current leads is proportional to the current that must be supplied. Since the heat load on the helium bath is proportional to the cross-sectional area of the current leads, a lower current (and thus a smaller diameter wire) helps minimize liquid helium boiloff. On the other hand, coils designed for smaller wire take longer to wind and quench more often. A sketch showing the construction of a racetrack coilsis shown in Figure 5.18.

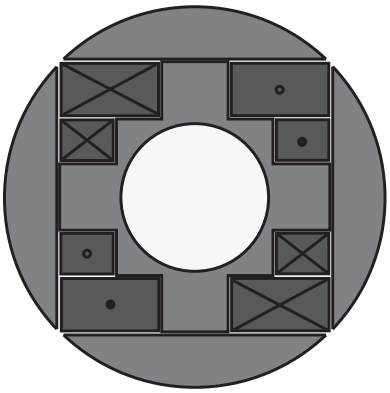

Figure 5.19: A cross-section sketch of the old magnet assembly

The apparatus used to demonstrate magnetic trapping of UCN in May, 1999 used a magnetic trap with an inner bore of 50 mm, and did not reach its critical current of 400 A, running instead at a maximum current of 180 A, corresponding to a trap depth of 1.0 T. This magnet is described in more detail in reference [23]. The racetrack coils were held onto a titanium form, and aluminum spacers were added to the assembly to make it cylindrical (see Figure 5.19). To keep the assembly together as the coils were energized, it was compressed by wrapping Kevlar around it under tension, covering the Kevlar with fiberglass, and then impregnating it with epoxy. Unfortunately,

it became clear that the Kevlar did not provide enough compression to keep the coils from moving when they were energized. One one occasion it was noted that the Kevlar-fiberglass assembly had shifted between cooldowns. It is possible that the Kevlar creeps over time. It is also known that Kevlar expands slightly at low temperature, which may have contributed to the lack of compression.

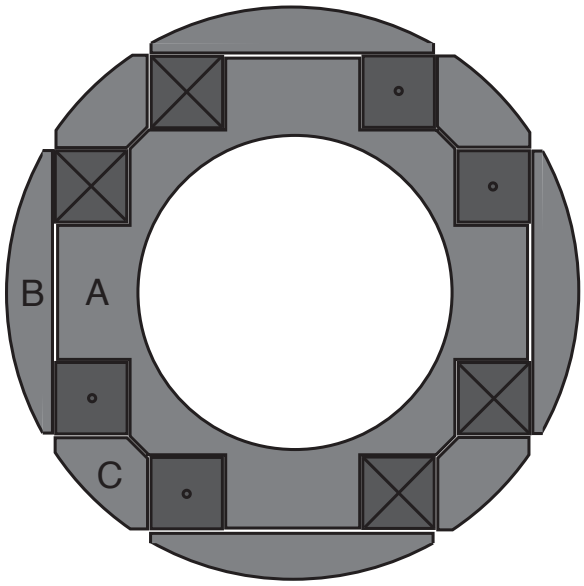

Figure 5.20: A cross-section sketch of the new magnet assembly, showing the titanium form (A) and the two kinds of titanium compressor pieces (B) and (C).

The new magnetic trap was designed to have a larger volume and be demountable. The chief design change was to use aluminum tubes instead of Kevlar to compress the assembly. Most of the assembly was built from titanium, which shrinks only 0.141% as it is cooled to 4 K. Surrounding the assembly with aluminum tubes that fit over the titanium at room temperature, but shrink 0.41% as they are cooled to 4 K, allowed compression as the assembly was cooled. The aluminum tubes thus compress the assembly and preventing the coils from moving as they are energized. The aluminum could be expected to retain its elasticity from cool-down to cool-down, and the tubes

could be removed at room temperature. This meant that the assembly could be taken apart and coils replaced with a minimum of effort.

The new trap was larger than the original and designed to maximize the number of trapped neutrons. The design was constrained by the size of the helium bath inside the current dewar. A number of designs were considered, varying coil cross-section, trap bore, and pinch coil design. The optimal design was determined to have coils of 2.5 cm x 2.5 cm cross-section, with a bore diameter of 105 mm. With a larger bore size, a higher detection efficiency could be obtained, as light could be more easily extracted from the trapping region. Also, the larger trap volume allowed the confinement of many more neutrons than in with the previous trap.

Figure 5.21: Side view of the titanium magnet form on which the racetrack coils fit.

To calculate the force exerted by the coils as they strain against the aluminum tubes, consider that the coils push apart with a force determined by their length, total current, and the magnetic field at the coil.

$$F = INB\ell,$$

where F is the force on one current bar, N is the number of turns of wire in the current bar, I is the current in the wire, and ℓ is the length of the current bar. The pressure p exerted by the current bars on the aluminum tubes is then

$$p = \frac{8F}{\pi d\ell},$$

and thus

$$p = \frac{8INB}{\pi d}.$$

With $I = 320$ A, $N = 776.5$ on average, $B = 3.4$ T, and $d = 193$ mm, one finds that $p = 11.2$ MPa.

For a tubular geometry, the pressure exerted by the compression of the aluminum tube can be determined by

$$p = \frac{2Et\delta d}{d^2},$$

where p is the pressure on the aluminum tube, E is the Young's modulus of the aluminum, t is the thickness of the aluminum tube, δd is the change in diameter of the aluminum tube, and d is the diameter of the tube. In the case of 6061 aluminum at low temperature, $E = 78.4$ GPa. Based on the different expansion coefficients of the materials used to build the magnet, $\delta d = 240$ μm. The diameter d is approximately 193 mm, and the thickness t is 12 mm. Therefore the pressure exerted by the aluminum tubes on the magnet assembly is 12.1 MPa. This is more than the pressure exerted by the coils when fully energized.

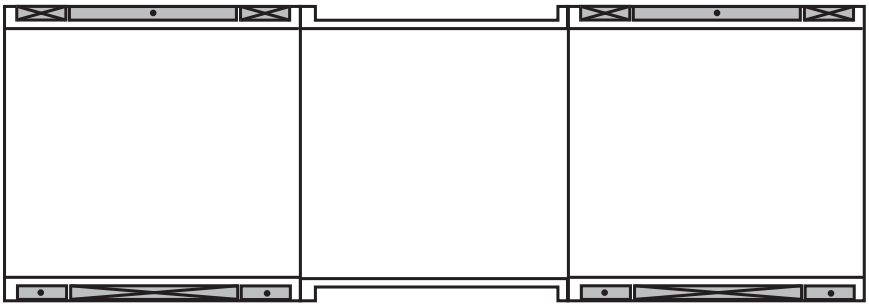

Figure 5.22: Sketch of the solenoid assembly

The magnet form and compression pieces were fabricated from grade 2 commercially pure titanium[18]. The magnet form is 95 cm long, and the two types of compression pieces are 74 cm and 80 cm long. The machining of the titanium was done

[18]The titanium was purchased from Tico Titanium, New Hudson, MI (248) 446-1995 (www.ticotitanium.com).

at the McKay machine shop at Harvard, except for the gun-drilling of the central bore.[19]

The coils were wound by Bob Michniak and Liang Yang using a new magnet winding machine at Harvard[20]. The wire used had a diameter of 740 μm, thinner than the wire used in the previous magnet[21]. The coils are each 80 cm long, with a distance between turnaround centers of 70 cm, and the distance between the centers of the current bars is 7.0 cm. The coils were wet-wound; epoxy was applied to the coils as they were wound, with each new layer of wire covered by a new layer of epoxy[22]. Each layer took about 30 minutes to wind. The layers of wire were separated by fiberglass cloth to prevent cracks in the epoxy from propagating. The four coils had 775, 776, 777, and 778 windings, and were protected by G-10 sheets that had been machined beforehand to cover the faces and sides of the coils. The G-10 sheets thus provided a flat surface that could be compressed evenly by the aluminum tubes, and served as well to protect the coils. As the epoxy set overnight after winding, the coil was compressed to ensure that there were few epoxy-rich regions.

Once the coils were made, they were tested individually. Each of them trained to within 15% of the 320 A load limit (see Figure 5.23). The training behavior of the individual coils is shown in Figure 5.24. The coils were then placed on the titanium form, and the compressor pieces attached. The compressor pieces were bolted tightly to the form, and then the entire assembly was machined to a uniform diameter of 19.3

[19]Gundrilling done by Honematic Machine Corp., Boylston, MA (508) 869-2131 (www.honematic.com).

[20]Winding machine model ER1200MP3 from Bobifil (www.bobifil.com).

[21]Wire used for the new magnetic trap was purchased from Supercon, and had a copper to superconducting ratio of 2:1.

[22]The epoxy used was Shell Resin 815C with 3140 hardener, at a ratio of 1:1.

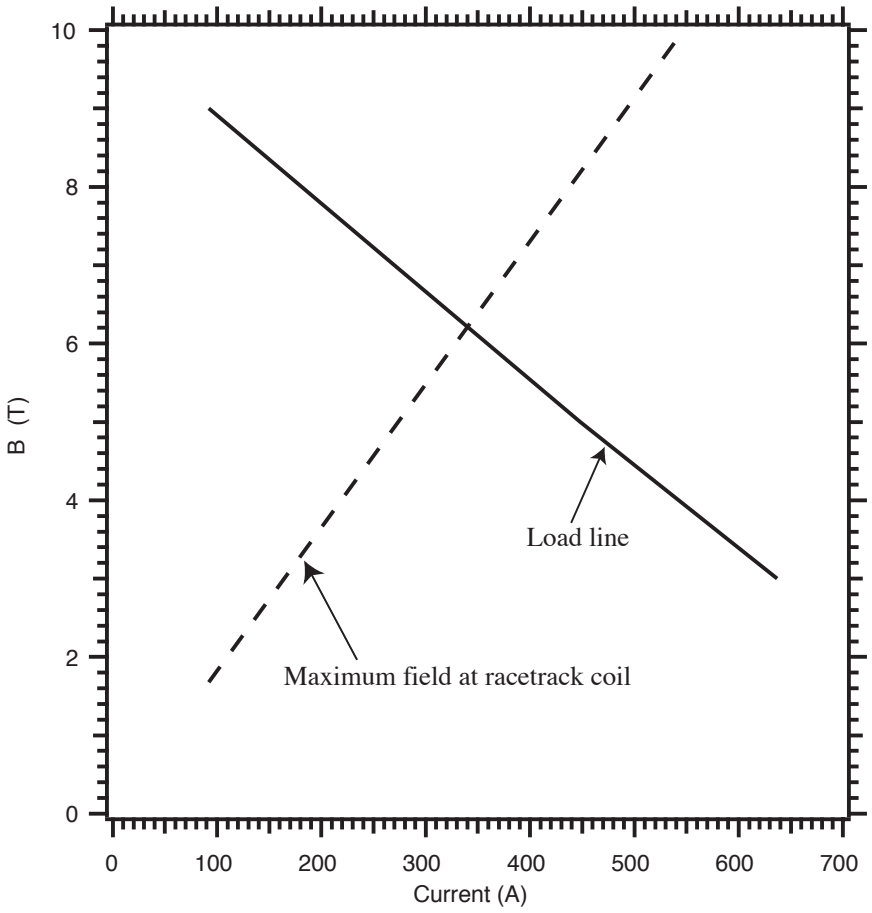

Figure 5.23: Two lines are shown: load line for the superconducting wire used, the linear relationship between the maximum field on the coils and the current through the wire. These two lines meet at a current of 320 A, which is the predicted maximum current that can be carried by the magnetic trap.

cm. Sections of aluminum tube were then machined to slide over the magnet assembly. There were seven tubes machined, each with a thickness of 12 mm. It was found that the titanium magnet assembly could not be easily be machined to a precisely uniform diameter; the diameter varied about 100 μm over its length. Therefore, in order for the aluminum tubes to slide on with as close a tolerance as possible ($< 25\,\mu$m gap between titanium assembly and aluminum tubes), the tubes were machined to each fit over a specified section of the magnet assembly. Each aluminum tube was inscribed

with a numeral from 1 to 7 indicating the order that they should be slid over the quadrupole assembly.

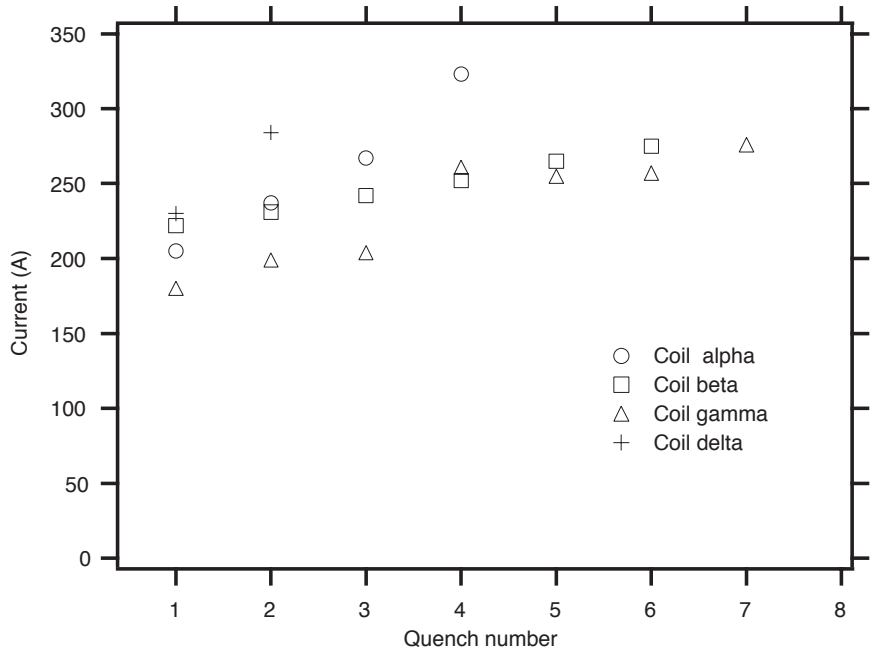

Figure 5.24: The training behavior of the four coils used to build the magnetic trap (denoted alpha, beta, gamma, and delta).

The solenoid assemblies are shown in Figure 5.22. Each assembly has an inner diameter of 21.4 cm and an outer diameter of 24.6 cm. These dimensions were chosen so that the entire assembly could fit into the helium bath with a 7 mm clearance. Within each solenoid assembly there is a "pinch coil" that provides axial confinement and two "bucking coils" that cause the field from the pinch coil to fall off quickly versus z. The solenoid forms were wound on the Harvard winding machine as well, and electrically connected to the quadrupole assembly in series. The whole assembly was mounted within the helium bath of the main apparatus using techniques similar to those used in the past (see reference [23]). A cross-section of the full assembly is shown in Figure 5.25. Current was supplied to the magnetic trap through leads

running from the top of the dewar[23].

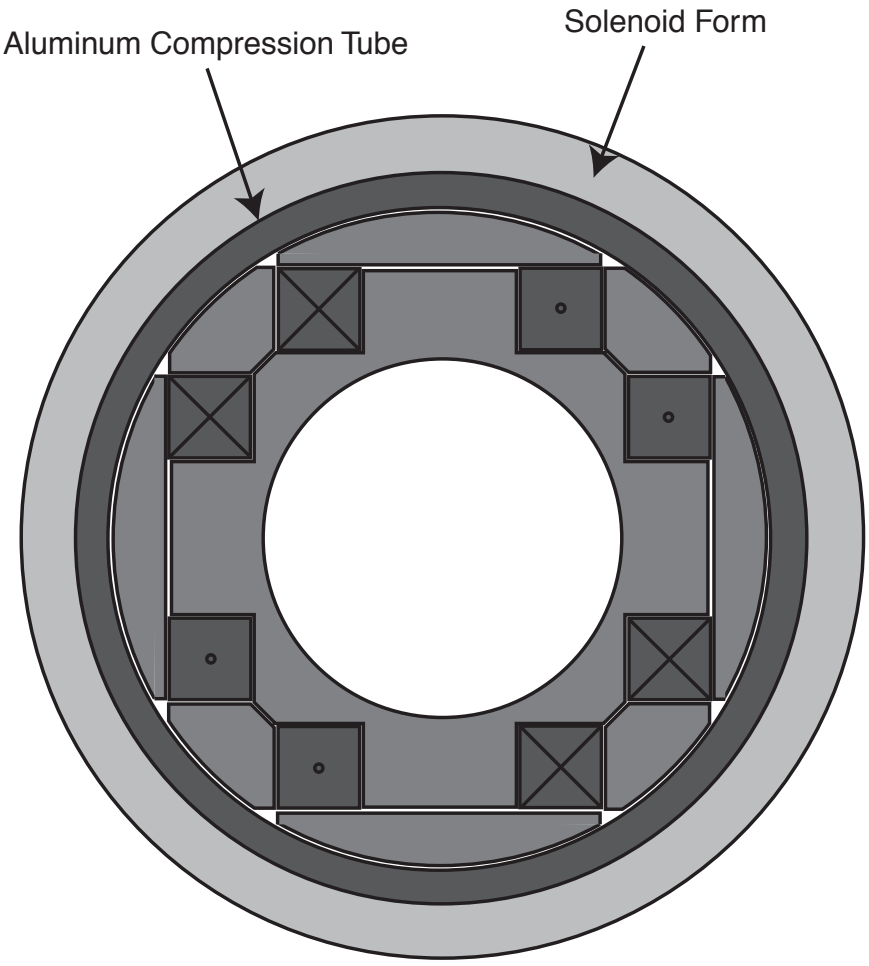

Figure 5.25: Sketch of a cross-section of the magnet assembly.

The magnet assembly was trained multiple times at various months in 2001. Eventually the magnet was run at 170 A, after exhibiting excessive training at higher currents. Details of training behavior are given in reference [25], along with the circuit used to protect the system from quenches.

[23]Model L-250 from American Magnetics, Oak Ridge, TN www.americanmagnetics.com

The field produced with this trap was studied using the program Biot-Savart[24]. This program produces magnetic field profiles along trajectories specified by the user. Figure 5.26 shows how the magnetic field magnitude varies versus radius. This indicates how the magnetic field increases with radius because of the racetrack coils. Figure 5.27 shows how the field magnitude varies down the axis of the trap, showing the axial confinement provided by the two pinch coils. Figure 5.28 shows the field along a line passing through the turnaround region of the a racetrack coil; this is the maximum field at any point on the racetrack coil and determines the maximum current theoretically possible while still maintaining superconductivity. Figure 5.29 shows the field along a line defined by the inner surface of the TPB- coated Gore-tex. The minimum field on this line determines the magnetic trap depth. The asymmetric dip in the field is caused by the partial cancellation of the trapping field by the divergent field produces by the pinch coils. Because the pinch coil diameter is relatively small, the field that it produces is fairly divergent at the trap radius, and this has a significant effect on the trap depth.

5.6 Background Suppression

Certain kinds of events can mask neutron decays within the trapping region. The most pernicious of these is gamma ray Compton scattering within the helium bath. Because Compton scattering transfers gamma ray energy to an electron, it is virtually indistinguishable from a beta-decay event. And because gamma rays that scatter in the helium contribute to backgrounds, considerable improvements in statistical accuracy can be gained by shielding the experiment.

The horizontal section of the experiment is surrounded by lead walls on all sides, 10

[24]Biot-Savart, Cirrus Software, Inc., Kaleden, BC, Canada.

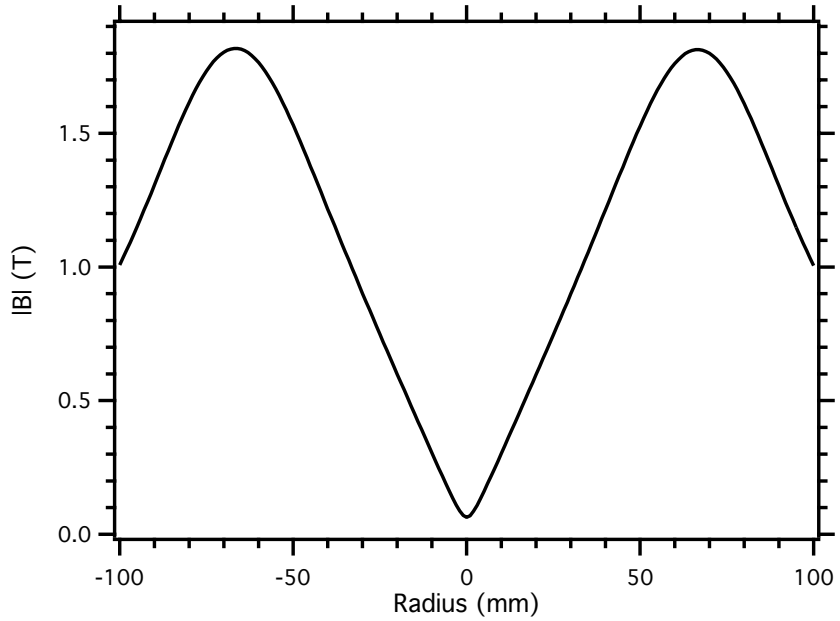

Figure 5.26: Magnetic field magnitude versus radius at $z = 0$, along a line perpendicular to the racetrack coils.

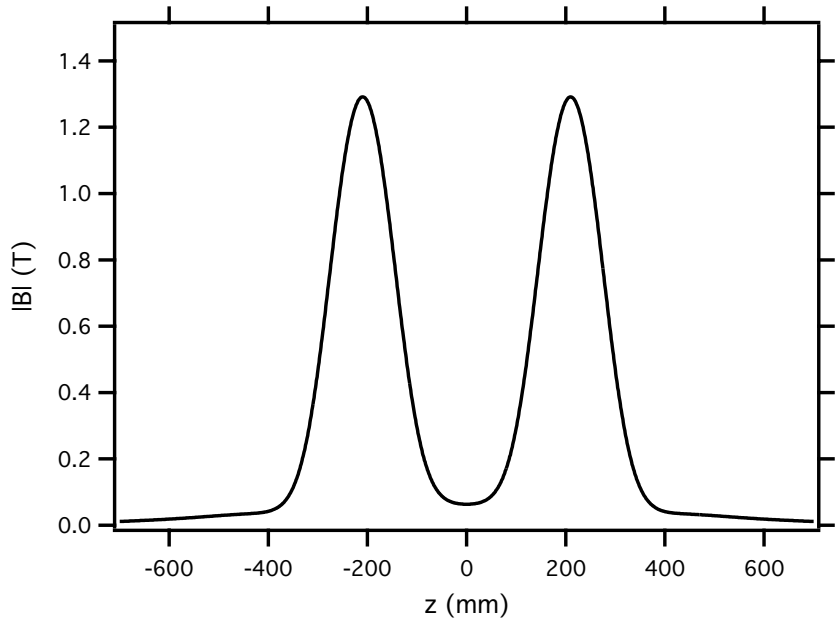

Figure 5.27: Magnetic field magnitude versus z along the central axis of the trap.

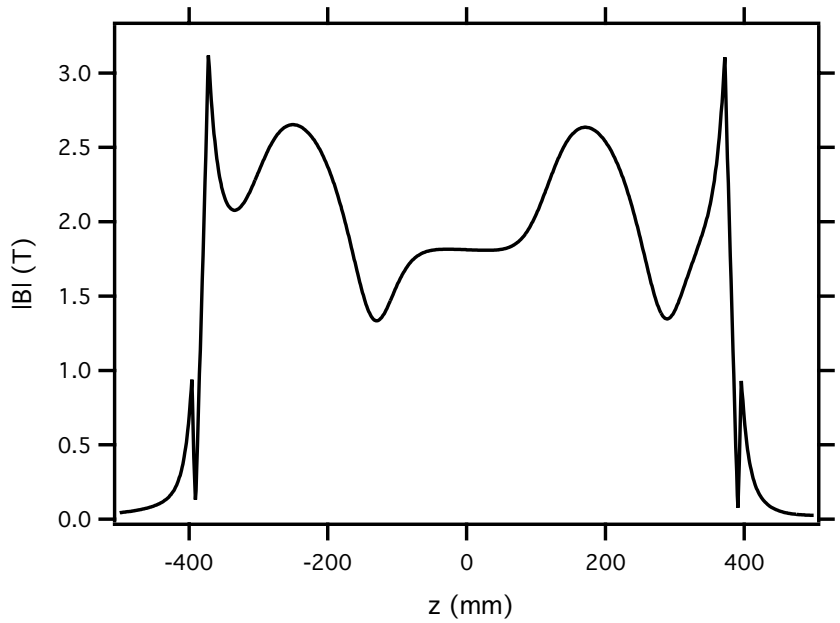

Figure 5.28: Magnetic field magnitude versus z on a line passing through a racetrack coil. The field at the racetrack turnaround is the maximum field felt by the coil, and determines the maximum current it can carry. The racetrack coil extends from -400 to 400 mm.

cm thick. This is important for minimizing gamma ray backgrounds. There are holes in the lead shielding, however. For example, there is a large hole where the vertical section attaches, and there are holes where the photomultiplier housings protrude. Future incarnations of the experiment could improve on the completeness of the lead shielding, blocking holes more carefully and using thicker lead walls.

A second sort of background is neutron-induced activation. In order to keep this to a minimum, the selection of materials to be placed in the neutron beam was done very carefully. All metals are shielded with neutron absorbing lithium- or boron-containing compounds, especially boron nitride. All of the materials inside the cell have low activation cross-sections or short decay lifetimes (such as carbon, hydrogen, oxygen, boron, and fluorine). Some materials outside the cell (such as the beryllium A-side windows) are prone to activation and must be chosen carefully. A more detailed

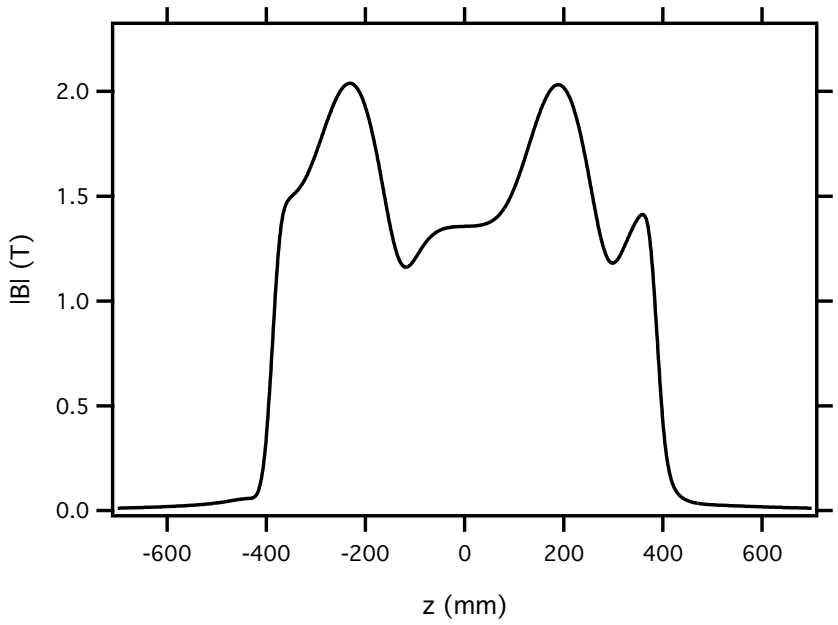

Figure 5.29: Magnetic field magnitude versus z on a line passing along the Gore-tex tube. This field determines the trap depth.

analysis of activation backgrounds in this experiment can be found in [25].

It has recently been realized that the reaction $^{10}\mathrm{B}(\alpha, \mathrm{n})^{13}\mathrm{N}$ is likely to be a significant source of time-dependent background. This reaction likely occurs within the boron nitride shielding material, and was overlooked because it is second-order. The boron shielding absorbs neutrons via the reaction $^{10}\mathrm{B}(\mathrm{n}, \alpha)^{11}\mathrm{B}$, which emits an alpha of energy 1.48 MeV. But it is then possible for a different boron nucleus to absorb the alpha particle and emit a neutron, thus producing $^{13}\mathrm{N}$. This isotope then decays by positron emission with a lifetime of 863 seconds. Though the cross-section for the $^{10}\mathrm{B}(\alpha, \mathrm{n})^{13}\mathrm{N}$ reaction is small (0.02 barns) because of the Coulomb barrier that the α particle must penetrate to activate $^{10}\mathrm{B}$, the large number of α particles emitted by the boron nitride yields an appreciable rate of $^{13}\mathrm{N}$ decays. We estimate that $^{13}\mathrm{N}$ nuclei are produced in the boron oxide beam dump at a rate of 20 s^{-1}, and a large fraction of the decays deposit energy in the superfluid helium. Like the activation of the

Brazilian glass, the activation of the boron nitride was unexpected, as second-order activation processes were not considered in the initial design of the experiment.

A final source of background in this experiment is cosmic ray muons. These are created by high-energy collisions in the upper atmosphere, and result in a muon flux at the surface of the Earth of 1 $cm^{-2}\,min^{-1}$. Because the muons pass directly through the experiment, they can ionize the liquid helium and cause scintillations, just like neutron beta-decays. But because few of the muons stop in the experiment, these events can be actively vetoed using slabs of plastic scintillator placed under experiment. Each muon "paddle" consists of a 2.5 cm x 32 cm x 1.42 m slab of scintillator, an acrylic condensing region (40 cm long), and a photomultiplier tube. The muon paddles are wrapped in black cloth to block room light. The muon paddles are arranged under the experiment as shown in Figure 5.30. By vetoing events that cause both the 8854's to trigger and any muon paddle, the constant background level was reduced by 17 s^{-1}.

5.7 Data Acquisition

The data acquisition system is described in full detail in reference [25] and this section is meant only as a brief summary. In short, the data acquisition system records events in which both 8854 photomultipliers looking at the experimental cell fire, and the muon paddles do not. For each event, the data acquisition system records the time at which the event occured and the digitized waveforms from the two main photomultipliers. The data acquisition system is controlled by a Power Macintosh G3 computer, which also controls the slider and blocker, controls the magnet current, and turns the photomultipliers on and off at appropriate times during the experiment.

The anodes of the photomultipliers are connected to the inputs of a NIM amplifier,

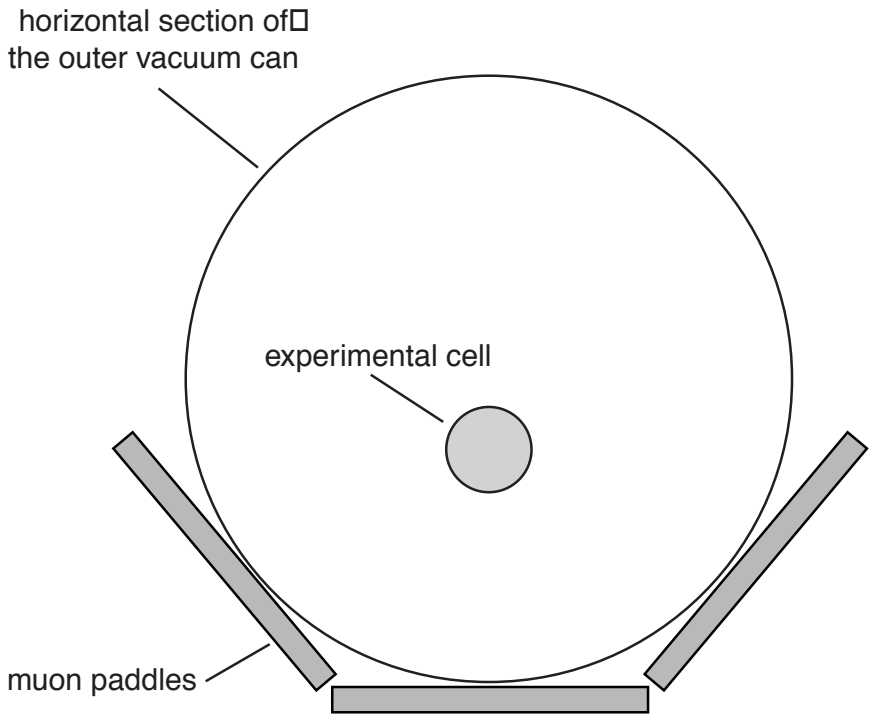

Figure 5.30: Arrangement of the muon paddles

and the amplifier outputs are connected to the digitizer cards, denoted "master" and "slave". The digitized photomultiplier pulses and event times are saved in a byte block format. A typical digitized photomultiplier pulse is shown in Figure 5.31.

The amplifier signals are also sent into NIM discriminators, which are then ANDed to form a coincidence signal. The four muon paddle outputs are amplified and sent into four different discriminators. The discriminator signals are fanned together to form a single veto signal. If the cell coincidence circuit fires but the muon veto does not, then the photomultiplier traces and event time are saved. Runs were saved in files whose names reflected the date in which they were taken. For example, the file 080301003.daq is a run taken on August 3, 2001, and is the third file saved that day. The programs used to analyze the data taken in August, 2001 are discussed in Appendix A of this thesis.

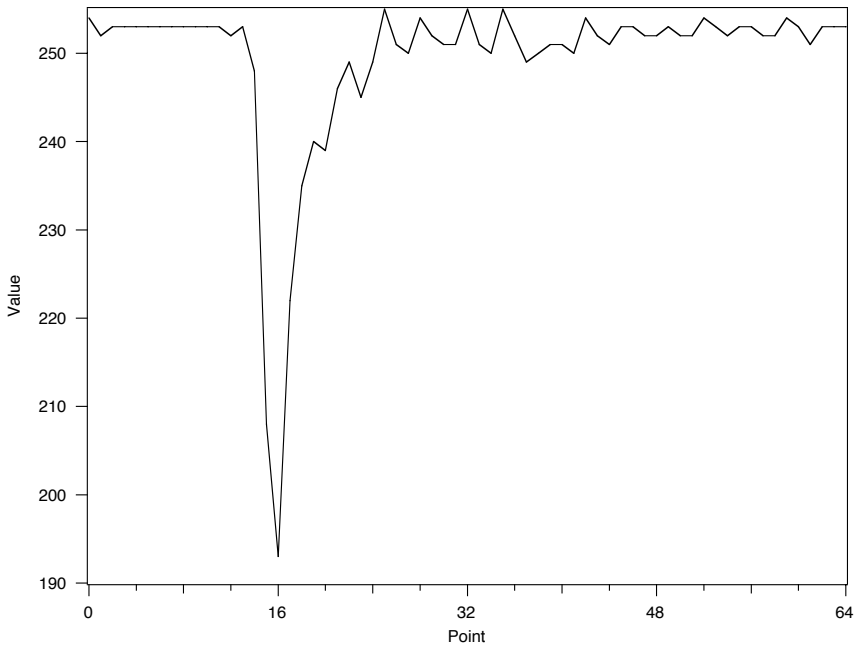

Figure 5.31: A typical digitized PMT pulse

Chapter 6

Data Analysis

6.1 Data Collection

Data are collected in a series of runs. In each run, neutrons are first loaded into the trap, and then their decay is observed as a function of time. To load the trap, the neutron beam is turned on for 2100 s. As shown in Fig. 6.1, the neutron population in the trap increases monotonically while the neutron beam is on, approaching the theoretical maximum. Then the beam is turned off and the photomultiplier tubes are turned on to watch for neutron decays. This period lasts for another 2700 s. During the beam-off period, the neutrons in the trap decay or are lost from the trap. Assuming that spurious trap losses are small, the rate of neutron decay detection should reflect the neutron beta-decay lifetime. After the collection period, a pause of 100 s is observed, and the process is repeated in a new run.

In practice, we perform two sorts of runs, called "positive" and "negative". In positive runs, the magnetic field is at its maximum value the entire run. In a negative run, the magnetic field is off while the neutron beam is on, then raised to its maximum value just before the beam is turned off, trapping very few neutrons. By subtracting

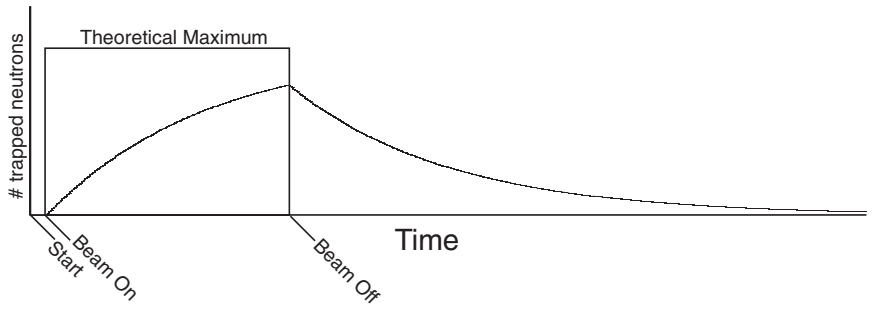

Figure 6.1: A plot of the predicted trapped neutron population versus time.

negative runs from positive runs, backgrounds may be suppressed leaving the neutron decay signal. The time sequence for positive and negative runs is shown in Figure 6.2. Each run lasts 4900 s, so ideally 17 runs can be performed per day.

6.2 Data Cuts and Thresholds

In order for an event to be recorded by the data acquisition system, both photomultipliers viewing the detection region must trigger within 20 ns of each other. This requirement was put in place in order to suppress single-photon backgrounds. There is a significant rate of uncorrelated photons from neutron-induced luminescence in the cell; requiring coincidence is highly effective in removing these uncorrelated events from the collected data. The accidental rate R_a for uncorrelated photons is

$$R_a = 2R_1R_2\tau,$$

where τ is the discrimination binwidth created by the triggering electronics, and R_1 and R_2 are the trigger rates for the two PMTs.

The rate of accidental coincidences is rather uncertain, as our data acquisition system did not record single photon rates in each photomultiplier. However, a special measurement of the rate from one of the photomultipliers yielded 19,000 to 11,000

counts per second between 100 and 600 seconds after the beam was turned off. This predicts a rate of 4 to 14 s^{-1}, in accord with the measured 1 photoelectron data. However the accidental coincidence rate at higher thresholds should be much smaller, as less than 10% of the single photoelectron events are misinterpreted for two photoelectron events (see Figure 5.14). This implies an accidental count rate roughly 100 times smaller for a two-photoelectron threshold, and even lower rates at higher thresholds. Therefore luminescence backgrounds are not significant for thresholds higher than two photoelectrons. The requirement of coincidence is critical for cutting unwanted time-dependent backgrounds.

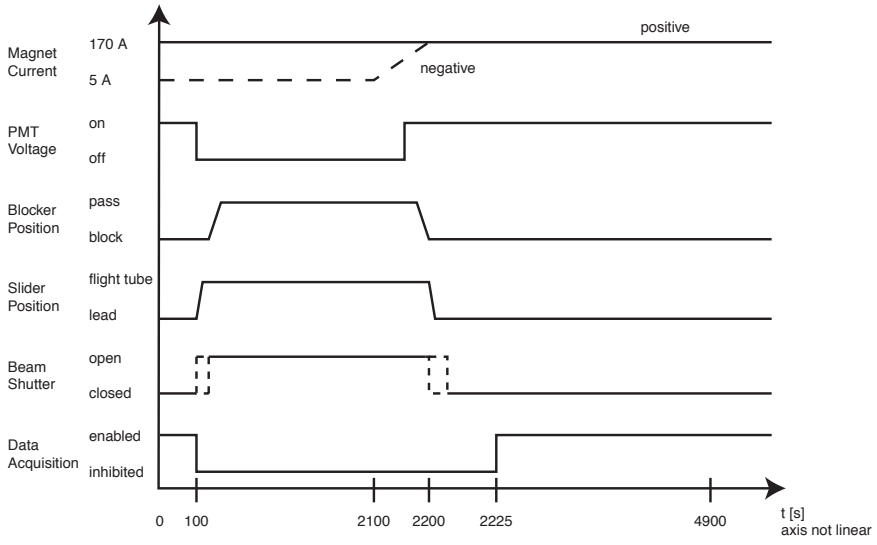

Figure 6.2: Time sequence for data collection.

If the discriminator signals from both PMTs overlap in time, and if none of the muon paddles trigger, then the event is recorded by the data acquisition system. Both PMT pulses are digitized and saved, and the time of each event is also recorded. After a run is finished, the data is saved in a byte block format; each byte block consists of a series of digitized pulses or a series of time stamps.

Table 6.1: Threshold as a function of photoelectron number.

Threshold (p.e.)	Pulse Area
1	11
2	30
3	49
4	68
5	87
6	106
7	125
8	144
10	182
12	220
15	277

This raw data is converted to a usable form in software, which is described fully in Appendix I. Simply, each event is characterized by two pulse areas (one for each PMT), and a time. The pulse area is expressed in terms of photoelectron number (p.e.) by dividing it by an estimated size of a one-photoelectron pulse (see Table 6.2). The data is then sorted such that events that are larger than a specified number of photoelectrons are kept. Only the lower threshold was varied since there are few events at high thresholds. After sorting, data events from the runs that are being analyzed (usually a set of runs at a given experimental condition) are histogrammed to form a single data set for each type of run. The histograms for the positive and negative sets of runs are subtracted to form a single data set for curve fitting purposes. The resulting histogram is fit to the function

$$Ae^{-kt} + B$$

where t is the time after the neutron beam is turned off. A non-linear, least-squares

fit is performed using the Igor Pro fitting routine.[1]

6.3 Backgrounds

The collected data exhibited both time-independent and time-dependent backgrounds, both of which had significantly larger rates than the expected neutron decay signal. These backgrounds result largely from ionizing radiation interacting with the helium bath and light collection optics, and proved to be a significant obstacle to precise measurement of the neutron decay curve. The measured background rates before the cell was exposed to neutrons are summarized in Table 6.2. Also shown is the background rate when the cell is emptied of helium. It can be seen that events in the helium create the largest fraction of the constant background. This can be explained by the fact that scattering events in the optics only make Cerenkov radiation, which is not created in large amounts. Events in the helium, on the other hand, create copious amounts of scintillation light, which is easily detected by the photomultipliers. Background events are probably largely the result of gamma rays scattering in the detector. These gamma rays come from long-lived radioactive K, U and Th isotopes in the apparatus, as well as from prompt neutron capture gammas in the surrounding instruments in the guide hall. Other sources might be cosmic rays that miss the muon paddles, or perhaps radioactive decays in the photomultiplier windows. Made of glass, the PMT windows contain a significant amount of potassium, and Cerenkov flashes in one PMT window can be seen by both.

Time-dependent backgrounds are also an issue. In Figure 6.3 the average of the 200 mK positive runs and the average of the 200 mK negative runs are shown, along

[1]Igor Pro Version 4.04, WaveMetrics, Inc., Lake Oswego, OR, http://www.wavemetrics.com

Table 6.2: Count rates in coincidence with the detection region empty or full of ultrapure helium. The rates are tabulated as a function of the lower level threshold number of photoelectrons required on each PMT. Thus, for a 2 photoelectron threshold, the total count rate of events where at least 2 photoelectrons are detected in coincidence on each PMT is reported. Also shown is the fraction of the background (± 0.01) at each threshold that is from background events in the light collection optics. Note that these are background rates before subtracting negative runs from positive runs.

Threshold (p.e.)	Count rate Empty [s^{-1}]	Count rate Full [s^{-1}]	Fraction due to acrylic
1	19.2	30.5	0.63
2	9.3	17.4	0.53
3	5.4	12.5	0.43
4	3.7	9.8	0.38
5	2.7	8.1	0.34
6	2.2	6.9	0.31
7	1.7	6.0	0.29
8	1.4	5.3	0.27
9	1.2	4.7	0.25
10	1.0	4.2	0.24
15	0.5	2.8	0.19
20	0.3	2.1	0.16

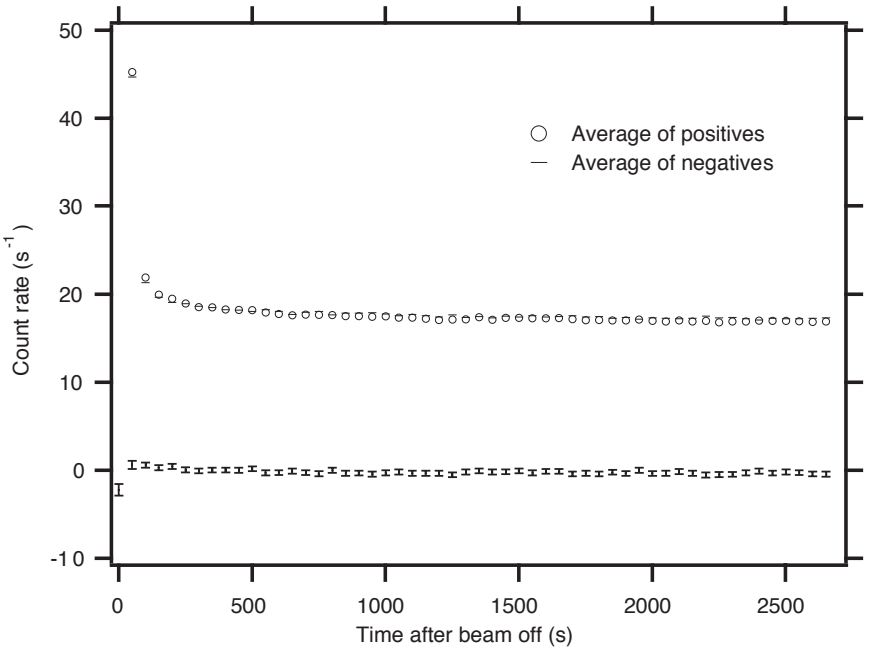

Figure 6.3: The average positive and average negative runs, with a cell temperature of 200 mK. Only events with 2 or more photoelectrons detected in each PMT are counted. The difference is shown below, with error bars.

with the difference between the two. This data is cut at 2 photoelectrons, so any luminescence contribution to the background should be small. Because the background is clearly time-dependent, there must be activation by the neutron beam. The time-dependent background is seen at higher thresholds as well; Figure 6.4 shows the same data cut at 5 photoelectrons. Clearly, activation contributes to the time-dependent background.

The activation background does not fit well to a single exponential; presumably this is because there are several species of activated nuclei contributing to the background. Some suspect nuclei are ^{20}F (half-life 11.0 s), ^{28}Al (half-life 135 s), and ^{66}Cu (half-life 306 s). Fluorine is present in large amounts in the Gore-tex plastic lining the cell walls and most likely creates the quickly decaying component seen in both the 2+ and 5+ data. Aluminum is present in large quantities in the dewar, and cop-

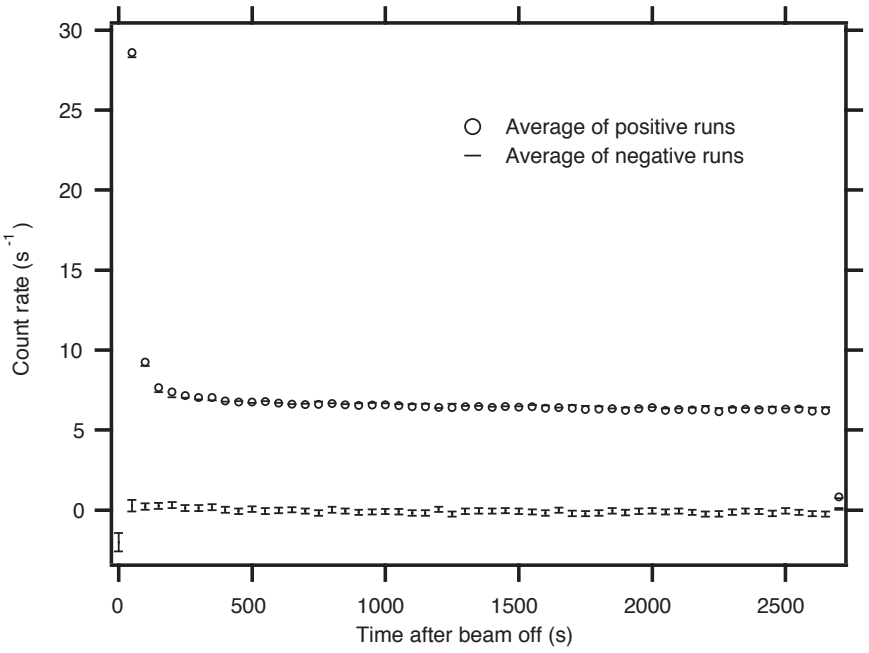

Figure 6.4: The average positive and average negative runs, with a cell temperature of 200 mK. Only events with 5 or more photoelectrons detected in each PMT are counted. The difference is shown below, with error bars.

per is present in the copper-nickel cell tube. Though the dewar and cell are carefully shielded from neutrons with boron nitride, the inevitable conclusion is that, somehow, neutrons managed to activate these materials.

6.4 Data

Data were taken at a variety of temperatures, and in the final set of runs, normal helium was used instead of ultra-pure ^{4}He. Table 6.3 summarizes the data set. Some runs were not used in the data analysis; these were excluded for excessive noise or corrupted data files and comprise about 10% of the total data collected. These runs are not included in Table 6.3.

Table 6.3: calendar

Data set	Temperature (mK)	Number of positive runs	Number of negative runs	Date range
"200 mK"	200 - 230	34	36	8/3 - 8/4, 8/6 - 8/9, 8/15 - 8/16
"300 mK"	280 - 330	13	11	8/9 - 8/12,8/18 - 8/19
"400 mK"	400 - 450	14	13	8/6, 8/16 - 8/18
"600 mK"	510 - 640	27	23	8/5 - 8/6
"750 mK"	740 - 760	17	16	8/19 - 8/21
"1 K"	1020 - 1130	19	19	8/12 - 8/15
^{3}He	200 - 250	15	13	8/23 - 8/25

6.5 Analysis

This section contains the fits to all of the aforementioned data sets. In general, it is seen that the data fits best to a lifetime that is significantly less than the neutron beta-decay lifetime. The intensity of decays is also less than that expected from the combination of the theory of the superthermal effect and Monte Carlo simulations[25].

Cold data

For helium temperatures less than 600 mK, upscattering of UCN by phonons in the superfluid helium is expected to be a small effect[1]. One can thus combine the 200, 300, 400, and 600 mK data sets into a single set. Figure 6.5 shows this data set with a threshold of 2 photoelectrons, as well as the best fit to this data. The fit lifetime is $482\ ^{+85}_{-63}$ s, considerably shorter than the Particle Data Group (world average) value of 885.7 $\pm$0.8 s [5] for the neutron beta decay lifetime. This is a 3.0 σ discrepancy.

Table 6.4: Fit parameters of combined 200-600 mK data as a function of threshold.

Threshold (photoelectrons)	k (s^{-1})	A (s^{-1})	B (s^{-1})
1	0.0019888 ± 0.000133	3.3087 ± 0.124	0.23434 ± 0.037
2	0.0020741 ± 0.000311	0.95502 ± 0.0834	-0.10295 ± 0.0231
3	0.0023014 ± 0.000369	0.74118 ± 0.0744	-0.077574 ± 0.0174
4	0.0020536 ± 0.000328	0.64586 ± 0.0596	-0.051907 ± 0.0167
5	0.0019743 ± 0.000287	0.58171 ± 0.0473	-0.042303 ± 0.0142
6	0.0019743 ± 0.000287	0.47874 ± 0.0377	-0.031859 ± 0.0129
7	0.0017148 ± 0.000283	0.41711 ± 0.0341	-0.026604 ± 0.0132
8	0.0015738 ± 0.000287	0.36503 ± 0.0304	-0.027543 ± 0.0139
10	0.0014503 ± 0.000319	0.29929 ± 0.0276	0.089566 ± 0.0148
12	0.0014189 ± 0.000396	0.20975 ± 0.024	-0.019046 ± 0.0135
15	0.0017382 ± 0.000571	0.13411 ± 0.022	-0.0089764 ± 0.00835

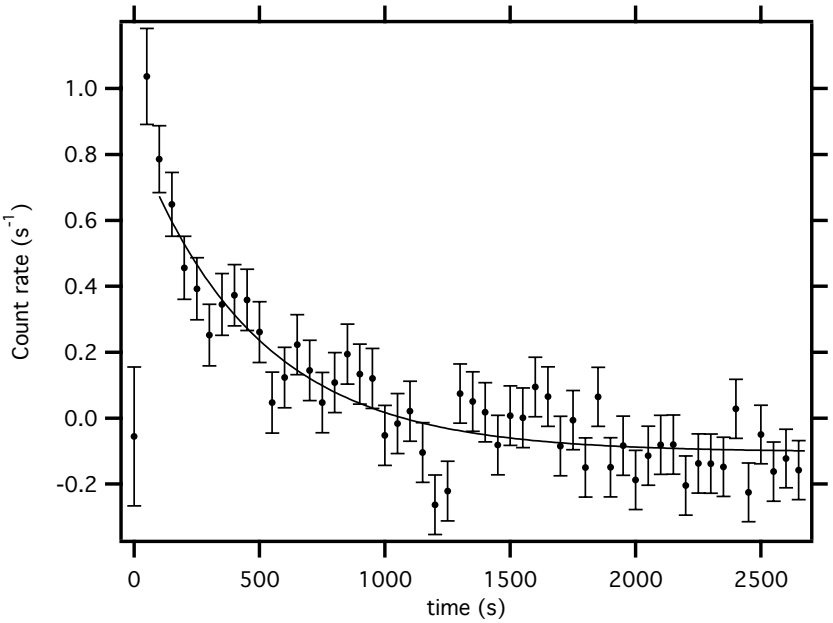

Figure 6.5: The difference between average positive and negative runs, for temperatures between 200 and 600 mK. Also shown is the best fit to the data. Fit parameters are $A = 0.95502 \pm 0.0834$, $k = 0.0020741 \pm 0.000311$, and $B - 0.10295 \pm 0.0231$.

The intensity of the decay signal is also signicantly less than calculations based on the superthermal effect predict[1]. For a 2 photoelectron threshold, the fit decay intensity is 0.96 ± 0.08 s^{-1}. Given an estimated detection efficiency of 61^{+8}_{-10}% (see section 5.4, this implies an actual initial rate $1.57^{+0.24}_{-0.29}\,s^{-1}$. This does not agree with the predicted rate of 3.1 s^{-1}, which assumes a UCN production rate of 3.4 ± 0.6 UCN s^{-1}[1, 25] from a monochromatic 8.9 Å beam (see Section 5.2). However, if the observed short lifetime results from neutrons being lost from the trap without being observed by the detector, then the decay amplitude will be modified by a factor τ_{trap}/τ_n. The predicted decay amplitude would then be $1.8 \pm 0.3\ s^{-1}$, consistent with our measurement.

Fits are also performed at a variety of other thresholds. From Table 6.4, one can see that the fit lifetime is consistent across a wide range of thresholds, while the

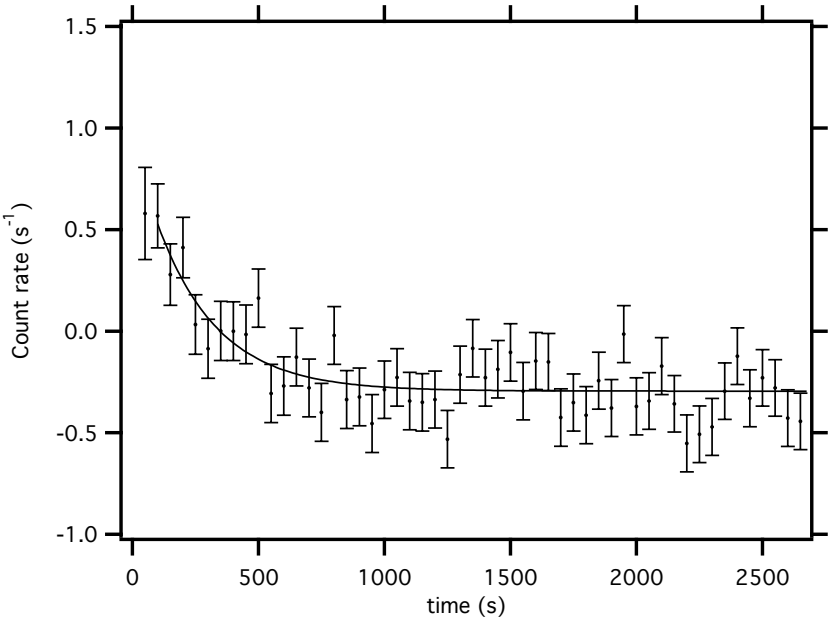

Figure 6.6: The difference between average positive and negative runs in the 200 mK data, with a threshold of 2 photoelectrons in each PMT. Also shown is the best fit to the data. Fit parameters are $A = 1.25 \pm 0.26$, $k = 0.0041 \pm 0.0010$, and $B = -0.295 \pm 0.026$.

intensity of the time varying difference decreases with increasing threshold. This presumably reflects the decreasing efficiency for detecting neutron decays as the threshold is increased.

The "cold data" discussed above is comprised of data taken at a variety of temperatures in the range 200-600 mK. It is also interesting to study the subsets of data acquired at different helium temperatures. Figure 6.6, Figure 6.7, Figure 6.8, and Figure 6.9 show the data and best fit for data sets denoted as 200, 300, 400, and 600 mK respectively. One would expect that if upscattering by phonons were significant, then the fit decay rate k would increase with higher temperatures. However, the opposite is the case; the coldest data set (200 mK) fits to the highest decay rate ($k = 0.0041 \pm 0.0010$), compared to $k = 0.00148 \pm 0.00049$ for 600 mK.

If the data is cut at 1 photoelectron, the fit decay intensity A is substantially larger

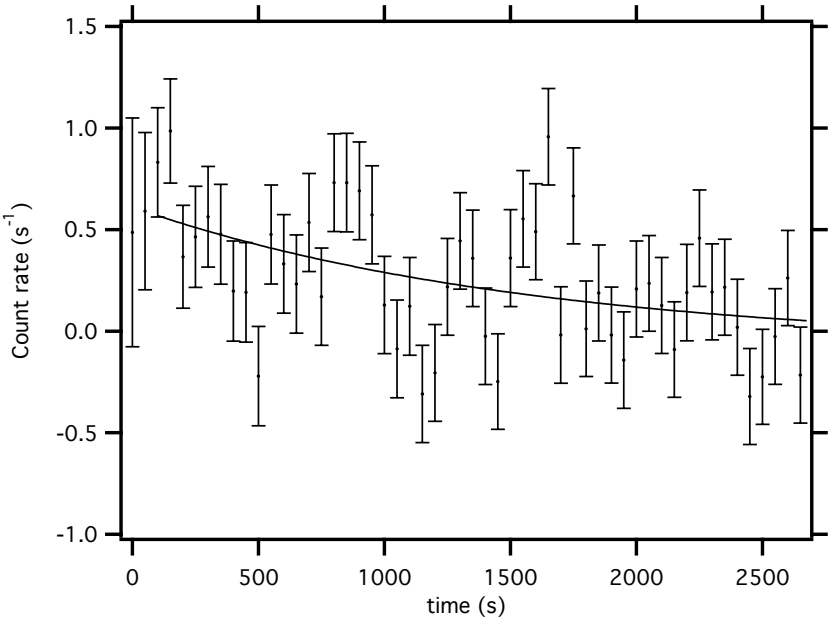

Figure 6.7: The difference between average positive and negative runs in the 300 mK data, with a threshold of 2 photoelectrons in each PMT. Also shown is the best fit to the data. Fit parameters are $A = 0.69 \pm 0.33$, $k = 0.00063 \pm 0.00085$, and $B = -0.08 \pm 0.42$.

than at higher thresholds. This large single photoelectron signal probably arises from a difference in the accidental coincidence rate between positive and negative runs, implying that the luminescence rate depends whether the magnetic field was on or off while the beam was on. This hypothesis is supported by the fact that this 1 photoelectron decay is seen in runs in which the superfluid helium is doped with ^{3}He (see Section 6.5).

Warm data

Data were also acquired at warmer temperatures. This was done to check that the signal seen at lower temperatures was indeed arising from the decays of trapped neutrons. As can be seen from Figure 6.11 and Figure 6.12, the difference between

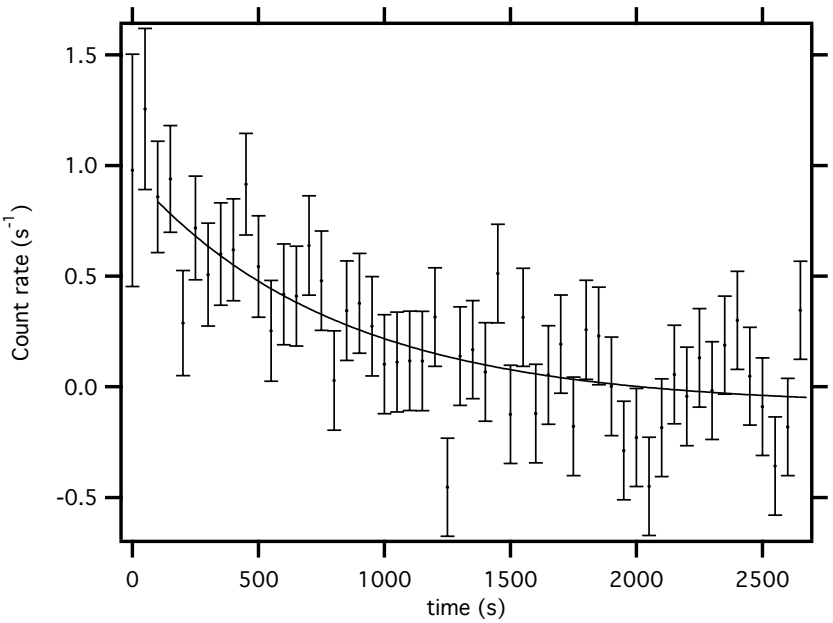

Figure 6.8: The difference between average positive and negative runs in the 400 mK data, with a threshold of 2 photoelectrons in each PMT. Also shown is the best fit to the data. Fit parameters are $A = 1.04 \pm 0.13$, $k = 0.00124 \pm 0.00044$, and $B = -0.09 \pm 0.10$.

positive and negative runs is suppressed at higher temperatures, as predicted by the theory of neutron upscattering[1].

^{3}He data

Data were also acquired at a low temperature, but with the isotopically pure ^{4}He replaced with standard helium from a gas bottle (^{3}He/^{4}He $\sim 10^{-7}$, in which neutrons are captured by the ^{3}He in less than 1 s). Removing the ultra-pure ^{4}He and replacing it with standard helium took two days, after which the temperature of the cell was lowered to about 200 mK. Figure 6.15 shows the difference between average positive and negative "^{3}He runs". There is no sign of a decay signal in this data. If the decay rate is fixed to that seen in the 200 mK data ($k = 0.0041$), the fit decay amplitude

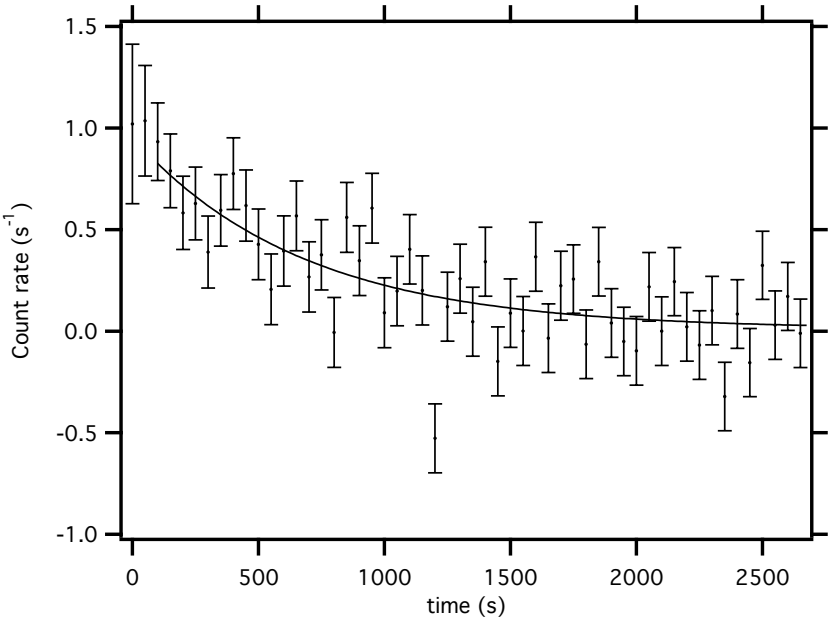

Figure 6.9: The difference between average positive and negative runs in the 600 mK data, with a theshold of 2 photoelectrons in each PMT. Also shown is the best fit to the data. Fit parameters are $A = 0.95 \pm 0.13$, $k = 0.00148 \pm 0.00049$, and $B = 0.01 \pm 0.07$.

$A = -0.146 \pm 0.206$. Given the fit amplitude of $A = 1.25 \pm 0.26$ in the 200 mK runs, this yields a difference between "^{3}He runs" and "200 mK runs" of 5.4 σ. This is strong evidence that the decay seen at thresholds of 2 photoelectrons and higher is indeed due to trapped neutrons, as it is difficult to arrive at any other model in which a difference in signal between positive and negative runs might be eliminated by a small ($\sim 10^{-7}$) change in fractional ^{3}He content.

Finally, Figure 6.16 shows ^{3}He data in which the threshold is 1 photoelectron in each photomultiplier. A large decay signal is seen, indicating that the large 1 photoelectron signal seen in the cold data is not related to trapped neutrons. This is evidence that the presence of the magnetic field while the beam is on can significantly affect the single-photoelectron accidental count rate.

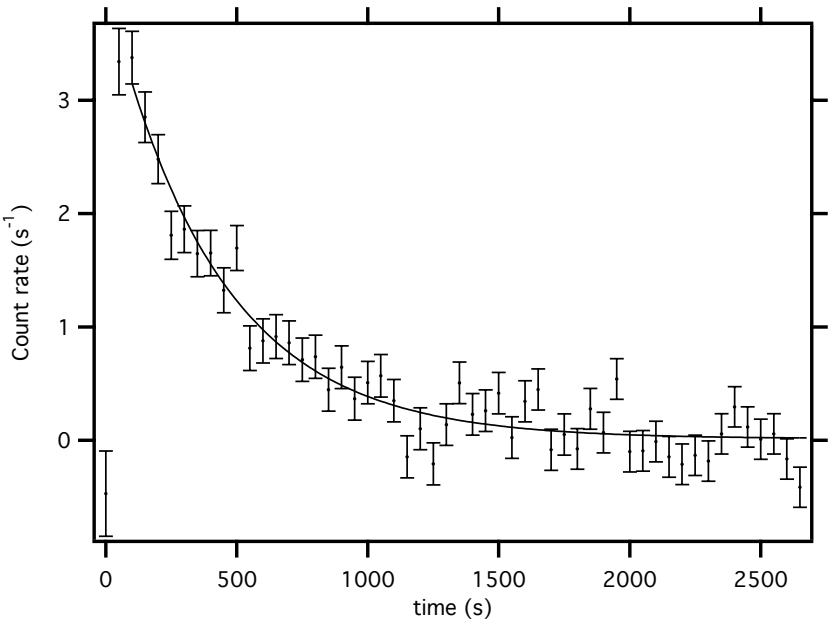

Figure 6.10: The difference between average positive and negative runs with a single photoelectron threshold in the 200 mK data, with a threshold of 1 photoelectron in each PMT. Also shown is the best fit to the data. Fit parameters are $A = 3.97 \pm 0.22$, $k = 0.002360.00020$, and $B = 0.01 \pm 0.05$.

6.6 Discussion

The data above provides evidence that we are trapping ultracold neutrons, based on the following observations:

- The magnitude of the decay signal is comparable to theoretical predictions.
- The warm data does not show this decay, in accordance with UCN upscattering theory.
- The ^{3}He data does not show a decay curve.

Luminescence backgrounds cannot explain the decay signal, since luminescence backgrounds should disappear at high thresholds, while the signal does not. Also, the ^{3}He data does not show a decay signal of significance, and there is no simple

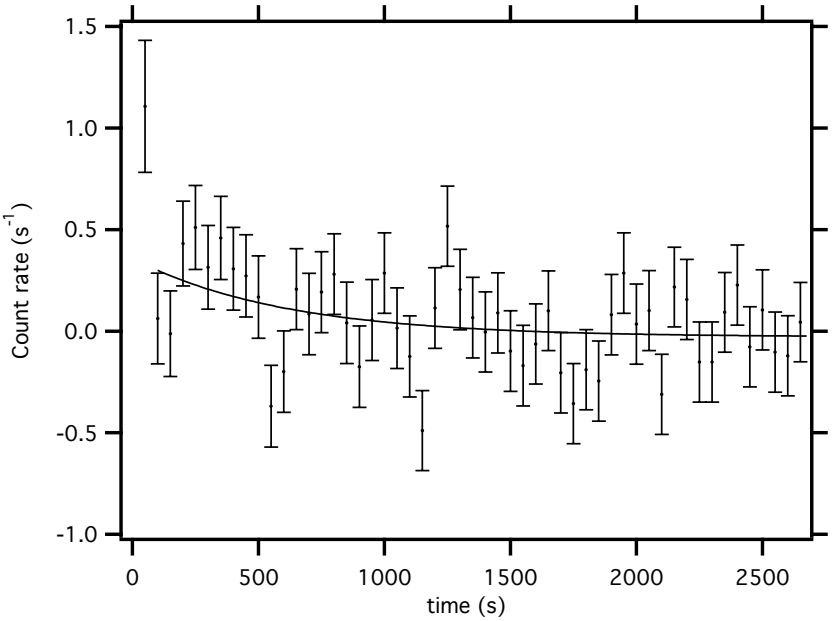

Figure 6.11: The difference between average positive and negative runs in the 750 mK data, with a threshold of 2 photoelectrons in each PMT. Also shown is the best fit to the data. Fit parameters are $A = 0.39 \pm 0.16$, $k = 0.00165 \pm 0.00140$, and $B = -0.03 \pm 0.07$.

model for why the luminescence signal should depend in any way on the presence of a small concentration of ^{3}He.

Activation backgrounds can not explain the signal because the signal disappears in the warm data, and because the signal is not present in the ^{3}He data. There is no simple model for why an activation signal would depend on temperature changes as low as 1 K, and no reason to think they would depend on ^{3}He concentration.

The hypothesis that the decay signal is due to trapped neutrons is good at the 5.4 σ level.

The anamolously short lifetime measured in the cold data is puzzling, and remains to be explained. Possible explanations are:

- Though the subtraction of negative runs from the positive should eliminate

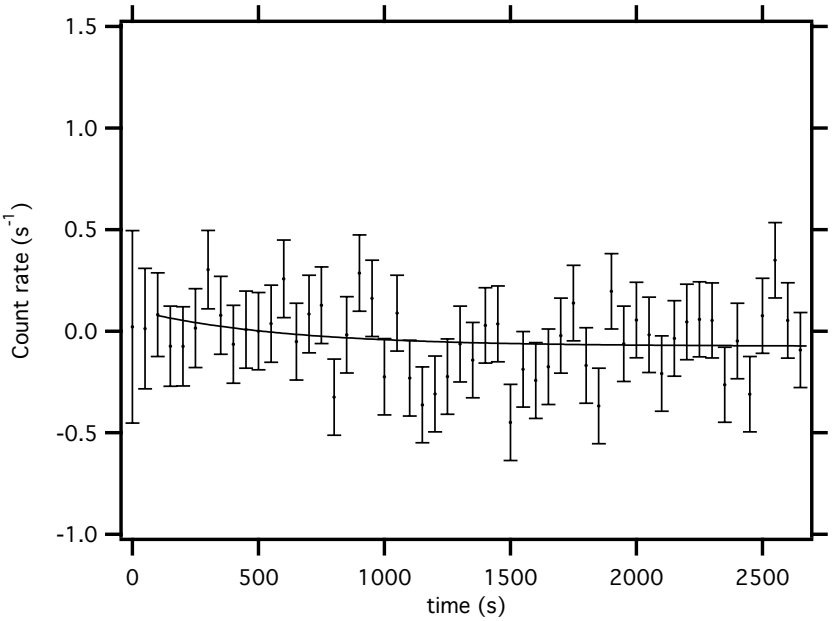

Figure 6.12: The difference between average positive and negative runs in the 1.1 K data, with a threshold of 2 photoelectrons in each PMT. Also shown is the best fit to the data. Fit parameters are $A = 0.18 \pm 0.13$, $k = 0.00173 \pm 0.00264$, and $B = -0.07 \pm 0.05$.

the time-dependent activation background to first order, one worries that the magnetic field experienced by the neutron beam is different in positive and negative runs. If this somehow affected the activation rate (by focusing and defocusing the spin-up and spin-down components of the neutron beam), a time dependent difference between positive and negative runs could be created. This could not be a large effect since no decay signal was observed in the ^{3}He data when analyzed with a 2 photoelectron threshold; however it is posible that a small time-dependent background, not observable in the ^{3}He data because of limited statistics, could have affected the measured lifetime. In the future, the activation background must be either well understood or eliminated in order to perform an accurate neutron lifetime measurement. A new way to control time-dependent backgrounds is presented in Chapter 5.

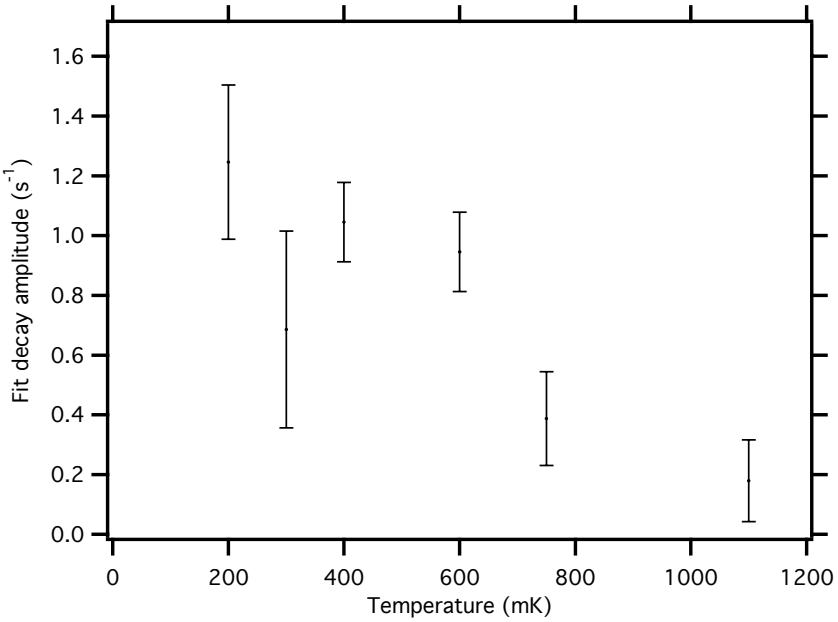

Figure 6.13: Fit decay intensity A for a variety of temperatures. Data analyzed with a 2 photoelectron threshold.

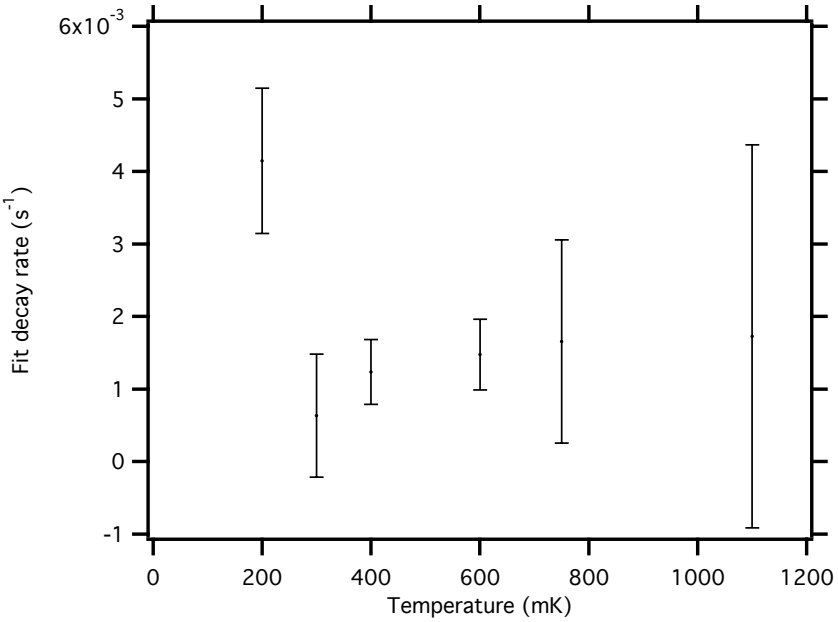

Figure 6.14: Fit decay rate k for a variety of temperatures. Data analyzed with a 2 photoelectron threshold.

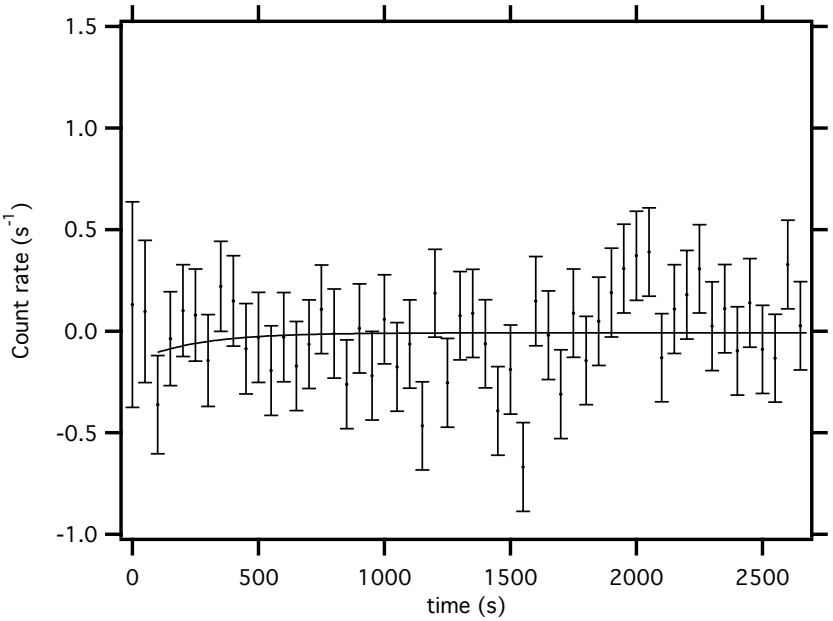

Figure 6.15: The difference between average positive and negative runs, with ^{3}He added, at a temperature of 200 mK. Also shown is the best fit to the data. Fit parameters are $A = -0.146 \pm .206$, and $B = -0.008 \pm 0.033$. The decay rate k is fixed at the rate fit in the "200 mK" data: 0.0041 s^{-1}.

- Marginally trapped neutrons (those with energies greater than the trap depth but confined in semi-stable orbits) would be lost from the trap through wall collisions. Though it seems unlikely that these neutrons could be kept in the trap for a long enough time to contribute the decay curve, this explanation cannot be ruled out entirely. Future experiments could check for this systematic by lowering the trap depth temporarily near the start of a run.

- There may be some unknown mechanism for the helium liquid to impart energy to a trapped neutron. This seems extremely unlikely, as it is energetically impossible for a ^{4}He nucleus to absorb a neutron and the upscattering rate from phonon interactions should be negligible at these temperatures.

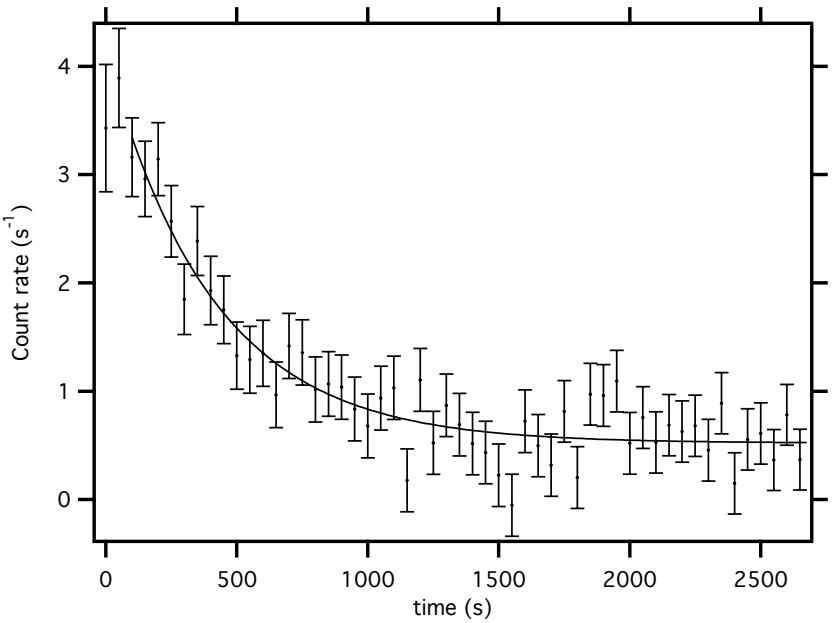

Figure 6.16: The difference between average positive and negative runs with a single photoelectron threshold, with ^{3}He added, at a temperature of 200 mK. Also shown is the best fit to the data. Fit parameters are $A = 3.61 \pm 0.28$, $k = 0.00244 \pm 0.00029$, and $B = 0.52 \pm 0.06$.

A summary of how the fit parameters varied with temperature can be seen in Figure 6.13 and Figure 6.14. As described above, the intensity A of the decay curve decreases markedly at temperatures of 750 mK and above, in accordance with neutron upscattering theory[1]. However, it can also be seen that the measured decay rate k is particularly high in the 200 mK runs, and this can not be explained in this fashion, since upscattering theory predicts that the upscattering rate should only decrease at lower temperatures. Perhaps this is simply a statistical fluctuation and does not indicate an actual physical effect; however since we do not understand why the lifetime is short we cannot rule out the possibility that the temperature of the cell may affect the lfetime by some unknown mechanism.

In 1999, with a weaker, smaller trap and a less efficient neutron decay detector, we measured the neutron lifetime in our trap to be 660^{+290}_{-170}s[23]. Since that time, our

statistics have improved markedly, and we can now claim a lifetime of $482\ ^{+85}_{-63}$ s. This is consistent with our 1999 result, but more clearly demonstrates that the lifetime we measure in our experiment is signicantly shy of the neutron beta-decay lifetime in vacuum. Determination of the source of systematic error leading to this discrepancy is necessary for the future of this technique, and a new apparatus that could be used to track down the problem is described in the next chapter.

Chapter 7

Conclusions and Recommendations

This thesis has described our method of detecting ultracold neutrons, the detection cell and its evolution over the history of the experiment, the ultracold neutron trapping apparatus as of Fall 2001, and the analysis of data taken with this apparatus in August, 2001. The changes to the apparatus undertaken between 1999 and 2001 have resulted in some significant improvements, while data taken with the new apparatus have proved informative.

7.1 Progress in Cycle 8

We have again demonstrated the magnetic trapping of ultracold neutrons. Because our new trap is deeper and larger than the one we used in 1999, and because we could detect neutron decays with higher efficiency, we are able to assign a higher significance (5.4 σ) to the hypothesis that we are trapping ultracold neutrons. In addition, we can point to several recent innovations that should prove invaluable in future incarnations of this experiment:

- Our new magnetic trap has been reliable, providing a trap depth of 1.1 T and

a volume far exceeding that of our previous magnetic trap. Its demountable design allows coils to be changed if they are damaged, and a protection system has been built to guard against damaging the magnet in the case of a quench.

- Our detector is more effective, with an efficiency twice that of the 1999 apparatus. This is due to a new beam dump technology - capturing the neutron beam with a transparent, polished window of pure boron oxide.

- Our new superfluid helium heat link has allowed lower cell temperatures. Its thermal conductance is much higher than our previous copper heat link, and also does not suffer from eddy current heating. We have had no difficulty in filling and cooling down the cell through the heat link, and its conductivity agrees well with theory.

- The development of a 9 Å monochromator has improved the prospects for UCN physics at the NCNR. With a separate beamline at NG6, emitting only 9 Å neutrons, experiments that need this particular wavelength will enjoy lower backgrounds. Because the monochromator does not interfere with the rest of the NG6 beamline, the UCN trapping experiment should have greater access to the beam than in previous years.

7.2 Lessons From Cycle 8

We can also point out several things we have learned from the new upgrade.

- It may be difficult to make a low-current Ioffe trap that is significantly deeper than the present one. While our new trap displayed excessive training behavior, the highest current at which we can run is determined by the ability of our

quench protection circuit to absorb energy from the trap. It appears that this is limited by the high inductance of our coils. Perhaps we could deepen the trap by winding new coils with larger diameter wire. This would decrease the inductance of the magnet (since there would be fewer turns in each coil) but would entail a higher helium boiloff, since higher currents will require larger current leads.

- Time-dependent backgrounds seem unavoidable with the present apparatus design. After going to great lengths to minimize the luminescence and activation backgrounds, we still found that we had significant amounts of both. We are sensitive to activation because our helium bath is a very effective ionizing radiation detector, with little discrimination between our trapped neutron signal and backgrounds caused by stray gamma rays, alphas, and betas. Activation backgrounds can exhibit a multitude of time scales; short-lived decays can obscure the neutron signal at short times, while long-lived decays change the ambient background level in our runs. With a background that changes from run to run, we must fit to the background even when subtracting negative runs. This extra fit parameter greatly increases the uncertainty in the putative neutron signal. Luminescence backgrounds are particularly troubling because they can vary in intensity depending on the history of the magnetic field. Thus, one can not be sure that time-dependent backgrounds due to luminescence are eliminated by subtracting field-off runs. Clearly all time-dependent backgrounds must be either eliminated or fully understood in order for a neutron lifetime measurement to be completed.

7.3 Recommendations For Future Work

Separate Production and Detection Regions

Figure 7.1 shows a new concept for the construction of the UCN trapping experiment. Key to this design is the division of the experiment into two parts: a UCN production apparatus and a UCN trapping apparatus, connected by a UCN Guide.

The production apparatus would consist of a can filled with superfluid helium, connected thermally to a dilution refrigerator and surrounded by cryogenic layers at 4 K, 77 K, and 300 K. One end of the can would have a neutron-passing window, while the rest would be covered by neutron moderating and absorbing materials. The inside walls of the can would be coated with a material that stores UCN well and has low wall depolarization, such as beryllium or diamond-like graphite. UCN created within the superfluid helium by the neutron beam would rattle around in the material box. The only exit for these UCN would be through a small tube leading out of the production region (at 90 degrees with respect to the neutron beam), also filled with superfluid helium. Low-field-seeking neutrons would be prevented from entering the tube by a solenoid surrounding the tube, a "Magnetic UCN Valve". High-field-seekers would be sucked into the field and into a narrow UCN guide.

The walls of the UCN guide need not yield an especially long storage lifetime, but they do need to have a high UCN potential and should be as specular as possible (again, beryllium or graphite are appropriate). The UCN guide passes out of the production apparatus, through a wall of neutron and gamma ray shielding, and into the UCN trapping apparatus. There the volume increases and the neutrons expand into the trapping region, also filled with superfluid helium. High field seeking neutrons would immediately hit the wavelength shifting coating on the walls, upscatter, and

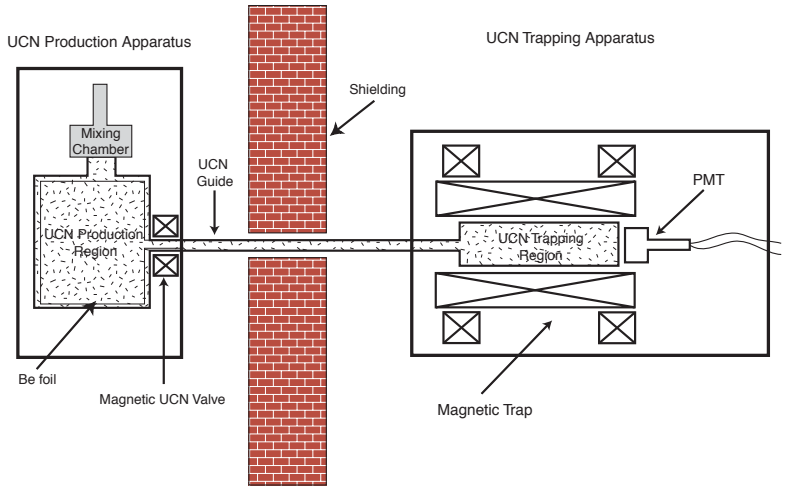

Figure 7.1: A possible future design

be lost.

The procedure for trapping UCN would be as follows: With the magnetic UCN valve closed (field on) the neutron beam would be turned on and the production volume filled with UCN. When a suitably high density is reached, the magnetic valve is opened and the closer pinch coil of the magnetic trap is lowered. Low-field-seeking neutrons will then pass through the UCN guide and flood the trapping region. Low energy UCN will not hit the TPB coating because the trapping field prevents them from reaching it. After a few seconds, the closer pinch coil and magnetic UCN valve are again closed. A photomultiplier or other light detector, viewing the trap from above, counts the UCN decays within the trap. After watching the UCN decay, the cycle is repeated. Note that the neutron beam is on continuously; while neutrons are being counted in the trap, the production region is being filled with new UCN.

To calculate the wall lifetime of neutrons in the production region, consider a cylinder 15 cm in diameter, 20 cm long, with a volume V_p of 3500 cm^3 and a surface area S_p of 940 cm^2. Then, assuming a UCN velocity v of 400 cm s^{-1} and a loss per

bounce p_p of 8×10^{-6}, one calculates

$$\tau = \frac{1}{k_p} = \frac{4V_p}{vS_p p_p} = 4650\,\mathrm{s}.$$

The value of p_p used here is typical of a cold, cleaned beryllium surface, assumes a $2f$ value of 2×10^{-5}, and takes into account $v/v_{crit} = 0.38$ (see Section 1.3). This wall lifetime is quite a bit longer than the neutron beta-decay lifetime, so the maximum UCN density would not be limited by wall losses. Alternately, wall losses could be significantly worse than assumed here, with little impact on the maximum UCN density.

After opening the magnetic valve, the loss rate per neutron is

$$k = \frac{v}{4V_{total}}(S_p p_p + S_g p_g),$$

where V_{total} is the total volume of production, trap, and guide, S_g is the surface area of the guide, and p_g is the probability of loss per bounce in the guide. Assuming a V_{trap} of 3400 cm^3, V_g of 1000 cm^3, and p_g of 2×10^{-4}, one finds that $\tau = 260$ s. This means that one would have approximately 260 s to open the magnetic valve, open the pinch coil, fill the trap with neutrons, and raise the pinch coil. The trap volume V_{trap} of 3400 cm^3 corresponds a tube 30 cm long and 12 cm in diameter. The guide is assumed to be 200 cm long and 2.5 cm in diameter. High specularity of the neutron guide is desired in this design, as the UCN densities must equalize in the production and trapping regions before too many UCN are lost. However, a long lifetime in the UCN guide is likely at low temperatures, and high specularity is possible if the UCN reflector is coated on an optically flat surface.

One might find it necessary to remove from the experiment the UCN that are not trapped so as not to introduce any extra backgrounds. This might be done by allowing the untrapped neutrons to hit an absorbing material after the lower pinch coil has

been ramped up. While loading the trap, this absorbing material would be kept in a high magnetic field so as not to lose the low-field seeking neutrons. The absorbing material might double as a UCN detector; for example, a Li:Ti detector could count each UCN absorbed on its surface. In this way the UCN production from run to run could be monitored separately from the decay of trapped UCN. A drop in the rate in the Li:Ti detector would indicate a decrease in the UCN production rate (say, from a mis-aligned neutron beam or a deteriorating UCN reflection probability in the production region or UCN guide). A drop in the rate of trapped neutrons detected relative to the rate in the Li:Ti detector would indicate deteriorating scintillation detection in the trapping region.

Outside the superfluid helium, the guts of the experiment would be surrounded by multiple cryogenic layers, at 4 K, 77 K, and 300 K. The Production Apparatus and Trapping Apparatus would each have their own separate liquid helium and liquid nitrogen baths, while the UCN guide would have neither, being connected thermally to the larger halves of the experiment by layers of copper and aluminum at 4K at 77K. The UCN guide and surrounding layers would be only of small diameter: large enough to pass UCN effectively, yet small enough to pierce lead and polyethylene layers leaving only a small unshielded area for neutrons and gamma rays to enter the trapping apparatus. The UCN guide would need a small magnetic field along its entire length to maintain neutron polarization as they travel; this could be provided by a weak solenoidal field supplied from room temperature.

An apparatus designed as described would have several advantages over the current design, including improved modularity, lower constant background, lower time-dependent background, higher trapped UCN density, and improved reliability. I will discuss each of these in turn.

- **Improved Modularity.** Because the apparatus can be divided into two parts, each of which can be cooled down separately, experimental work can be done with each part more easily than if one large, more complicated experiment had to be cooled down. For example, the UCN production apparatus could be cooled down to test UCN production rate, UCN material bottle lifetimes, and the temperature dependence of UCN loss rate in helium. These experiments could be done by attaching a material at the end of the UCN guide that absorbs neutrons directly and creates an electronic signal. After building up low field seekers in the trap, the magnetic valve could be opened, letting the neutrons be absorbed in the detector. The signal to noise in the detector would be very high, allowing highly accurate measurements of the UCN production and loss rates. The UCN trapping apparatus could be tested independently (perhaps at a remote location if this is convenient) to test the magnetic trap and calibrate the neutron detector. It will also be easier to get the apparatus leak tight, as each half of the experiment could be cooled down separately to check for leaks. Even after the two halves are connected, leaks will be easier to locate because the two halves of the experiment are well physically separated, each with its own liquid helium and liquid nitrogen baths. The UCN production apparatus might later be used as a general UCN source for other experiments, for example to test experimental concepts for the neutron EDM measurement.

- **Lower Constant Background.** The UCN trapping apparatus could be more easily shielded from gamma rays and neutrons than our current apparatus. This is because there only needs to be a small (15 cm diameter) hole in the shielding to allow the UCN guide to connect the two halves of the experiment. Because the UCN trapping apparatus does not need to be close to the beam aperture, there

will be more room for thicker and more complete neutron and gamma shielding. The muon rate in a vertical trap is lower than in a horizontal trap because the cosmic ray flux is peaked in the downward direction. Also, cosmic rays that do pass through the detector will be more easily detected, as a smaller muon paddle area coverage will be necessary. One new source of constant background would be VCN from the production region that travel through the guide and decay in the trapping region. The magnitude of this background is uncertain and must be tested experimentally; however it is unlikely to be large compared to the background from gamma rays.

- **Lower Time Dependent Backgrounds.** In the current apparatus, significant time dependent backgrounds are apparent after the neutron beam is turned off. The subsequent luminescence and radioactive decay from neutron activation can obscure the decay signal from trapped neutrons and introduce systematic error in the measurement of the neutron lifetime. With wide separation between the UCN production and trapping regions, both of these sources of time dependent background can be eliminated. Luminescence light from the production region can be blocked by baffles and is very unlikely to reach the detector. Gamma rays from neutron activation are also unlikely to reach the detector, as the trapping apparatus can be well shielded and is far away from the production apparatus. Especially tantalizing is the possibility that the neutron beam could be kept on continuously in this configuration, resulting in total elimination of time-dependent luminescence and activation backgrounds. This could be done provided that the constant background coming from the neutron beam is low enough. This is a plausible scenario considering that our current apparatus runs with other experiments nearby. There would be a small background from

high-field-seeking UCN that decay in the trapping region, but this should be small compared to both the signal and the constant background, since most high field seekers will be upscattered from the walls of the Transport Region or the trapping region. The capture of upscattered UCN in the surrounding neutron shielding is unlikely to produce a signal in the superfluid helium.

- **Higher UCN Density.** With a dedicated UCN production apparatus, this half of the experiment can be designed to better maximize UCN creation, without the constraints imposed by the bulky magnetic trap. For example, the production region can be closer to the beam aperture, with fewer, wider collimaters. This could double the UCN production. Also, the production region could be surrounded by a hydrogenous material to reflect neutrons back into the production region. This method of increasing UCN production has been studied by Bangert *et al.*[88]; they find that UCN production can be increased by a factor of 2 by surrounding the production region with 2 cm of acrylic. Finally, if the neutron beam is on continuously, the experiment will not have to pause data collection for a lengthy period of time to accumulate UCN. While trapped neutrons are decaying and being counted in the Trapping Apparatus, the production apparatus will be accumulating low field seeking UCN for the next trapping run. This will yield a higher number of runs per day, with better statistics as a result. Though the density of neutrons will decrease after the magnetic valve is opened by the ratio $V_p/(V_t + V_g + V_p)$, where V_p, V_t, and V_g are the volumes of the production region, trapping region, and UCN guide respectively, this ratio should be close to 1 if the production volume is sufficiently large. Also, some low-field-seekers will be lost to upscattering at surfaces, though ultra-high vacuum conditions and clean surfaces in the production region should keep these

losses to a minimum.

- **Improved Reliability.** Separation of the experiment into two halves should eliminate all large indium seals, which are the primary source of cryogenic leaks in the current apparatus. This should improve the chance of successful cooldowns.

The KEK Magnet

It was discovered during the design of our present apparatus that many superconducting quadrupole magnets exist that, while running at very high currents, might be used to make a very large, very deep magnetic trap. Quadrupole magnets are used at particle accelerators to focus counter-propagating beams of charged high energy particles near a detector, thus increasing the collision rate. By simply adding a pair of solenoids to the accelerator quadrupole, one could have an extremely large and deep magnetic trap.

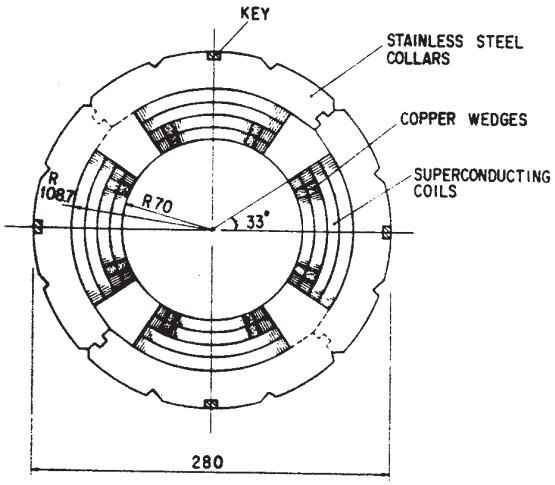

Figure 7.2: A cross-section view of the KEK magnet

The most promising magnet design was identified to be the quadrupole magnet used at the TRISTAN accelerator at KEK in Japan[89]. These magnets are quite large, sporting a bore diameter of 14 cm, a usable field region 100 cm long, and a field at the bore wall of 10.0 T when running at 5000 A in superfluid helium[90]. The load line characteristics of the magnetic are shown in Figure 7.3. These quadrupole magnets have not been in use since the shutdown of TRISTAN in 1995, and have been in storage since that time. Excited about the possibility of using one of these magnets in the neutron trapping experiment, we contacted the group that built and tested these magnets. The KEK graciously agreed to send us one of their magnets for testing. We have not yet tested it in conjunction with a solenoidal field, although we have tested our quench protection circuitry in conjuction with the magnet at currents as high as 1800 A. There is little doubt whether the magnet would perform well by itself; the major experimental question is whether the magnet could function properly under the additional mechanical stresses caused by a superimposed solenoidal field. The solenoid field would also lower the maximum current. We estimate that a trap depth of 4.4 T at 4400 A is possible in superfluid helium, given a trap diameter of 10 cm. If the magnet were run at 4.5 K, the maximum trap depth would be about 3.8 T, running at 3800 A.

Incorporating the KEK magnet into our experiment would be a major undertaking. The magnet is quite heavy (400 kg) and large (28 cm diameter, 145 cm length). With solenoids added, the total diameter of the magnet assembly would be about 35 cm. In addition, it would run on large currents and would thus need quite thick current leads, generating large heat loads on the helium bath. An estimate for the heat load from suitable High-Tc leads was provided to us by a manufacturer of such

leads.[1]. These would be pinned at 77 K at the top end and enter the liquid helium bath at 4.5 K. For leads 30 cm long capable of carrying 2500 A, Eurus estimates a heat load per lead of 0.9 W. Assuming that the heat load scales linearly with the lead current capacity, and using the conversion 1 W = 33 ℓ/day of liquid helium, one arrives at the conclusion that If we bought High-Tc leads capable of carrying 4400 A, the total helium boiloff per day from the leads would be 105 liters per day. This heat load might be reduced by a factor of two by cooling the leads with the boiloff helium.

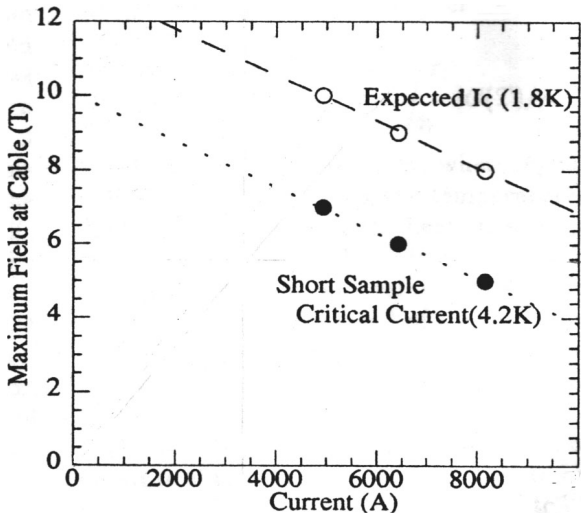

Figure 7.3: Load lines for the KEK magnet at 4.2 K and 1.8 K.

However, the number of neutrons that we could trap using the KEK magnet is far greater than using our current apparatus. We now can trap about 2,000 neutrons per load. With one cycle of running and no time-dependent backgrounds, simulations show that we could achieve a lifetime uncertainty of 4.5 s. Using the KEK magnet (with a trap depth of 4.4 T), we could load as many as 170,000 neutrons per run. In 1 cycle of run time at NG6, the statistical uncertainty in the neutron lifetime would

[1]Eurus Technologies Inc., Tallahassee, FL, http://www.teameurus.com

be 0.2 seconds. A larger and deeper trap is necessary for this experiment to reach its ultimate precision.

While it is unlikely that we would use the KEK magnet in the near future, it is important that we keep the KEK magnet in mind when we redesign our apparatus. If we switch to a two-dewar scheme as recommended in this thesis, then the dewar containing the magnetic trap should be large enough to hold the KEK magnet and solenoids.

Summary of Recommendations

In summary, we recommend that the design of the neutron trapping apparatus be changed to allow separate detection and trapping regions. This will require development of expertise in our group in the storing of neutrons using material bottles. It will also require a major effort in the construction of new dewars and associated cryogenics. We also recommend the winding of new, higher current coils for the magnetic trap that we presently use, but constructing the new dewar in such a way that it could accomodate the much larger KEK magnet.

Appendix A

Data Analysis Software

The software described in this Appendix was used to perform an independent analysis of the data acquired during August, 2001. It is in many ways similar to the software developed previously by Carlo Mattoni[25], and serves the same functions. However, it was written in a short time period after all of the data was collected and was developed independently. It takes as input the digitized photomultiplier pulses and time stamps associated with each data run, and outputs a decay curve, given such parameters as photomultiplier thresholds and specific runs to be analyzed.

There are four separate routines, called the "parser", the "viewer", the "cutter", and the "histogrammer". They form a software package called "Danalyzer". The individual routines are described below:

- **The Parser**

  The parser takes as input the .daq files that are saved following each data run. These files contain digitized photomultiplier pulses and time stamps, saved in a byte block format. Each pulse is read into the program and integrated to yield a pulse area, which is representative of the total charge collected by the photomultiplier anode. Each event is then characterized by two pulse areas (one

for each PMT) and a event time. This information is saved as a .par file.

- **The Viewer**

  The viewer allows the user to see individual photomultiplier traces, compare the traces of master and slave cards, and study how the parsing algorithm operates. The viewer takes as input a .daq file, creates a .vie file, and uses this file in its running procedure.

- **The Cutter**

  The cutter takes as input the .par file outputted by the parser. It allows the user to eliminate events that do match a combination of designated criteria. Usually these criteria are pulse size thresholds. The cutter outputs a .cut file.

- **The Histogrammer**

  The histogrammer takes as input the .cut files from a number of user-designated files, and creates a summed histogram of their decay curves. "Negative" fiels are subtracted from "positive" files (see Chapter 6) to make a decay curve suitble for fitting.

Bibliography

[1] R. Golub, D. Richardson, and S. K. Lamoreaux. *Ultra-Cold Neutrons*. Adam Hilger, 1991.

[2] R. E. Lopez and M. E. Turner. Precision prediction for the big-bang abundance of primordial helium 4. *Physical Review D*, 59:103502, 1999.

[3] Y. Hayato et al. Search for proton decay through p $->$ antineutrino K+ in a large water cerenkov detector. *Physical Review Letters*, 83:1529, 1999.

[4] D. Dubbers. Particle physics with cold neutrons. *Progress in Particle and Nuclear Physics*, 26:173–252, 1991.

[5] D.E. Green et al. Particle listings. *The European Physics Journal C*, 15:1, 2000.

[6] J. Reich et al. A measurement of the beta asymmetry in neutron decay with PERKEO II. *Nuclear Instruments and Methods in Physics research A*, 440:535–538, 2000.

[7] P. Liaud et al. The measurement of the beta asymmetry in the decay of polarized neutrons. *Nuclear Physics A*, 407:53, 1997.

[8] B. G. Erozolimsky et al. Corrigendum: Corrected value of the beta-emission asymmmetry in the decay of polarized neutrons measured in 1990. *Physics Letters B*, 412:240, 1997.

[9] P. Bopp et al. Beta-decay asymmetry of the neutron and g_a/g_v. *Physics Review Letters*, 56:919, 1986.

[10] D. Wilkinson. Analysis of neutron beta-decay. *Nuclear Physics A*, 377:472, 1982.

[11] J. P. Alexander et al. First measurement of the $b \to \pi\ell\nu$ and $b \to \rho(\omega)\ell\nu$ branching fractions. *Physics Review Letters*, 77:5000–5004, 1996.

[12] H. Leutwyler and M. Roos. Determination of the elements v_{ud} and v_{us} of the kobayashi-maskawa matrix. *Zeitschrift fur Physik C*, 25:91, 1984.

[13] S. Arzumanov et al. Neutron lifetime measured by monitored storing of ultracold neutrons. *Nuclear Instruments and Methods A*, 440:511–516, 2000.

[14] J. Byrne, P. G. Dawber, C. G. Habeck, S. J. Smidt, J. A. Spain, and A. P. Williams. A revised value for the neutron lifetime measured using a penning trap. *Europhysics Letters*, 33:187–192, 1996.

[15] W. Mampe, L. N. Bondarenko, V. I. Morozov, Yu. N. Panin, and A. I. Fomin. Measuring neutron lifetime by storing ultracold neutrons and detecting inelastically scattered neutrons. *JETP Letters*, 57:82–87, 1993.

[16] V. V. Nesvizhevskiĭ, A. P. Serebrov, R. R. Tal'daev, A. G. Kharitonov, V. P. Alfimenkov, A. V. Streikov, and V. N. Shvetsov. Measurement of the neutron lifetime in a gravitational trap and analysis of experimental errors. *Soviet Physics JETP*, 75:405–412, 1992.

[17] W. Mampe et al. Neutron lifetime measured with stored ultracold neutrons. *Physical Review Letters*, 63:593, 1993.

[18] P. E. Spivak. Neutron lifetime obtained from atomic-energy-institute experiment JETP Lett.28, 303(1978). *Soviet Physics JETP*, 67:1735–1740, 1988.

[19] W. Paul, F. Anton, L. Paul, S. Paul, and W. Mampe. Measurement of the neutron lifetime in a magnetic storage ring. *Zeitschrift für Physik C, Particles and Fields*, 45:25–30, 1989.

[20] J. Byrne, P. G. Dawber, J. A. Spain, A. P. Williams, M. S. Dewey, D. M. Gilliam, G. L. Greene, G. P. Lamaze, R. D. Scott, J. Pauwels, R. Eykens, and A. Lamberty. Measurement of the neutron lifetime by counting trapped protons. *Physical Review Letters*, 65:289–292, 1990.

[21] M.G.D. van der Grinten et al. Characterization and development of diamond-like carbon coatings for storing ultracold neutrons. *Nuclear Instruments and Methods in Physics Research A*, 423:421–427, 1999.

[22] J. M. Doyle and S. K. Lamoreaux. On measuring the neutron beta-decay lifetime using ultracold neutrons produced and stored in a superfluid-^{4}he-filled magnetic trap. *Europhysics Letters*, 26:253–258, 1994.

[23] C. R. Brome. *Magnetic Trapping of Ultracold Neutrons*. PhD thesis, Harvard University, 2000.

[24] A. Steyerl and S.S. Malik. Sources of ultracold neutrons. *Nuclear Instruments and Methods in Physics Research A*, 284:200–207, 1989.

[25] C. E. H. Mattoni. *Magnetic Trapping of Ultracold Neutrons Produced Using a Monochromatic Cold Neutron Beam*. PhD thesis, Harvard University, 2002.

[26] P.C. Hendry and P.V.E. McClintock. Continuous flow apparatus for preparing isotopically pure ^{4}He. *Cryogenics*, 27:131–138, 1987.

[27] H. Fleishman et al. *Review of Scientific Instruments*, 30:1130, 1959.

[28] E. H. Thorndike and W. J. Shlaer. *Review of Scientific Instruments*, 30:838, 1959.

[29] J.R. Kane and R. T. Siegel. *Bulletin of the American Physical Society*, 10:515, 1965.

[30] J. E. Simmons and R. B. Perkins. Liquid helium scintillation counter as a neutron polarimeter. *Review of Scientific Instruments*, 32:1173, 1961.

[31] F. E. Moss and F. L. Hereford. Inhibition of the scintillation of He II. *Physical Review Letters*, 11:63–64, 1963.

[32] F. L. Hereford and F. E. Moss. Recombination luminescence in the scintillation of normal and superfluid liquid helium. *Physical Review*, 141:204–208, 1966.

[33] J. Jortner et al. Energy transfer phenomena in liquid helium. *Physical Review Letters*, 12:415–416, 1964.

[34] C. M. Surko and F. Reif. Investigation of a new kind of energetic neutral excitation in superfluid helium. *Physical Review*, 175:229–241, 1968.

[35] G. W. Rayfield. Modulation of the neutral excitation current in liquid helium by electric fields. *Physical Review Letters*, 23:687, 1969.

[36] R. P. Mitchell and G. W. Rayfield. Neutral excitations from a tritium source immersed in he II. *Physics Letters A*, 37:231–232, 1972.

[37] W. S. Dennis et al. Spectroscopic identification of excited atomic and molecular states in electron-bombarded liquid helium. *Physical Review Letters*, 23:1083–1086, 1969.

[38] A. V. Konovalov and G. V. Shlyapnikov. Decay kinetics of triplet He(2^3S) excitations in liquid and solid helium. *Soviet Physics JETP*, 73:286–291, 1991.

[39] J. W. Keto et al. Dynamics of atomic and molecular metastable states produced in electron-bombarded superfluid helium. *Physical Review Letters*, 28:792–795, 1972.

[40] J. W. Keto et al. Dynamic properties of neutral excitations produced in electron-bombarded superfluid helium. I. The He(2^3S) and $He_2(a^3\Sigma)$ atomic and molecular metastable states. *Physical Review A*, 10:872–886, 1974.

[41] J. W. Keto et al. Dynamic properties of neutral excitations produced in electron-bombarded superfluid helium. II. Afterglow fluorescence of excited helium molecules. *Physical Review A*, 10:887–896, 1974.

[42] J. R. Woodworth and H. W. Moos. Experimental determination of the single-photon transition rate between the 2^3S_1 and 1^1S_0 states of He I. *Physical Review A*, 12:2455, 1975.

[43] A. Koymen et al. Multiple activation energies for conversion of He(2^3S) atoms to $He_2(a^3\Sigma_u^+$ molecules in ternary collisions. *Chemical Physics Letters*, 168:405–409, 1990.

[44] M. Stockton et al. Ultraviolet emission spectrum of electron-bombarded superfluid helium. *Physical Review A*, 5:372–379, 1972.

[45] C. M. Surko et al. Spectroscopic study of the luminescence of liquid helium in the vacuum ultraviolet. *Physical Review Letters*, 24:657–659, 1970.

[46] M. Stockton et al. Ultraviolet emission spectrum of electron-bombarded superfluid helium. *Physical Review Letters*, 24:654, 1970.

[47] J. S. Adams et al. Scintillation and quantum evaporation generated by single monoenergetic electrons stopped in superfluid helium. *Journal of Low Temperature Physics*, 113:1121, 1998.

[48] G. W. Seidel, 2000. Personal communication.

[49] D. B. Kopeliovich et al. Spectral properties and the dynamics of excimer he_2^* molecules in he^4 crystals. *Soviet Physics JETP*, 69:638, 1989.

[50] V. B. Eltsov et al. *Soviet Physics JETP*, 81:909, 1995.

[51] R. Mehrotra et al. A study of the neutral excitation current in liquid Helium 4 above 1 K. *Journal of Low Temperature Physics*, 36:47–64, 1978.

[52] R. Golub and S. K. Lamoreaux. Neutron electric dipole moment, ultracold neutrons and polarized ^{3}He. *Physics Reports*, 237:1, 1994.

[53] H. A. Roberts and F. L. Hereford. Diffusion of metastable systems produced by α-particles in liquid ^{3}He-^{4}He solutions. *Physics Letters A*, 38:395–397, 1972.

[54] S.R. Bandler et al. Projected performance of a large superfluid helium solar neutrino detector. *Journal of Low Temperature Physics*, 93:785, 1993.

[55] D.N. McKinsey and J.M. Doyle. Liquid helium and liquid neon - sensitive, low background scintillation media for the detection of low energy solar neutrinos. *Journal of Low Temperature Physics*, 118:153, 2000.

[56] C. H. Lally et al. UV quantum efficiencies of organic fluors. *Nuclear Instruments and Methods in Physics Research B*, 117:421–427, 1996.

[57] W. M. Burton and B. A. Powell. Fluorescence of tetraphenyl butadiene in the vacuum ultraviolet. *Applied Optics*, 12:87, 1973.

[58] M. Brunet et al. Proprietes de photocathodes metalliques et de couches fluorescentes dans l'ultraviolet lointain. *Journal of Physics A*, 24:87, 1963.

[59] T.T.H. Mai and R. Drouin. Relative quantum efficiencies of some ultraviolet scintillators. *Applied Optics*, 23:2046–2047, 1971.

[60] J. Kumar and A. K. Datta. vacuum ultraviolet scintillators: sodium salicylate and p-terphenyl. *Applied Optics*, 18:1414, 1979.

[61] W. Viehmann and R. L. frost. Thin film waveshifter coatings for fluorescent radiation converters. *Nuclear Instruments and Methods in Physics Research*, 167:405–415, 1979.

[62] M. Grande et al. An optimised thin film wavelength shifting coating for Cherenkov detection. *Nuclear Instruments and Methods in Physics Research*, 215:539–548, 1983.

[63] C. L. Butner and W. Viehmann. Quantum efficiency measurements for several waveshifter coatings in the vacuum ultraviolet. *Applied Optics*, 23:2046, 1984.

[64] E. C. Bruner. *Journal of the Optical Society of America A*, 59:204, 1969.

[65] J. A. R. Samson. *Techinques of Vacuum Ultraviolet Spectroscopy*. Wiley, New York, 1967.

[66] S. R. Sandler et al. Dimethyl styrene yields more efficient scintillators. *Nucleonik*, 18:102, 1960.

[67] O. A. Gunder et al. Scintillation detectors based on poly-2,4-dimethylstyrene: structural peculiarities and radiation damage. *IEEE Transactions on Nuclear Science*, 42:320, 1995.

[68] C. d'Ambrosio et al., 1990. CERN-PRE-90-96.

[69] K. Habicht. *Szintillationen in flussigem Helium - ein Detektor Fur ultrakalte Neutronen*. PhD thesis, Technischen Universitat Berlin, 1998.

[70] A. G. Tenner. *Nuclear Instruments and Methods in Physics Research*, 22:1, 1963.

[71] J.P. Hernandez and M. J. Silver. Dynamics of electron-bubble formation in helium. *Physical Review A*, 2:1949, 1970.

[72] B. E. Callicoatt et al. Charge transfer with He clusters. *Journal of Chemical Physics*, 105:7872–7875, 1996.

[73] B. E. Callicoatt et al. Capture and ionization of argon within liquid helium droplets. *Journal of Chemical Physics*, 108:9371–9382, 1998.

[74] M. Ovchinnikov et al. Charge localization and fragmentation dynamics of ionized helium clusters. *Journal of Chemical Physics*, 108:93511, 1998.

[75] A. V. Benderskii et al. Photodynamics in superfluid helium: Femtosecond laser-induced ionization, charge recombination, and preparation of molecular rydberg states. *Journal of Chemical Physics*, 110:1542, 1999.

[76] S. Sato et al. *Bulletin of the Chemical Society of Japan*, 47:2174, 1974.

[77] H. A. Roberts et al. Scintillation of liquid helium under pressure. II. $2 > T > 0.3$ K. *Physical Review A*, 4:2380–2385, 1971.

[78] T. A. King and R. Voltz. The time dependence of scintillation intensity in aromatic materials. *Proceeding of the Royal Society of London*, pages 424–439, 1966.

[79] H. A. Roberts and F. L. Hereford. Luminescence of helium II produced by weak α-particle sources. *Physical Review A*, 7:284–291, 1973.

[80] Kubota et al. *Physical Review B*, 20:3486, 1979.

[81] A. P. Hickman et al. Nature of excited helium atoms in liquid helium: a theoretical model. *Physical Review B*, 12:3705–3717, 1975.

[82] P. Calvani et al. Neutral excitations in liquid helium. *Il Nuovo Cimento B*, 19:271–286, 1973.

[83] C. O. Chablowski et al. *Journal of Chemical Physics*, 90:2504, 1989.

[84] V. B. Eltsov et al. Triplet-state $^4He_2^*$ in superfluid helium. *Journal of Low Temperature Physics*, 110:219, 1998.

[85] Frank Pobell. *Matter and Methods at Low Temperature*. Springer-Verlag, 1965.

[86] J. S. Butterworth et al. A removable cryogenic window for transmission of light and neutrons. *Review of Scientific Instruments*, 69:3998, 1998.

[87] A. Serebrov et al. Depolarization of UCN stored in material traps. *Nuclear Instruments and Methods A*, 440:717–721, 2000.

[88] P.D. Bangert et al. Enhancement of superthermal ultracold neutron production by trapping cold neutrons. *Nuclear Instruments and Methods in Physics Research A*, 410:264–272, 1998.

[89] K. Tsuchiya et al. Performance of the eight superconducting quadrupole magnets for TRISTAN low-beta insertions. *IEEE Transactions on Magnetics*, 27:1940–1943, 1991.

[90] K. Sasaki et al. Test results of spare TRISTAN insertion quadrupole magnet with yoke added in superfluid helium. *IEEE Transactions on Applied Superconductivity*, 7:570–573, 1997.